

© 2008

GAURAV SARAF

ALL RIGHTS RESERVED

STUDIES OF IN-PLANE ANISOTROPIC PHYSICAL PROPERTIES

IN a-PLANE $\text{Mg}_x\text{Zn}_{1-x}\text{O}$

BY

GAURAV SARAF

A Dissertation submitted to the

Graduate School-New Brunswick

Rutgers, The State University of New Jersey

in partial fulfillment of the requirements

for the degree of

Doctor of Philosophy

Graduate Program in Electrical and Computer Engineering

Written under the direction of

Professor Yicheng Lu

and approved by

New Brunswick, New Jersey

May, 2008

ABSTRACT OF THE DISSERTATION
STUDIES OF IN-PLANE ANISOTROPIC PHYSICAL PROPERTIES IN a-
PLANE $\text{Mg}_x\text{Zn}_{1-x}\text{O}$

by GAURAV SARAF

Dissertation Director: Prof. Yicheng Lu

$\text{Mg}_x\text{Zn}_{1-x}\text{O}$ is a compound semiconductor material formed by alloying ZnO with MgO. The larger direct bandgap of $\text{Mg}_x\text{Zn}_{1-x}\text{O}$ ($\sim 4\text{eV}$ for $\text{Mg}_{0.33}\text{Zn}_{0.67}\text{O}$) renders it useful as a barrier layer in ZnO/ $\text{Mg}_x\text{Zn}_{1-x}\text{O}$ based heterostructures and quantum wells. Conventionally grown c-oriented ZnO based quantum wells suffer from piezoelectric and spontaneous polarization fields, leading to lower quantum efficiency. Non-polar a-plane and m-plane ZnO based heterostructures avoid such problems. The non-polar $\text{Mg}_x\text{Zn}_{1-x}\text{O}$ films also possess in-plane anisotropic optical, acoustic and electrical properties, useful for novel polarization sensitive devices. However, as-grown non-polar $\text{Mg}_x\text{Zn}_{1-x}\text{O}$ films show rougher surface compared to its c-plane counterpart, introducing serious difficulty in growth of high quality heterostructures.

This dissertation addresses growth optimization and comprehensive characterization of a-plane $\text{Mg}_x\text{Zn}_{1-x}\text{O}$ ($0 \leq x \leq 0.33$) films on r-sapphire substrates using Metalorganic Chemical Vapor Deposition (MOCVD). Angle Resolved Auger electron spectroscopy (ARAES) indicates that Mg replaces Zn in ZnO lattice. Mg composition and films' crystal properties are characterized using transmission spectroscopy and x-ray diffraction (HRXRD), respectively. The in-plane strain along c-axis is compressive,

while perpendicular to c-axis is tensile. Strain anisotropy reduces with increase in film thickness due to relaxation, with complete relaxation at film thickness of $\sim 2\mu\text{m}$. An increase in Mg composition increases a-axis lattice parameter and reduces c-axis lattice parameter, resulting in higher strain in the films. Scanning tunneling microscopy (STM) shows long and elongated terraces on films surface due to anisotropic surface diffusion and strain-relaxation. The direction of terraces is dependent on the miscut direction of r-sapphire substrates. The effects of film thickness, Mg composition, and deposition temperature on surface morphology have been analyzed. A red shift in the optical transmission edge is observed for electric field polarized perpendicular to in-plane c-axis as compared to that along in-plane c-axis. An increase in Mg composition reduces the separation in transmission edge. In-plane anisotropy in Hall mobility is analyzed, with mobility measured perpendicular to c-axis being higher than that along c-axis. The ZnO thin film transistors (TFTs) fabricated with devices aligned along and perpendicular to c-axis. The TFTs show high on-off ratio up to $\sim 10^9$. The field-effect mobility and transconductance of $\sim 35.5\text{cm}^2/\text{Vs}$ and 1.09mS/mm are obtained.

ACKNOWLEDGEMENTS

I want to acknowledge constant support and advice of Prof. Yicheng Lu during the entire course of my Ph.D. I also want to acknowledge the advice and help from Dr. Theo Siegrist from Bell Laboratories, Alcatel-Lucent Technologies; he helped me to clarify critical concepts in Stress-Strain analysis. I want to acknowledge the help from our collaborators Prof. Ulrike Diebold and Dr. Olga Dulub at the Physics Department at Tulane University for their help with the surface characterizations. Finally I want to acknowledge the help and support from my group members during the entire course of my stay here as a Ph.D. candidate.

DEDICATIONS

This work is dedicated to my family, especially my mother and father. This work would not have been possible without their constant support and encouragement.

TABLE OF CONTENTS

Abstract	ii
Acknowledgements	iv
Dedications	v
Table of Contents	vi
List of Tables	viii
List of Figures	ix
Chapter 1 Introduction	1 - 5
1.1 Motivation	1
1.2 Objectives of the work	3
1.3 Dissertation Organization	4
Chapter 2 Technical Background	6 - 32
2.1 Crystal properties	6
2.2 MOCVD Growth	10
2.3 Stress and Strain	16 - 21
2.3.1 Strain along different growth directions	17
2.3.2 a-plane ZnO on r-sapphire	19
2.4 Surface and Interface properties	21 – 27
2.4.1 Surface properties	21
2.4.2 Interface properties	26
2.5 Optical and Electrical properties	27
Chapter 3 MOCVD Growth Optimization	33 - 54
3.1 MOCVD system	33

3.2	Growth optimization of a-plane $\text{Mg}_x\text{Zn}_{1-x}\text{O}$ films	36 - 54
3.2.1	Mg in ZnO lattice	39
3.2.2	Mg composition	41
3.2.3	Morphology, Orientation and Crystal properties.....	43
3.2.4	Optical Properties	47
3.3	ZnO/ $\text{Mg}_x\text{Zn}_{1-x}\text{O}$ Heterostructure	50
Chapter 4	In-plane Strain Anisotropy In a-plane $\text{Mg}_x\text{Zn}_{1-x}\text{O}$	55 - 70
4.1	Strain with a-plane ZnO film thickness	59
4.2	Strain with Mg composition	63
4.3	Reciprocal space maps	65
Chapter 5	Interface And Surface Properties	71 - 100
5.1	Interface properties	71
5.2	Surface properties	77 - 100
5.2.1	Morphology anisotropy	77
5.2.2	Effect of substrate miscut	89
5.2.3	Effect of Growth Temperature	97
Chapter 6	Optical And Electrical Properties	101 - 113
6.1	Optical anisotropy	101
6.2	Electrical anisotropy	104
6.3	ZnO TFT - A feasibility study	107
Chapter 7	Conclusions and suggestions for future work	114 - 117
References	118 - 126
Curriculum Vitae	127

LIST OF TABLES

Table 2.1:	Elastic coefficients for bulk ZnO.....	17
Table 2.2:	Repeat distances \perp and \parallel to the c-axis of epitaxial ZnO on r-Al ₂ O ₃	20
Table 4.1:	Lattice parameters along orthogonal parameters $a[11\bar{2}0]$, $p[\bar{1}\bar{1}00]$ and $c[0001]$ axis, with variation in a-plane ZnO film thickness	59
Table 4.2:	Lattice parameters along orthogonal parameters $a[11\bar{2}0]$, $p[\bar{1}\bar{1}00]$ and $c[0001]$ axis, with variation in a-plane Mg _x Zn _{1-x} O film composition	64
Table 5.1:	The degree of miscut measured for R-1, R-2 and R-3.....	94
Table 6.1:	The extracted device parameters for the two in-plane directions.....	111

LIST OF FIGURES

Figure 2.1:	Shows (a) wurtzite crystal structure of ZnO, (b) crystal structure projection of ZnO along the [0001] as normal direction (Zn and O atoms are marked with arrows).....	7
Figure 2.2:	A set of orthogonal co-ordinate axis selected using a pair of perpendicular m-axis and a-axis.....	9
Figure 2.3:	Magnesium concentration (x) as a function of the ratio of Mg flow into the reactor.....	15
Figure 2.4:	Shows the step edges for polar and non-polar surface of ZnO.....	24
Figure 2.5:	Shows the bandgap lineup of ZnO and $\text{Mg}_x\text{Zn}_{1-x}\text{O}$	30
Figure 3.1:	Schematic of a MOCVD system for ZnO growth.....	35
Figure 3.2:	Schematic diagram of the axis-symmetric flow patterns in a rotating-disc vertical flow MOCVD reactor.....	35
Figure 3.3:	(a) Shows a schematic of the Zn plane in the wurtzite lattice of ZnO, (b) and shows the Auger scattering intensity observed from Zn and Mg atoms and O atoms, respectively with variation in the polar angle.....	40
Figure 3.4:	Shows a plot of % transmission versus wavelength (nm) for $\text{Mg}_x\text{Zn}_{1-x}\text{O}$ films with $x = 0, 0.18, 0.25, 0.34, 0.60$, respectively.....	42
Figure 3.5:	(a) and (b), shows the FESEM images of a ZnO and $\text{Mg}_{0.12}\text{Zn}_{0.88}\text{O}$ film on r-sapphire, respectively.....	45

Figure 3.6:	(a) and (b) show x-ray coupled scans for a-plane ZnO and Mg _{0.12} Zn _{0.88} O on r-sapphire, respectively.....	46
Figure 3.7:	Shows a plot of full width at half maximum (FWHM) of ω -rocking curves and detector scans of a-plane ZnO films with variations in deposition temperature.....	48
Figure 3.8:	Shows the room temperature PL spectra for a-plane Mg _x Zn _{1-x} O (x = 0, 0.08, and 0.12) films on r-sapphire substrate, the intensities of the peaks were normalized for comparison between different film compositions.....	49
Figure 3.9:	Shows the FESEM image of a ZnO-Mg _x Zn _{1-x} O single heterostructure.....	53
Figure 4.1:	(a) and (b) show schematic and lattice structure of a-plane ZnO film on r-sapphire substrate, respectively. (c) Shows orthogonal axes for a hexagonal unit cell.....	57
Figure 4.2:	(a), (b) and (c) show plots of lattice parameters a[11 $\bar{2}$ 0], p[1 $\bar{1}$ 00] and c[0001] on orthogonal axes with respect to the a-plane ZnO film thickness.....	61
Figure 4.3:	(a) Strain variation with a-plane ZnO films thickness, bulk ZnO lattice parameters used as reference, (b) plot of the c/a ratio and (c) Strain anisotropy $ (\epsilon_{ }/\epsilon_{\perp}) $ with a-plane ZnO film thickness.....	62
Figure 4.4:	(a), (b) and (c) show plots orthogonal axes lattice parameters	

	along $a[11\bar{2}0]$ and $p[1\bar{1}00]$ and $c[0001]$ of a-plane $Mg_xZn_{1-x}O$ film with Mg composition.....	66
Figure 4.5:	(a) Strain in a-plane $Mg_xZn_{1-x}O$ film, (b) Plot of theoretically calculated (c/a) ratio to measured (c/a) ratio and, (c) Strain anisotropy $ (\epsilon_{ }/\epsilon_{\perp}) $ and unit cell volume with Mg composition, reference relaxed lattice of bulk ZnO is used.....	67
Figure 4.6:	(a) and (b), shows the reciprocal space maps along a-plane ZnO ($20\bar{2}5$) and $Mg_{0.15}Zn_{0.85}O$ ($20\bar{2}5$) reflections, respectively.....	69
Figure 5.1:	(a) and (b) show the interface of non-polar ZnO film with r-sapphire and selected area diffraction (SAED) pattern from the film and the substrate, respectively.....	73
Figure 5.2:	(a) and (b) show the interface and SAED pattern from a non-polar $Mg_{0.30}Zn_{0.70}O$ films, respectively.....	74
Figure 5.3:	Shows (a) schematic of misfit dislocations at the epitaxial thin film – substrate interface, (b) Lattice schematic of the a-plane ZnO/r-sapphire interface with misfit dislocations.....	76
Figure 5.4:	(a) and (b) shows STM images of the film surface taken at 2000nm x 2000nm and 50nm x 50nm scale, respectively. The arrow shows the direction of c-axis.....	80
Figure 5.5:	Shows atomically resolved (20nm x 20nm) STM image of the non-polar ZnO film surface, respectively.....	82

Figure 5.6:	(a) and (b) shows STM images of the a-plane $\text{Mg}_{0.15}\text{Zn}_{0.85}\text{O}$ film surface taken at 2000nm x 2000nm and 50nm x 50nm scale, respectively. The arrow indicates the direction of in-plane c-axis.....	83
Figure 5.7:	Shows LEED pattern for varying Mg composition to analyze the surface ordering and crystallinity of a-plane $\text{Mg}_x\text{Zn}_{1-x}\text{O}$ films, with variation in Mg composition.....	87
Figure 5.8:	(a) Shows a log-log plot of rms roughness of a-plane ZnO films with film thickness, (b) shows a plot of rms roughness of a-plane $\text{Mg}_x\text{Zn}_{1-x}\text{O}$ films with Mg composition.....	88
Figure 5.9:	Shows a schematic of the substrate miscut, including the miscut angle (δ) and direction of the miscut.....	91
Figure 5.10:	Shows a schematic XRD four-circle configuration setup used for substrate miscut measurement, the figure also shows rotational degrees of freedom of the substrate with respect to the x-ray source and detector.....	91
Figure 5.11:	Shows the polar plots of a) R-1, b) R-2 and c) R-3, showing the direction of the miscut.....	93
Figure 5.12:	(a), (b) and (c) shows STM images for a-plane ZnO films at 500nm×500nm resolution, deposited on R-1, R-2 and R-3 respectively. The inset shows the roughness measured along (blue line) and perpendicular (red line) to in-plane c-axis.....	95

Figure 5.13:	Shows a plot of the rms surface roughness variation of the a-plane ZnO films with growth temperature.....	98
Figure 6.1:	Shows the transmission spectrum of a-plane (a) ZnO and (b) $\text{Mg}_{0.12}\text{Zn}_{0.88}\text{O}$ films with light polarization parallel and perpendicular to the c-axis, respectively.....	103
Figure 6.2:	Shows Hall mobility measurement (a) for a-plane $\text{Mg}_{0.08}\text{Zn}_{0.92}\text{O}$ films grown on r-sapphire substrates with magnetic field and (b) for a-plane $\text{Mg}_x\text{Zn}_{1-x}\text{O}$ films with Mg composition at magnetic field of 2000G.....	105
Figure 6.3:	(a) and (b) show the variation of average mobility and carrier concentration in a-plane ZnO films with deposition temperature and oxygen partial pressure in MOCVD, respectively.....	109
Figure 6.4:	Shows the schematic of the ZnO TFT device on r-sapphire.....	110
Figure 6.5:	(a) Shows the anisotropic $I_{\text{DS}} - V_{\text{DS}}$ characteristics, (b) shows anisotropic I_{DS} and g_m versus I_{GS} characteristics of the devices aligned along the two in-plane directions.....	112

CHAPTER 1: INTRODUCTION

1.1 MOTIVATION

Recently, wide band gap semiconductor materials, such as GaN are of significant interest for use in blue light emitting diodes, and short wave length laser diodes. Similar to GaN, ZnO has direct band gap of 3.34eV at room temperature. The high free excition binding energy of ~60meV as compared to 21-25meV for GaN, renders ZnO useful for applications in ultraviolet lasers and modulators [1, 2]. ZnO due to its large energy band gap is also suitable for fabrication of high temp and high power devices, where the typical operating temperature is above 200°C [3]. Optically pumped lasing action has also been observed in ZnO [4, 5] and it has been used as buffer layer for growth of GaN thin films because of its small lattice mismatch with GaN [6]. ZnO also has several other advantages including high radiation hardness [7] as compared to other wide band-gap semiconductor materials, availability of wet chemical etching, and compatibility with Si technology.

One of the key issues in modern solid-state electronics is the energy band engineering through design and fabrication of heterostructures, which leads to quantum confinement. The density of states is modified by the quantum confinement effects, which are partly responsible for some unusual properties of heterostructures. One of the ways to alter the bandgap of a semiconductor is to alloy it with a material of higher bandgap, while ensuring that the lattice constant of the semiconductor is matched with the substrate. This concept has been researched for most III-V semiconductors such as GaAs/AlGaAs, GaN/AlGaN etc., and the fabrication techniques have been well established. For fabricating a heterostructure using a ZnO active layer, bandgap

engineering is achieved by alloying ZnO with oxides of group II elements in the periodic table, i.e. Cd, Be, Mg, Ca, Sr [8]. ZnO can be alloyed with MgO to form high quality single crystal films having Mg content upto 33 at. % while retaining the wurtzite crystal structure [9, 10]. Alloying ZnO with MgO to form $\text{Mg}_x\text{Zn}_{1-x}\text{O}$ was found to increase the direct bandgap of ZnO from 3.3eV to about 4.0eV (for $\text{Mg}_{0.33}\text{Zn}_{0.67}\text{O}$), while still retaining the wurtzite crystal structure of ZnO [11]. ZnO/ $\text{Mg}_x\text{Zn}_{1-x}\text{O}$ based heterostructures have received a great deal of research attention in electronic and optoelectronic devices [12 – 17]. Ohtomo et. al. studied the structural properties of ZnO/ $\text{Mg}_x\text{Zn}_{1-x}\text{O}$ superlattices deposited on c-sapphire (0001) substrates with varying well widths [18]. Chia et. al. showed quantum confinement in ZnO/ $\text{Mg}_x\text{Zn}_{1-x}\text{O}$ multiple quantum wells on ScAlMgO₄ (0001) substrates, and studied the well width dependence on the radiative and non-radiative recombination times [19]. Recently, Koike et. al. studied the characteristics of ZnO/ $\text{Mg}_x\text{Zn}_{1-x}\text{O}$ heterostructure field-effect transistors grown on a-sapphire (0001) substrates [13].

In contrast to cubic close packed structure of most other semiconductors with four symmetry axes which cancel each other, ZnO's wurtzite crystal structure causes, ZnO and its alloys (e.g. $\text{Mg}_x\text{Zn}_{1-x}\text{O}$) to be polarized along the primary [0001] c-axis. Although, most of the ZnO based heterostructure and quantum well devices have been reported on c-axis oriented ZnO, like GaN the active layers of the devices grown with this orientation suffer from undesirable spontaneous and piezoelectric polarizations [20, 21]. The presence of these spontaneous and piezoelectric polarizations produce electrostatic fields which gives rise to Quantum-Stark Effect and thus cause spatial separation of the electrons and holes thus reducing their overlap and lowering of the quantum efficiency in

optoelectronic devices. Since, the a-plane and m-plane ZnO has equal number of cations and anions, the films oriented along these two directions are non-polar and thus it avoids the problem of spontaneous and piezoelectric polarization fields. Non-polar a-plane ZnO and $\text{Mg}_x\text{Zn}_{1-x}\text{O}$ films have been successfully grown using MOCVD [10, 22, 23]. Apart from the advantages of enhanced quantum efficiency and stable Schottky contacts, non-polar ZnO and $\text{Mg}_x\text{Zn}_{1-x}\text{O}$ films have in-plane structural, optical, acoustic [22] and electrical anisotropy. The presence of these anisotropic properties renders the a-plane ZnO, $\text{Mg}_x\text{Zn}_{1-x}\text{O}$ films and heterostructures useful for potential applications in various areas such as UV modulators.

Despite of all these advantages non-polar a-plane ZnO and $\text{Mg}_x\text{Zn}_{1-x}\text{O}$ films have not been studied in detail. Primarily due to the difficulties associated with growth of a-plane films and control of anisotropic strain, surface roughness and interface defects.

1.2 OBJECTIVES OF WORK

Current research in ZnO/ $\text{Mg}_x\text{Zn}_{1-x}\text{O}$ film based heterostructures and quantum wells is focussed on use of c-axis as the primary growth direction using c-sapphire and (0001) ScAlMgO_4 as primary substrates using Pulse-Laser Deposition (PLD), Molecular Beam Epitaxy (MBE) [16 - 19]. Even though significant advances have been made in this area using c-axis growth of heterostructures and quantum wells, the inherent limitation of quantum efficiency due to piezoelectric and spontaneous polarization fields would be a major issue in development of next generation optoelectronic devices. The use of non-polar a-axis and m-axis of the ZnO/ $\text{Mg}_x\text{Zn}_{1-x}\text{O}$ films would thus play a vital role in this area. Development of non-polar a-plane ($1\bar{1}20$) ZnO and $\text{Mg}_x\text{Zn}_{1-x}\text{O}$ films on r-sapphire

substrates have earlier been demonstrated using Metalorganic Chemical Vapor Deposition (MOCVD) technique. The non-polar growth however possesses anisotropy in in-plane physical properties. Although some of the in-plane anisotropic physical properties maybe advantageous for development of novel electronic, optical and acoustic devices [2, 22], in-plane anisotropy could also lead to poor surface, interface and structural properties. Some of the anisotropic properties are intrinsic to the hexagonal ZnO material system [23], while some such as surface structure and morphology, and interface property result from surface diffusion and growth energetics. The presence of anisotropic growth rate in ZnO [24] and strain relaxation leads to rougher a-plane ZnO surface as compared to c-plane, which adversely affects device design and fabrication. Currently, only limited information is available of study and control of the anisotropic properties in non-polar a-plane $\text{Mg}_x\text{Zn}_{1-x}\text{O}$ films.

The objectives of this research are (i) Growth optimization of epitaxial non-polar a-plane $\text{Mg}_x\text{Zn}_{1-x}\text{O}$ films on $(01\bar{1}2)$ r- Al_2O_3 (r-sapphire) substrates using metalorganic chemical vapor deposition technique (MOCVD), (ii) Comprehensive characterizations of in-plane anisotropic strain, surface and interface, optical and electrical properties and (iii) Demonstration of a prototype a-plane ZnO thin film transistor (TFT).

1.3 DISSERTATION ORGANIZATION

After describing the motivation and the importance of the related work in Chapter 1, Chapter 2 covers a background of the crystal structure, thin film growth, strain, surface and interface, and optical properties. In Chapter 3, a brief description of the MOCVD equipment used for the growth of non-polar a-plane ZnO and $\text{Mg}_x\text{Zn}_{1-x}\text{O}$ films on r-

sapphire substrates is discussed followed by growth optimization and properties of a-plane $\text{Mg}_x\text{Zn}_{1-x}\text{O}$ films. Chapter 3 also includes brief introduction and feasibility of $\text{ZnO}/\text{Mg}_x\text{Zn}_{1-x}\text{O}$ heterostructures. Chapter 4 presents the analysis of strain properties including in-plane anisotropy in strain. Chapter 4 also discusses reciprocal maps (RSMs) used to determine crystal quality of a-plane thin films. Chapter 5 analyzes the anisotropic surface and interface properties. Chapter 6 focuses on optical and electrical anisotropy in the films followed by device feasibility to study anisotropic device behavior of ZnO thin film field effect transistors (TFTs). Finally, Chapter 7 summarizes the work accomplished with recommendation for future research in the field.

CHAPTER 2: TECHNICAL BACKGROUND

2.1 CRYSTAL PROPERTIES

ZnO is an oxide of the group II metal Zinc, which belongs to $P6_3mc$ space group. ZnO is on the borderline between a semiconductor and an ionic material. In most of the growth conditions ZnO stabilize as n-type semiconductor with wurtzite structure (hexagonal symmetry). Figure 2.1 (a) Shows the wurtzite crystal structure of ZnO, and (b) shows crystal structure projection of ZnO along the $[0001]$ as normal direction (Zn and O atoms are marked with arrows). The wurtzite crystal structure has hexagonal unit cell with two lattice constants, 'a' and 'c'. An ideal wurtzite crystal consists of two interpenetrating hexagonal close packed (HCP) structures, with one type of atoms in each separated by $3c/8$, which in case of ZnO is $u = 0.3825$ (fractional coordinates). Even though it is tetrahedrally bonded, similar to other semiconductors, the bonds have a partial ionic character. The lattice parameters of ZnO are $a = 0.324982\text{nm}$ and $c = 0.520661\text{nm}$ at 300K, with a c/a ratio of 1.602 which is close to 1.633 of ideal hexagonal close-packed structures. In the direction parallel to the c-axis Zn–O distance is 0.1992nm and in all the other three directions of the tetrahedral arrangement of nearest neighbors it is 0.1973nm . In a unit cell zinc occupies the $(0,0,0.3825)$ and $(0.6667,0.3333,0.8825)$ positions and oxygen occupies the $(0,0,0)$ and $(0.6667,0.3333,0.5)$ positions [25]. The close-packed (0001) planes are made up of two sub-planes (A & a), each consisting of either the cationic (Zn) or the anionic (O) species. The crystal can be considered to have the stacking sequence. ...AaBbAaBb.... as compared to. ...AaBbCcAaBbCc.... in diamond cubic (silicon) and sphalerite (GaAs etc.,). In the hexagonal crystal system, a four-axis coordinate system is used to identify the various planes and directions.

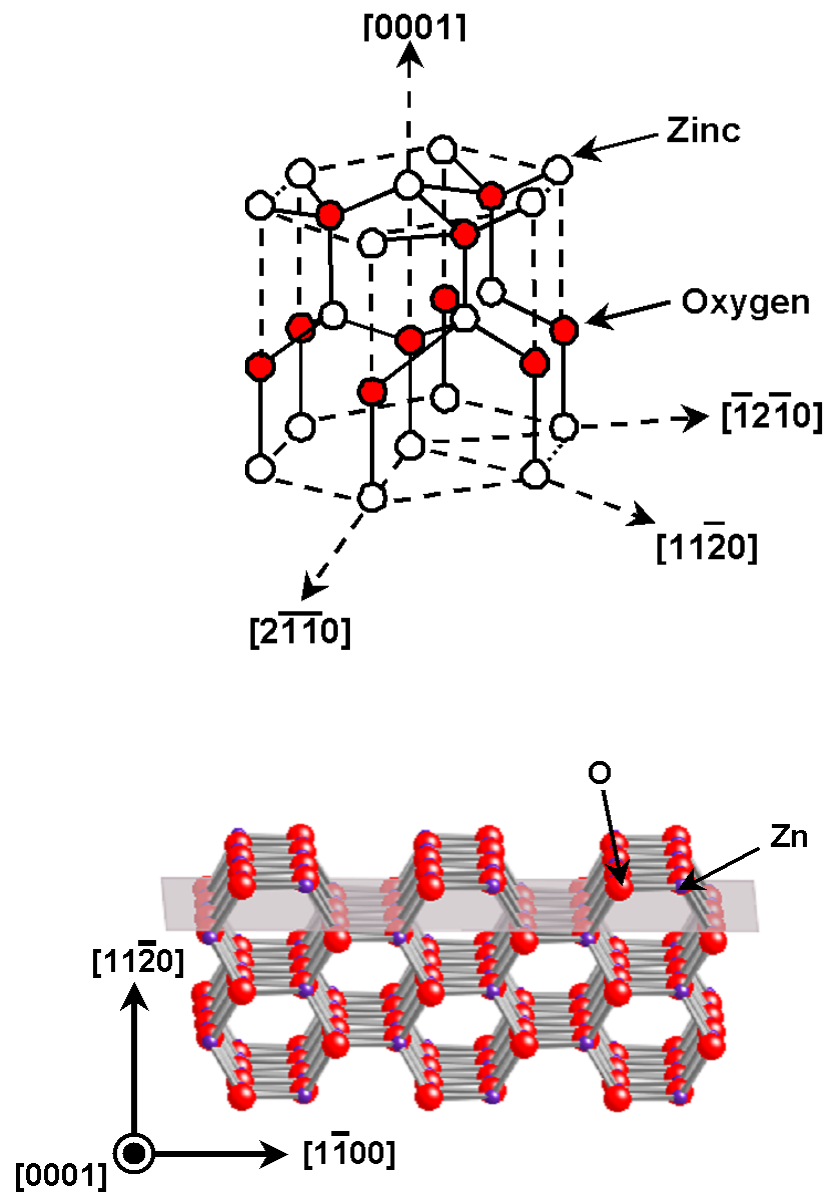


Figure 2.1: Shows (a) the wurtzite crystal structure of ZnO, (b) crystal structure projection of ZnO along the $[0001]$ as normal direction.

The four indices are called the Miller-Bravais indices, and a plane is defined by 4 indices, i.e., $(h\ k\ i\ l)$. As the three basis vectors are in-plane with an angle of 120° to each other, it follows $-i = h+k$. The planes of the same family are identified by permutations of the first three indices. There are 2 c-planes (0001) , 6 m-planes $(1\bar{1}00)$ and 6 a-planes $(11\bar{2}0)$ as can be seen in Fig. 2.2 [26]. The c-plane is normal to any of the m or a-planes, there is always a pair of m and a-plane orthogonal to each other. The c-plane is a polar plane of the wurtzite crystal structure and is O or Zn terminated. The m and a-planes are non-polar because in these planes there is an equal number of cations and anions. This structure does not possess a center of symmetry. The lack of inversion symmetry leads to ZnO being a piezoelectric material and the polarity of the c-axis results in the Zn-terminated and O-terminated planes to display vastly different properties.

$\text{Mg}_x\text{Zn}_{1-x}\text{O}$ can be used as barrier layer for the ZnO-based heterostructures. Earlier, Ohtomo et. al. showed ZnO can be alloyed with MgO to form $\text{Mg}_x\text{Zn}_{1-x}\text{O}$, while still retaining the wurtzite crystal structure of ZnO till $\text{Mg \%} = 0.33$ and have also shown that the epitaxial films having Mg up to $x = 0.15$ are thermodynamically stable up to about 700°C [27]. MgO belongs to the space group $\text{Fm}\bar{3}\text{m}$ with lattice parameter $a = 4.215\text{\AA}$ and stabilizes with a cubic rocksalt structure. MgO is octahedrally bonded having a 6-fold coordination with Mg–O distance of 2.1075\AA . The lattice consists of interpenetrating face centered cubic lattices, separated along the c-axis by $u = 0.5$ (fractional coordinates). While oxygen (by convention) occupies the $(0,0,0)$ and $(0.5,0.5,0)$ positions, magnesium occupies the $(0,0,0.5)$ and $(0.5,0.5,0.5)$ positions [25]. When the wurtzite lattice is relaxed, $c/a = 1.204$ and $u = 0.5$. This implies that the Mg and O atoms lie in the same plane.

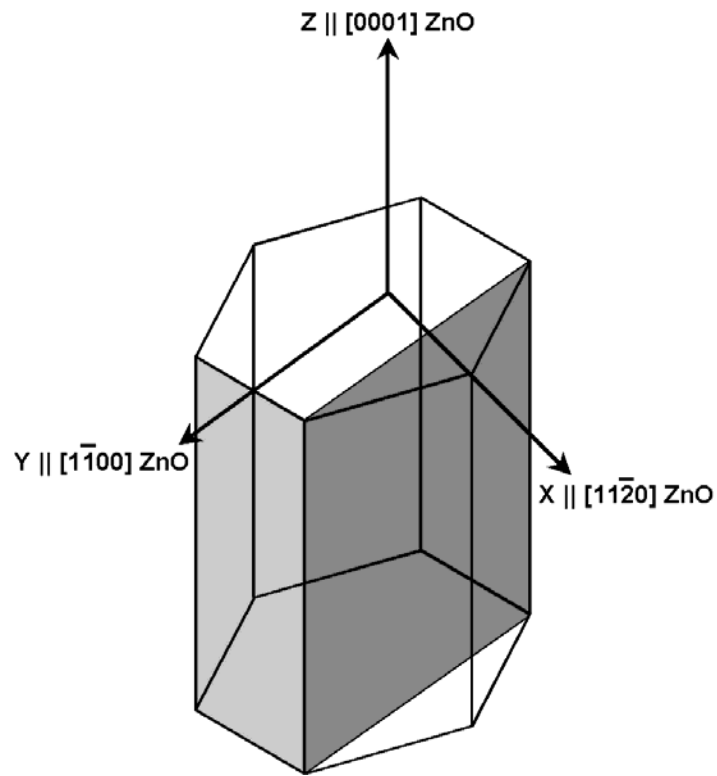


Figure 2.2: A set of orthogonal co-ordinate axis selected using a pair of perpendicular m-axis and a-axis.

The tetrahedrally coordinated and octahedrally coordinated Zn^{2+} ion radii are very close to the tetrahedrally coordinated and octahedrally coordinated Mg^{2+} ionic radii respectively. Thus Mg atom has been found to substitute the Zn atom in tetrahedral coordination leading to distortion of the wurtzite ZnO lattice in the $\text{Mg}_x\text{Zn}_{1-x}\text{O}$ films [11]. Mg incorporation reduces the c-axis lattice parameter of ZnO according to $c = 0.5204 - 0.017x$ nm, while increasing the a-axis lattice parameter by $a = 0.324 + 0.0036x$ nm [9, 14].

2.2 MOCVD GROWTH

Several groups using different growth techniques including PLD, sputtering, MBE, CVD and MOCVD have reported ZnO film growth [10, 16-19, 22, 23]. The most commonly reported substrates for ZnO film growth have been c-sapphire, ScAlMgO_4 etc. The growth on these substrates lead to polar (0001) oriented ZnO films. Since, (0001) plane has the highest energy amongst all the low-index planes, the growth rate along the c-direction is the highest [24, 28]. So, the ZnO crystals are elongated in the [0001] direction and the prismatic sides of the crystals are usually the $\{10\bar{1}0\}$ or $\{11\bar{2}0\}$ planes. Thus, even under non-epitaxial conditions it is very easy to obtain c-axis oriented films on almost any substrate.

Metalorganic chemical vapor deposition (MOCVD) is different from the conventional CVD in the choice of precursors of the reacting species. At least, one precursors used for the MOCVD growth is a metal-organic. These metalorganics have only one dangling bond and can be converted to chemical vapors easily. This allows easy handling of the reactant species. Use of metalorganic precursors allows the use of very

low growth temperatures, depending on the vapor pressure of the precursor. Better control in composition during growth is also achieved [29-31].

MOCVD has better control over thermodynamic control of reactions, uniformity in deposition as well as in-situ doping concentrations. MOCVD also leads to better stoichiometry as compared to most other chemical deposition technologies (CVD, PECVD etc.), primarily due to lower decomposition temperature of the metalorganics. Another advantage of using metalorganics instead of metal vapors is that they do not condense on the chamber walls at room temperatures. Hence, the “line-of-sight” geometry that is required for metal vapors is not necessary when using metalorganics. Moreover, while direct condensation is the growth method when using metal vapors, in MOCVD the reactants adsorb on the substrate surface and chemically react with one another. Thus additional control of the growth process is possible through the chemical interactions amongst the sources as well as due to interaction between the sources and the substrate. Chemical vapor deposition (CVD) is a process based on pyrolytic reactions. The precursors used in the CVD system compounds with a reasonable vapor pressure. A carrier gas, usually O_2/N_2 , carries the vapors of the reacting species. The reaction then proceeds on the substrate surface. The susceptor mechanically supports the substrate and also serves as the source of thermal energy for the reaction. It is heated to the required temperature, using induction-heating coil.

Most elements when attached to organic functional groups such as (CH_3 , C_2H_5 , etc.,) have high vapor pressure. These metalorganic molecules ($(CH_3)_3Ga$, $(C_2H_5)_2Zn$, etc.,) have only one dangling bond and can be converted to chemical vapors by reaction. Hence MOCVD is a process whereby one or more of the reactants that is a metalorganic,

get adsorbed on the substrate surface, then react chemically to deposit the desired compound on the substrate.

The main steps in the growth of film by MOCVD are:

- a. Convective transport of source gases/metalorganics from the injected or entry point in the reactor to the substrate.
- b. Diffusion transport of the gases through the relatively stationary “boundary layer” formed at the substrate surface due to viscous friction to gaseous flow close to the substrate surface.
- c. Adsorption of the gaseous species onto the substrate surface.
- d. Diffusion and chemical reaction of the various species on the surface resulting in deposition.
- e. Desorption of product organic species such as CH_4 , H_2 , etc.,

Based on the above sequence of events two rate limiting steps are possible. At low temperatures, the rate of the surface reactions is reduced and the deposition is surface-reaction-rate-limited (c, d, & e). At higher temperatures, transport of the gaseous species through the boundary layer is rate limiting, and hence deposition is mass-transport-limited (a, & b). Use of metalorganics is advantageous over the use of metal vapors, because they do not condense on the chamber walls at room temperatures. Hence, the “line-of-sight” geometry required for metal vapors (i.e. the substrate should be in the direct line of sight of the vapor source), is not necessary for metalorganics. Thus MOCVD also provides additional control of the growth process, through the chemical interactions amongst the sources as well as due to interaction between the sources and the substrate.

Commonly used precursors for zinc and oxygen are Dimethyl Zinc $[(\text{CH}_3)_2\text{Zn}]$ and Diethyl Zinc $[(\text{C}_2\text{H}_5)_2\text{Zn}]$, and CO_2 , O_2 , N_2O , and H_2O , respectively. The covalent compounds of Zinc are amongst the most volatile organometallic compounds. Zn with carbon forms a covalent compound with sp-hybridization. Though Dimethyl Zinc can be used to achieve high growth rate due to higher vapor pressure, Diethyl Zinc is more advantageous due to the following reasons:

- i) Dimethyl Zinc reacts more vigorously with O_2 and H_2O as compared to Diethyl Zinc, thus it is more difficult to limit the gas phase reactions.
- ii) Using Diethyl Zinc lowers the possibility of carbon contamination. At the substrate temperature of $\sim 400^\circ\text{C}$, unlike Dimethyl Zinc, Diethyl Zinc adsorbed on the surface of the substrate, results in Zn metal and eliminates the reduced ethyl group as ethylene.

The melting point of DEZn is -28°C and the boiling points are 117°C and 30°C at pressures of 760mm Hg and 27mm Hg respectively. The strongly electrophilic (accepts an electron) character of zinc largely determines the chemical behavior of these compounds. They are electron deficient compounds in that the number of low-lying orbitals available for bonding (four) is greater than the number of bonding electron pairs (two). This presence of vacant orbitals for bonding explains the tendency of DEZn to form complexes with compounds containing hetero-atoms with free electron pairs (O, N, P, S etc.). At the same time this serves to explain the great chemical reactivity of DEZn. DEZn is highly susceptible to attack by oxygen and water.

Bis-(methylcyclopentadienyl)magnesium (MCp_2Mg) has a melting point of 29°C and its boiling point is 56°C at 0.3mm Hg. The alternate commercially available Mg

precursor is Bis-(cyclopentadienyl)magnesium (Cp_2Mg) which, when pure, is a white solid that melts at $\sim 281^\circ\text{C}$. Use of this compound often requires additional purification when received from vendors if reproducible doping results are to be obtained [32], which can be time consuming and expensive. MCp_2Mg , while structurally similar to Cp_2Mg , the MCp_2Mg has a lower melting point (29°C), permitting the source to be used as a liquid and without any complicated purification process [32]. Therefore, MCp_2Mg is the most common magnesium precursor of choice for MOCVD growth of II-VI compounds. Both the precursors react pyrophorically when exposed to air.

Gorla et. al. and Muthukumar et. al. have earlier published information on Rutgers MOCVD system, with details on precursor selection etc. [33, 34]. Earlier, Muthukumar et. al. demonstrated a-plane $\text{Mg}_x\text{Zn}_{1-x}\text{O}$ films on r-sapphire substrate using MOCVD. It was shown that a $\sim 5\text{nm}$ ZnO film buffer is required retain the wurtzite crystal structure in a-plane $\text{Mg}_x\text{Zn}_{1-x}\text{O}$ films [11]. It was also observed that the composition (x) of the $\text{Mg}_x\text{Zn}_{1-x}\text{O}$ films is a function of the ratio of the Mg/Zn flow into the reactor keeping the O_2 flow constant, substrate temperature, and the chamber pressure [33]. Figure 2.3 shows the dependence of Mg composition (x) on Mg/Zn metalorganic gas-flow ratio. For films grown below 375°C the Mg incorporation was very low and did not increase with Mg flow and for films grown above 375°C Mg incorporation increased linearly with increasing Mg flow till $x = 0.3$ and then decreased. As the vapor pressure of MCp_2Mg is much lower than the vapor pressure of DEZn it is difficult to get high Mg incorporation in the films without compromising the growth rate.

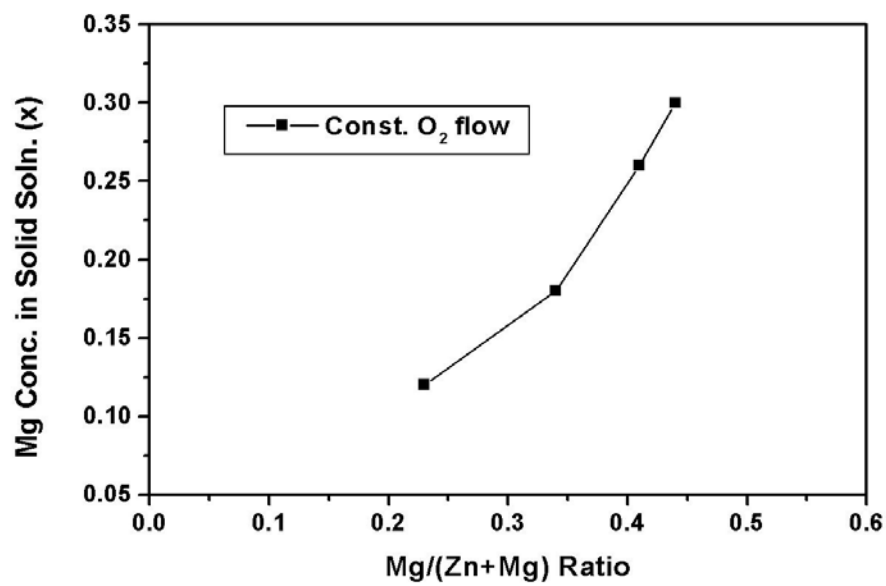


Figure 2.3: Magnesium concentration (x) as a function of the ratio of Mg flow into the reactor [33].

2.3 STRESS AND STRAIN

Strain is defined as deformation in solids and is described in terms of continuous deformation field $\mathbf{u}(\mathbf{r})$, which defines the vector displacement, where \mathbf{r} corresponds to the position vector $\mathbf{r} = r(x, y, z)$. Then symmetric strain tensor ϵ_{ij} is related to the displacement field according to equation 2.1:

$$\epsilon_{ij} = \frac{1}{2} \left(\frac{du_j}{dx_i} + \frac{du_i}{dx_j} \right) \quad (2.1)$$

Where, $i, j = 1, 2$ and 3 are the spatial directions. For sufficiently small stress σ , strain is proportional to the magnitude of applied stress according to the Hooke's law, given by equation 2.2:

$$\sigma_{ij} = C_{ijkl} \epsilon_{ij} \quad (2.2)$$

Where, C_{ijkl} are the stiffness coefficients, and $i, j, k, l = 1, 2$ and 3 . Due to symmetry of the stress and strain tensors, the elastic stiffness coefficients follow the following properties: $C_{ijkl} = C_{jikl} = C_{ijlk}$. The equalities of the first two and the last two suffixes reduce the independent stiffness coefficients to 36. It can also be shown that $C_{ijkl} = C_{klij}$. This relation further reduces the number of constants to 21. The crystal symmetry of a wurtzite crystal further reduces the number of coefficients required to 5 [14].

Stress-Strain tensor for wurtzite crystal:

$$\begin{pmatrix} \sigma_{xx} \\ \sigma_{yy} \\ \sigma_{zz} \\ \sigma_{yz} \\ \sigma_{xz} \\ \sigma_{xy} \end{pmatrix} = \begin{pmatrix} C_{11} & C_{12} & C_{13} & 0 & 0 & 0 \\ C_{12} & C_{11} & C_{13} & 0 & 0 & 0 \\ C_{13} & C_{13} & C_{33} & 0 & 0 & 0 \\ 0 & 0 & 0 & C_{44} & 0 & 0 \\ 0 & 0 & 0 & 0 & C_{44} & 0 \\ 0 & 0 & 0 & 0 & 0 & C_{66} \end{pmatrix} \begin{pmatrix} \epsilon_{xx} \\ \epsilon_{yy} \\ \epsilon_{zz} \\ \epsilon_{yz} \\ \epsilon_{xz} \\ \epsilon_{xy} \end{pmatrix} \quad (2.3)$$

Assuming the shear component to be zero ($\sigma_{xy} = \sigma_{xz} = \sigma_{yz} = 0$), the tensor can be reduced to:

$$\begin{pmatrix} \sigma_{xx} \\ \sigma_{yy} \\ \sigma_{zz} \end{pmatrix} = \begin{pmatrix} C_{11} & C_{12} & C_{13} \\ C_{12} & C_{11} & C_{13} \\ C_{13} & C_{13} & C_{33} \end{pmatrix} \begin{pmatrix} \varepsilon_{xx} \\ \varepsilon_{yy} \\ \varepsilon_{zz} \end{pmatrix} \quad (2.4)$$

Since, ZnO is a wurtzite crystal that belongs to the crystal group 6mm, the stress-strain tensor for ZnO films would be as shown in equation 2.4.

Table 2.1: Elastic coefficients for bulk ZnO [14]

Elastic constants for wurtzite ZnO	GPa
C_{11}	217
C_{12}	117
C_{33}	225
C_{13}	121
C_{44}	50

2.3.1 STRAIN ALONG DIFFERENT GROWTH DIRECTIONS:

(a) c - axis growth

Growth along the c-axis is along the z-axis, which is parallel to the c-axis [0001] (based on the defined in the figure 2.2). The stress component along the growth axis i.e. z-axis, $\sigma_{zz} = 0$, as the growth direction has freedom of expansion or contraction. The in-plane strain in case of ZnO grown on c-sapphire or GaN substrate in such a case would

be isotropic due to the hexagonal symmetry of the substrate, thus $\varepsilon_{xx} = \varepsilon_{yy}$. Thus the matrix can be modified according to:

$$\begin{pmatrix} \sigma_{xx} \\ \sigma_{yy} \\ \sigma_{zz} \end{pmatrix} = \begin{pmatrix} (C_{11} + C_{12})\varepsilon_{\parallel} + C_{13}\varepsilon_{\perp} \\ (C_{12} + C_{11})\varepsilon_{\parallel} + C_{13}\varepsilon_{\perp} \\ 2C_{13}\varepsilon_{\parallel} + C_{33}\varepsilon_{\perp} \end{pmatrix} \quad (2.5)$$

Where, $\varepsilon_{\parallel} = \varepsilon_{xx} = \varepsilon_{yy}$, and $\varepsilon_{\perp} = \varepsilon_{zz}$.

Thus for c-axis oriented growth of ZnO on c-sapphire or GaN substrate/ template, the in-plane stress would be uni-axial due to in-plane symmetry of the underlying substrate.

$$\sigma_{xx} = \sigma_{yy} = (C_{11} + C_{12})\varepsilon_{\parallel} + C_{13}\varepsilon_{\perp} \quad (2.6)$$

And,

$$\sigma_{zz} = 0 = 2C_{13}\varepsilon_{\parallel} + C_{33}\varepsilon_{\perp} \quad (2.7)$$

The relation in this equation leads to the Poisson's ratio (ν):

$$\nu = \frac{\varepsilon_{\perp}}{\varepsilon_{\parallel}} = \frac{-2C_{13}}{C_{33}} \quad (2.8)$$

And, the ratio of the in-plane stress to strain is known as the Young's Modulus (Y) and is give by:

$$Y = \frac{\sigma_{\parallel}}{\varepsilon_{\parallel}} = (C_{11} + C_{12}) - \frac{2C_{13}^2}{C_{33}} \quad (2.9)$$

(b) a - axis growth

For a-plane ZnO growth in-plane strain would be anisotropic along c-axis [0001] and along m-axis [$\bar{1}100$], because the unique c-axis of ZnO is in-plane of the substrate and the growth direction is perpendicular to both the c-axis as well as the m-axis leading to biaxial in-plane stress. The in-plane anisotropic strain also results from anisotropic substrate lattice parameters in the growth plane (r-sapphire ($01\bar{1}2$) in this case). The out

of the plane stress i.e. along the growth direction $[11\bar{2}0]$ ZnO is zero ($\sigma_{xx} = 0$), since this is the direction of free growth, which is able to accommodate any contraction or expansion. However, in-plane stress components are not leading to a bi-axial in-plane stress ($\sigma_{zz} \neq \sigma_{yy}$).

The resulting matrix in such case would be:

$$\begin{pmatrix} \sigma_{xx} \\ \sigma_{yy} \\ \sigma_{zz} \end{pmatrix} = \begin{pmatrix} C_{11}\epsilon_{xx} + C_{12}\epsilon_{yy} + C_{13}\epsilon_{zz} \\ C_{12}\epsilon_{xx} + C_{11}\epsilon_{yy} + C_{13}\epsilon_{zz} \\ C_{13}(\epsilon_{xx} + \epsilon_{yy}) + C_{33}\epsilon_{zz} \end{pmatrix} \quad (2.10)$$

Which then results in the relationship between the elastic coefficients and strain as:

$$\epsilon_{xx} = - \left(\frac{(C_{12})\epsilon_{yy} + C_{13}\epsilon_{zz}}{C_{11}} \right) \quad (2.11)$$

(c) *m* - axis growth

The growth along *m*-axis ZnO would require similar calculations with the subscript ‘xx’ replaced by subscript ‘yy’ in the matrix representation leading to the relation:

$$\epsilon_{yy} = - \left(\frac{C_{12}\epsilon_{xx} + C_{13}\epsilon_{zz}}{C_{11}} \right) \quad (2.12)$$

Since in this case, ($\sigma_{yy} = 0$) and ($\sigma_{zz} \neq \sigma_{xx}$).

2.3.2 a-PLANE ZnO ON r-SAPPHIRE

It is important to study the strain and relaxation in non-polar ZnO and $\text{Mg}_x\text{Zn}_{1-x}\text{O}$ films, because strain affects both the physical properties as well as device performance. A relaxed non-polar ZnO film lacks piezoelectric and spontaneous polarization fields, which are only present along the polar $[0001]$ axis due to lack of inversion symmetry. Presence of strain however distorts the unit cell and thus affects the polarization fields in

the films (to be discussed in detail in later sections). Furthermore, physical properties such as surface morphology, interface misfit dislocations and optical properties are also directly affected by strain and relaxation anisotropy in the films. Table 2.2 shows the in-plane repeat distance along and perpendicular to c-axis of ZnO. The calculated value of the lattice mismatch along in-plane c-axis ([0001] direction) is only 1.53%, while the lattice mismatch along the in-plane m-axis ($[1\bar{1}00]$ direction) of ZnO is $\sim 18.3\%$.

Table 2.2: Repeat distances \perp and \parallel to the c-axis of ZnO on r-Al₂O₃ [33].

Material	Structure	Lattice Parameters (Å)	Thermal Expansion Coefficient @ 500°C (10^{-6} K^{-1})	Repeat distance \perp c-axis of ZnO (Å)	Repeat distance \parallel c-axis of ZnO (Å)
ZnO	Wurtzite (hexagonal)	a = 3.2498 c = 5.20661	a = 8.2 c = 4.9	a _{ZnO} = 3.2498	c _{ZnO} /2 = 2.601
r-Al ₂ O ₃	Rhombohedral (hexagonal packing of oxygen)	a = 4.7587 c = 12.9929	a = 7.1 c = 8.0	a _{sapphire} /√3 = 2.747	$\frac{1}{6}\sqrt{3a_{sapphire}^2 + c_{sapphire}^2}$ = 2.5645

Earlier, Pérez et. al. reported the in-plane and out of the plane stress and strain calculation for a-plane Cd_xZn_{1-x}O films grown on r-sapphire substrates [35]. In order to obtain a change in the lattice parameters for Cd_xZn_{1-x}O grown on R-sapphire substrate, reciprocal space maps were carried out around ZnO (20 $\bar{2}$ 0) and ZnO (11 $\bar{2}$ 2) reciprocal lattice points. The reciprocal space maps along with the coupled scan along the ZnO

($11\bar{2}0$) indicated a change in the periodicity along the c-axis (corresponding the c-lattice parameter) and along ZnO ($11\bar{2}0$) (corresponding to a-lattice parameter). It was observed that the strain distribution in the ZnO film on R-sapphire is anisotropic with larger tensile strain along the $[1\bar{1}00]$ compared to a much smaller compressive strain along $[0001]$. It was also observed that the strain is completely relaxed along the $[0001]$ axis for a ZnO film thickness of $\sim 800\text{nm}$. Furthermore, the strain in the films was directly co-related to the Cd concentration.

2.4 SURFACE AND INTERFACE PROPERTIES

2.4.1 SURFACE PROPERTIES

The polar and non-polar surfaces of ZnO show vast differences in structural, optical as well as electronic properties. The presence of anisotropic kinetics in ZnO [24] and strain relaxation leads to rougher a-plane ZnO surface as compared to c-plane, which adversely affects device design and fabrication. Dulub et. al. studied the surface properties and stability of different planes of bulk ZnO crystal and found that the non-polar surfaces of ZnO are rougher as compared to the polar surfaces, with anisotropic features oriented parallel to the crystallographic c-axis [28, 36]. The observed ‘needles-shaped domains consisted of terraces with long-straight step edges parallel to the c-axis. Such step edges can be considered as $(10\bar{1}0)$ -oriented facets with a very low surface energy. Recently, it was also observed that for oxide surfaces, the surface energy of a step edge from a parent facet is sufficient for step formation [37, 38]. However, the step edges that run perpendicular to the small terraces represent small c-plane facets and are expected to have a higher surface energy. Diebold et. al. earlier reported that the root

mean square (rms) surface roughness of the non-polar ($11\bar{2}0$) ZnO surface is higher than the polar (0001) ZnO surface with deep groves and steep (0001) oriented sides [36, 37]. It was observed that these surfaces have higher surface energy and are less stable as compared to the polar (0001) and ($000\bar{1}$) surfaces. The non-polar ($11\bar{2}0$) surfaces were observed to have equal number of cations and anions as expected.

Surface structure and morphology depend on formation energy of the various planes, growth kinetics and strain-relaxation of the films. In addition to kinetic considerations (anisotropic surface/bulk diffusion; the influence of a dislocation network at the interface, strain-related effects), step edges are known to play a major role in surface chemistry and growth processes [38]. At the atomic scale, a thin film surface consists of terraces with monoatomic step edges. In case of ZnO, the step edges of these terraces that run parallel to the c-axis contain an equal number of Zn and O ions, and are non-polar. The step edges that are perpendicular to the c-axis are polar and terminated with either exclusively O or exclusively Zn atoms. Figure 2.4 shows the step edges for polar and non-polar surface of ZnO. These step edges have a high surface energy and that the attachment of Zn and O entities occurs at quite different rates at each of them.

The surface and interface situation will be different when Mg is incorporated into the films. The kinetic parameters mentioned above, as well as the interface strain/stress and dislocation network could be quite different. For example, Mg has lower surface diffusion rate as compared to Zn affecting the overall growth kinetics, furthermore it is possible that Mg can segregate at the surface thus affecting the overall morphology. Also, since MgO alloying with ZnO changes the lattice parameters as seen in the previous section, Mg incorporation and composition would directly affect the

interface dislocation network. This would not only be important for the resulting film morphology and interface properties, but also be particularly important for the fabrication of heterostructures, as the band offset would be a sensitive function of the local stoichiometry at the interface. Apart from these factors fluctuations in surface morphology lead to electrostatic fields that have a direct impact on the quantum confinement in both HFETs as well as quantum wells. Large surface morphology fluctuations and anisotropic surface roughness also presents difficulties towards metallization and device fabrication.

Apart from growth kinetics and energy considerations some of the other issues that significantly affect the surface morphology in thin films include the substrate roughness and miscut. There is ample evidence in the literature that miscut of the starting substrate has significant influence on the surface morphology of deposited thin films. In case of Si/Ge systems the presence of substrate miscuts have been observed to lead to anisotropic surface roughness, aligned in a particular crystallographic direction. The roughness is aligned along the azimuth of the miscut direction [39 - 41]. The alignment along a particular direction could result from the energy considerations, assuming the miscut direction to have lower barrier to formation as compared to the surface without any miscut. In a specific case of 20 layers of Si/Ge deposited on 4.3° miscut Si substrate, it was observed that the roughness bumps are flattened along the direction where the local slope brings the surface in close alignment with the (001) surface [39].

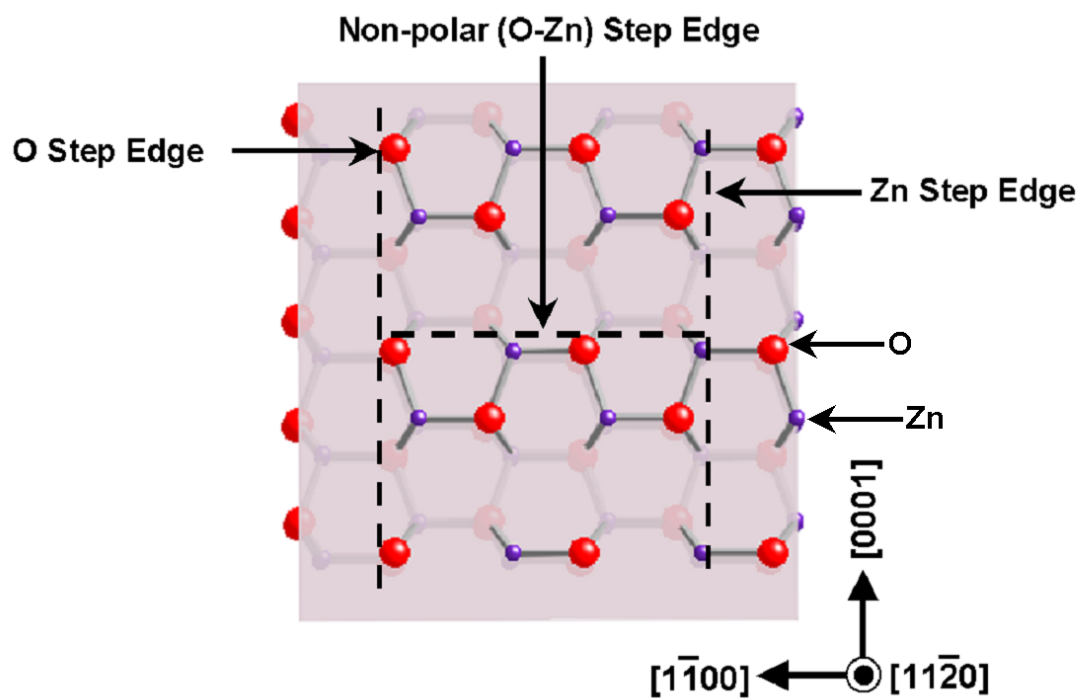


Figure 2.4: shows the step edges for polar and non-polar surface of ZnO

In certain cases the miscut substrates actually leads to smoother films compared to use of on-axis substrates [40]. Anisotropy in the surface roughness morphology is still observed. In another case, for a Ge film deposited on Si (001) substrate. Again the miscut direction showed lower roughness compared to the orthogonal in-plane direction. Reduced roughness compared to on-axis substrates is associated with lower step bunching [41] generally observed in the Si/Ge systems. Roughness could also be reduced due to difference in the crystal growth rates along the different directions. So on a miscut substrate that the growth difference is proportionally averaged between the normal and the in-plane orientation as compared to the on-axis substrates where the difference in the growth rates is maximum [40]. After considering a 4-fold symmetry cubic system like Si/Ge that lacks inherent structural anisotropy, it is relevant to consider GaN on sapphire and SiC systems for more comprehensive understanding. Since, the structure of GaN is similar to ZnO, analysis of effect of substrate miscut on surface morphology in these systems is important. For c-axis (0001) oriented GaN films deposited on different miscut a-plane sapphire substrates, it was observed that lowest rms roughness of $\sim 0.13\text{nm}$ was obtained for substrates with miscut $\sim 0.25^\circ$ [42]. Increase or decrease in the miscut in the miscut angle of the a-plane sapphire resulted in rougher surface. However, roughness anisotropy was not significant in these films. Indicating that the substrate miscut decides the orientation and the vertical correlation length causing roughness anisotropy but the lateral correlation lengths may depends on other key factors. Substrate miscut was also found to significantly affect the x-ray and optical properties of the films. However the films with lowest rms roughness did not show best optical properties as observed by photoluminescence (PL). Even in case of (0001) GaN films deposited on close lattice

matched (0001) SiC-4H substrates, the substrate miscut have been shown to have significant effects on the optical properties [43]. These results suggest that the quantum wells and heterostructures require careful design of the substrate miscut for optimum surface and interface roughness, and still achieve high confinement efficiency. In other reports of deposition of a-plane GaN films on r-sapphire substrates it has been observed that a decrease in substrate miscut from 1.05° to 0.5° resulted in significant reduction of the surface roughness vertical correlation, although the lateral correlation was not changed significantly [44, 45]. The cause of the change in the vertical correlation length could be due to the tilt in the grains of the film along the substrate miscut, while the lateral correlation length may be inherent to the crystal structure and the growth kinetics.

2.3.2 INTERFACE PROPERTIES

A study of the interface properties is important to understand the defect formation at the interface between the film and the substrate, and also at hetero-interfaces. The presence of defects such as misfit dislocations, threading dislocations, or stacking faults are associated with the crystal growth and structural integrity of the films, which have a direct impact on the optical and electrical properties. Several groups have studied the interface properties of the polar ZnO films grown on c-sapphire substrates. There have been few reported works including ours, on the interface properties of non-polar ZnO films. Unlike GaN, c-oriented ZnO films do not show basal plane stacking faults. However, as observed by Vigue et. al. for ZnO films deposited on c-sapphire substrates. The threading dislocations are mostly oriented along the c-axis, some even forming dislocation loops. They also observed three different kinds of threading dislocations

primarily a-type, a+c-type and c-type. The overall defect density was found to be around $4 \times 10^{10} \text{ cm}^{-2}$ [46]. However, Gerthsen et. al. deposited c-axis oriented ZnO films on a GaN/c-sapphire template and showed high density of stacking faults. They observed two stacking faults with different stacking sequences and bounding dislocations in the structure. The origin of the stacking faults was associated with vacancies or interstitial leading to formation or absence of additional (0002) planes. The primary reason being presence of point defects (Zn interstitial), due to the possibility of accommodation of large Zn interstitial in the ZnO lattice, however the presence of oxygen vacancies is equally probable cause of such observation [47]. Narayan et. al. studied the defects at the ZnO/c-sapphire and the hetero-interface AlN/ZnO/c-sapphire. These films were deposited using PLD. The observed density of threading dislocations close to the interface of ZnO/c-sapphire was about $2 \times 10^{10} \text{ cm}^{-2}$, while the density of stacking faults in the basal (0001) plane was about 10^5 cm^{-1} . The hetero-interface between AlN and ZnO was found to be a mixed interface that was polycrystalline in nature. The density of threading dislocations in AlN films oriented towards the (0002) was found to be 10^{10} cm^{-2} . The threading dislocations in ZnO films were oriented with a burgers vector $1/3[11\bar{2}0]$, and the density decreased with increase in film thickness [48]. The decrease in density of threading dislocations is expected due to improvement in the film quality with thickness.

2.4 OPTICAL AND ELECTRICAL PROPERTIES

The operation of all optoelectronic devices is based on creation or annihilation of electron-hole pairs induced by absorption and recombination of photons. The electron-hole pair formation basically involves excitation of an electron from the valence band to

the conduction band leaving a hole behind in the valence band. This excitation occurs from any energetic photon incident on the semiconductor that can impart energy greater than the bandgap of the semiconductor. In this process the energy is absorbed from the energy source and the process is called absorption. The reverse of this process is recombination. When the recombination is radiative, photons are dissipated usually with energy equal to the band gap of the semiconductor. This process is called luminescence. Photoluminescence can be defined as radiative recombination of the electron-hole pairs created by injection of photons [49]. The optical absorption and emission spectra provide information about the bandgap, energy positions of the defects and impurity levels etc. There are other transitions in a material other than the valence to the conduction band transition caused by the presence of defects and impurities. These transitions are free excitons, bound excitons and deep-level transitions. Free excitons are caused by the presence of a free electron and free hole in the conduction band, they experience and coulombic force of attraction due to opposite charges. Thus the electron orbits around the hole as in a hydrogen atom and has a binding energy associated with it. Bound excitons on the other hand, are formed when an isolated intrinsic or extrinsic defect in the lattice facilitates the binding of an exciton via coulombic forces. For example, a free hole can combine with a neutral donor to form a positively charged excitonic ion [49-52]. Deep level transitions are caused by presence of defects in lattice such as vacancies, interstitial or substitutional impurities, or impurity-vacancy complexes in the forbidden energy gap of the semiconductor. These primarily act as carrier recombination or trapping centers and adversely affect the device performance [52].

The direct bandgap energy of ZnO is 3.37eV at room temperature and the refractive index varies from 1.96 to 2.1, with wavelength below the band gap. The conduction band for ZnO is predominantly *s*-type, and valence band is *p*-type (6 fold degenerate). The valence band splits into three bands A, B and C, which are doubly degenerate sub bands. The free exciton binding energies associated with these bands are 63meV, 50meV and 49meV respectively. The experimental bandgap value for wurtzite ZnO is reported to be 3.4eV and that of MgO in rocksalt symmetry is 7.8eV. Therefore, when ZnO is alloyed with Mg the bandgap will increase, but Mg incorporation will also increase the ionicity of the material. Walter et al [53, 54] have applied the LDA approximation to calculate the bowing coefficient value to be 0.56eV. Applying the gap correction of 2.56 eV from LDA approximation to the rocksalt structure, the bandgap of wurtzitic MgO is estimated to be 6.25 eV. Using the estimated value of 6.25 eV for wurtzite MgO and a gap of 3.4 eV for ZnO, they predict a gap of 4.2 eV at 33% MgO, consistent with Ohtomo's result [9]. From the $\text{Mg}_x\text{Zn}_{1-x}\text{O}$ films grown using PLD method, Ohtomo et.al. have experimentally determined the bandgap at room temperature to vary linearly upto 4.15 eV for $x=0.36$. Therefore, $\text{Mg}_x\text{Zn}_{1-x}\text{O}$ films can serve as a suitable material for potential barrier layers in ZnO based devices having a bandgap offset (ΔE_g) as large as 750 meV. The band edge line up at the $\text{ZnO}/\text{Mg}_{0.33}\text{Zn}_{0.67}\text{O}$ is shown in figure 2.6. The value of $\Delta E_c/\Delta E_v$ was determined to be 90/10 using best fit method of the calculated values of effective mass of electrons ($m_e^*=0.28$) and holes ($m_h^*=1.8$) with the experimental data [55]. Figure 2.5 shows the bandgap lineup of ZnO and MgZnO. Optical anisotropy exists in the excitation of these excitons by light polarized either perpendicular or parallel to c-axis of ZnO.

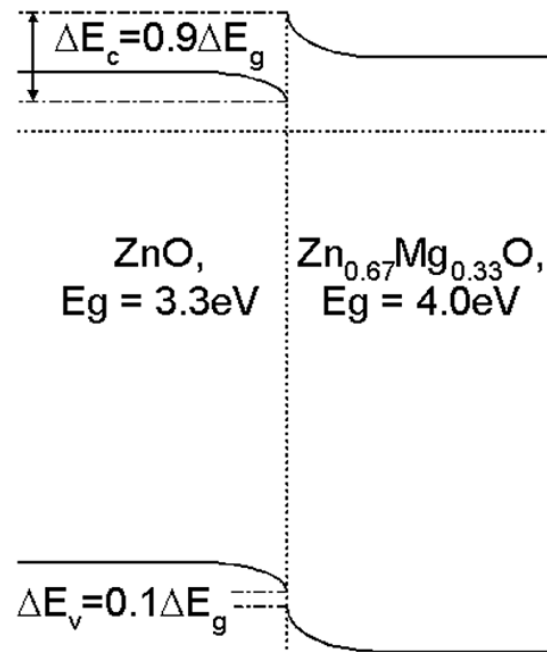


Figure 2.5: shows the bandgap lineup of ZnO and MgZnO.

C-excitons being excited when light is polarized parallel to c-axis and, A and B are excited when light is polarized perpendicular to c-axis of ZnO. Presence of optical anisotropy and high binding energy is useful for many applications of ZnO.

The wide bandgap of ZnO reduces visible light sensitivity, preventing possible degradation of the device [56, 57]. Highly crystalline and optically transparent (visible part of spectrum) ZnO films can be deposited at low temperatures and wet chemical processing of ZnO is possible. These desirable properties have led to increased efforts towards the development of ZnO-based field effect transistors (FETs), thin film transistors (TFTs) and heterostructure field effect transistors (HFETs) [12, 13, 58].

The availability of anisotropic transport properties can be advantageous or detrimental depending on device structure and application. It can be used to optimize the performance of devices such as Schottky contacts or p-n junction diodes, which exhibit a predominantly a one-dimensional current flow by choosing appropriate in-plane crystal orientation. However, more complex electronic devices using the anisotropic mobility and carrier transport would require careful design and analysis. It was observed that although large anisotropy in the bulk mobility is detrimental to 6H-SiC based vertical power devices such as double-implanted metal-oxide-semiconductor field effect transistors (DMOSFETs) [59], in-plane mobility anisotropy can be used to achieve a lower on-resistance in [60]. Orientation-dependent (perpendicular and parallel to (011) rotation-axis) device performance has been investigated for off-axis cut Si MOSFETs, the difference in I-V characteristics has been attributed to mobility and surface roughness anisotropy [61]. Irie et. al. investigated the in-plane mobility anisotropy and strain-direction dependence of inversion layer mobility in Si (100), (110) and (111) and found

an optimum combination of surface orientation, in-plane channel direction and strain direction for enhanced MOSFET device performance [62]. Mobility anisotropy in strained-Si has been used for better FET device performance [63]. Similar studies on orientation-dependence of mobility anisotropy have been studied on organic semiconductors [64, 65]; and in heterostructures and super-lattices where the interface roughness significantly affects anisotropy in transport characteristics [66, 67].

CHAPTER 3: MOCVD GROWTH OPTIMIZATION

It is imperative to control the thin film's material properties to achieve good device performance. Optoelectronic devices such as quantum wells and heterostructures, and electronic devices such as field effect transistors (FETs) etc. strongly depend on the crystal properties, surface and interface morphology, strain, optical and electrical properties. Successful realization of such device structures requires an understanding of the thin film growth phenomena to achieve optimized growth conditions. This chapter focuses on the MOCVD growth optimization of a-plane $\text{Mg}_x\text{Zn}_{1-x}\text{O}$ films on r-sapphire substrate. The first section discusses the MOCVD system configuration used to deposit a-plane $\text{Mg}_x\text{Zn}_{1-x}\text{O}$ films. The following this the focus is on the growth optimization and study of crystal orientation, crystal quality, morphology and optical properties. Finally a preliminary work in development of ZnO-based heterostructures presented.

3.1 MOCVD SYSTEM

The Rutgers MOCVD chamber is an axis-symmetric rotating-disk vertical flow reactor as shown in figure 3.1. It consists of a horizontally placed wafer susceptor, which is rotated at high speeds and is heated by a resistive heater placed below the susceptor. Rotation of the substrate improves the deposition uniformity across the wafer. Gases flow from the top and exit through an exhaust at the bottom. N_2 , introduced into the MOCVD reactor from the top, is used as the carrier gas, while ultra high purity oxygen is used as an oxidizer. This system configuration provides the separation of metalorganics from O_2 , and a small transit time for the gaseous species due to the high speed of gases coming out of the holes in the injectors and the short distance from the injectors to the substrate,

resulting in a reduction of gas phase reactions. To reduce the transit time in the lines an additional Ar push flow is added to the exit side of the bubblers carrying the metalorganics into the reaction chamber. High purity O_2 is introduced into a growth chamber through a separate line. Argon flowing through the bubblers is initially sent through the bypass line directly to the exhaust system and is introduced into the chamber only when the susceptor temperature is heated up to the required temperature. The volume of argon is sufficiently low to prevent any turbulence in the system, as compared to the total volume of gases flowing into the reactor while switching the gas flow from the bypass line into the chamber. A schematic of the flow pattern over a rotating susceptor is shown in figure 3.2. The vertical velocity of gas flowing downward is reduced as it approaches the susceptor and is redirected radially, reaching a stagnation point of zero vertical velocity at the susceptor surface. The flow pattern is characterized by a boundary layer of fluid being dragged around with the disk and thrown outward by centrifugal force. This centrifugal pumping action also sucks gas down toward the disk. When the susceptor is heated, the gas above the susceptor is heated and rises up due to buoyancy, and then falls again after being re-cooled. This instability develops into circulating flow patterns. Circulation can result in undesirably long residence times leading to gas phase reactions that degrade the quality of growing film. These circulating patterns can be avoided by maintaining a large downward flow. In case of ZnO growth, such flow patterns have to be avoided since small particles formed due to gas-phase reactions will stay in the reactor and grow, and will degrade the quality of the growth. These circulating flow patterns can be avoided by maintaining a large downward flow. Hence a large volume of carrier gas has to be constantly introduced from top.

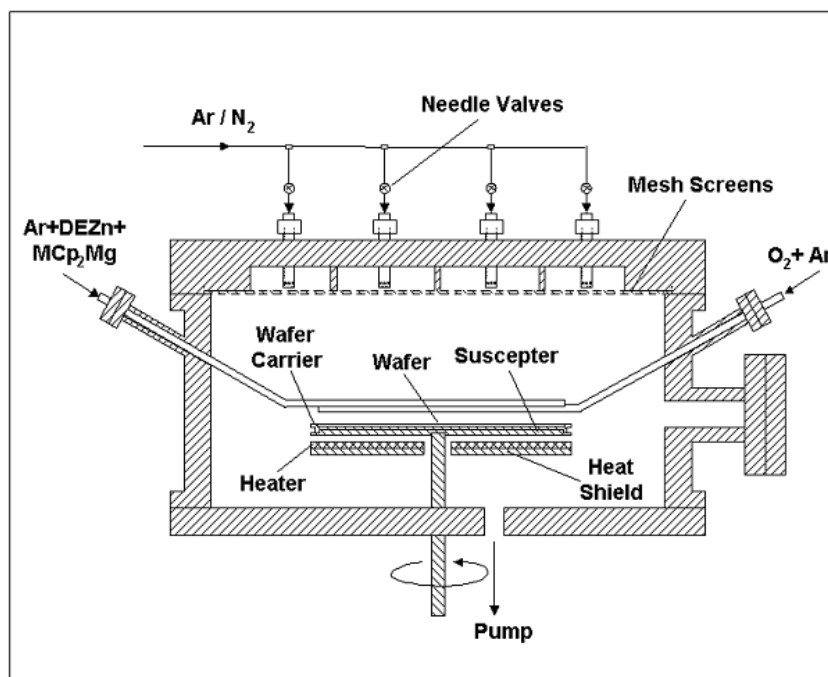


Figure 3.1: Schematic of a MOCVD system for ZnO growth

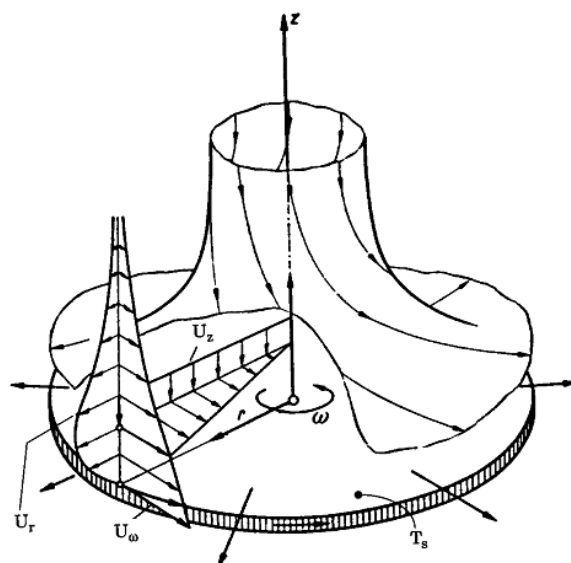


Figure 3.2: Schematic diagram of the axis-symmetric flow patterns in a rotating-disc vertical flow MOCVD reactor

The vacuum system consists of two stages, the first stage is a roots blower that allows a high volume of gas to flow, and the second stage is a roughing pump. The vertical velocity of gas flowing downward is reduced as it approaches the susceptor and is redirected radially, reaching a stagnation point of zero vertical velocity at susceptor surface. An IBM-compatible PC with data acquisition (DAQ) boards is used to control and monitor the mass flow controllers (MFC) and pneumatic valves, and to maintain temperature and pressure in the reactor and the gas lines. The metalorganic precursors used for Zn and Mg are DEZn (Diethyl Zinc) and MCp₂Mg (Bis-methyl cyclopentadienyl Magnesium), respectively. Since, DEZn with melting point -28°C , and the boiling point is 117°C and 30°C at pressures of 760mm Hg and 27mm Hg respectively, has high vapor pressure at room temperature, so the bubbler is maintained at a temperature of $\sim 19^{\circ}\text{C}$. MCp₂Mg on the other hand has a melting point of 29°C and boiling point of 56°C at 0.3mm Hg, thus the bubbler is maintained at $\sim 47^{\circ}\text{C}$. In order to prevent the condensation of precursors vapors in the delivery lines and clogging of the gas handling system, all portions of this network that transport chemical vapor must be heated to or above the evaporation temperature of the precursor. Therefore, the MCp₂Mg line is heated till the inlet into the reactor.

3.2 GROWTH OPTIMIZATION OF a-PLANE $\text{Mg}_x\text{Zn}_{1-x}\text{O}$ FILMS

Heteroepitaxy of ZnO on sapphire involves many problems due to the differences in chemical nature, structure (wurtzite on corundum), lattice parameters, and thermal expansion coefficient. In case of a-plane ZnO growth on r-sapphire, the films also suffer from anisotropic mismatch in lattice parameters and thermal expansion coefficients as

discussed earlier in section 2.3.2. In this section growth optimization of a-plane ZnO and $\text{Mg}_x\text{Zn}_{1-x}\text{O}$ films is discussed. Growth optimizations study includes determination of Mg position in the ZnO lattice, crystal orientation, morphology and crystallinity study and a study of the optical properties.

To optimize oxide film quality, it is desirable that the chemistry of metal oxidation on the surface occurs at a rate much higher than that of film growth. Furthermore, it is desired to have the substrate temperature high enough to promote surface diffusion to achieve good crystallinity. Thus an optimum has to be reached between the growth temperature and the flow of metalorganics reaching the substrate surface for oxidation, to enhance layer-by-layer (Van-der Marwe) growth mode. Therefore neglecting lattice mismatch, layer-by-layer growth of ZnO, can be achieved if Zn atoms are delivered to the r-sapphire substrate along with excess molecular oxygen atoms at a growth rate that is slow compared to the kinetics of the oxygen dissociation reaction $\text{O}_2 \rightarrow 2\text{O}$ and the oxidation reaction $\text{Zn} + \text{O} \rightarrow \text{ZnO}$. In such a case, the rate-limiting step would be the delivery of Zn atoms to the surface. Individual Zn and O atoms could then diffuse on the surface and find their respective sites of minimum energy, which are cation and anion sites in the corundum lattice, respectively, located either at steps or on terraces. If, in contrast, the growth rate is slightly faster than the rate of O_2 dissociation, intermediate products / phases can be formed which get embedded into the growing film thus resulting in poor structural quality. Zn atoms delivered from the Zn precursor using Ar as carrier and O_2 used as oxidizer from a separate injector (as described in earlier section 2.2), with optimized temperature and flow rate is used to deposit a-plane ZnO films.

MgO alloying of ZnO to form a-plane $\text{Mg}_x\text{Zn}_{1-x}\text{O}$ can be achieved by introducing Mg precursor (MCp_2Mg) along with the Zn precursor (DEZn) during the MOCVD growth. It has been reported earlier by Muthukumar et. al. that a $\sim 5\text{nm}$ ZnO buffer was required to sustain the wurtzite crystal structure in a-plane $\text{Mg}_x\text{Zn}_{1-x}\text{O}$ films deposited on the r-sapphire [11]. The presence of ZnO buffer provides epitaxial wurtzite template for subsequent $\text{Mg}_x\text{Zn}_{1-x}\text{O}$ films to be wurtzite. This is primarily because Mg atom prefers octahedral sites on sapphire as substrate, thus allowing formation of cubic rocksalt $(\text{Mg,Zn})\text{O}$. A ZnO buffer on the other hand prevents the interaction of Mg atom and the sapphire substrate, thus restricting the formation of the cubic rocksalt structure.

Growth rate of the film is dependent on the substrate temperature and the gas-flow conditions. Gas flow and deposition temperature determines the rate-limiting step during a CVD growth. At low deposition temperatures, keeping the gas-flow constant, the growth rate increases exponentially with increase in temperature. Assuming that the gas-phase reaction is limited by controlling and diluting the gasses in the reaction chamber, and most of the reaction occurs on the surface of the substrate. The rate-limiting step in such a process is the reaction rate and the surface diffusion of the constituents' Zn atom and oxygen. At high temperatures however, the surface diffusion energy is much higher than the activation energy of the surface chemical reaction, the rate-limiting step is the transfer of the reactants onto the surface of the substrate across the boundary layer. In this regime if the gas-flow is increased it further increases the growth rate. Growth rate is significantly affected by $\text{Mg}_x\text{Zn}_{1-x}\text{O}$ alloy composition. Since, Mg metalorganic has much lower vapor pressure as compared to Zn metalorganic, and the surface diffusion of Mg

slower than Zn, the overall growth rate of a $\text{Mg}_x\text{Zn}_{1-x}\text{O}$ film is reduced with Mg composition in the films.

ZnO and $\text{Mg}_x\text{Zn}_{1-x}\text{O}$ films were deposited on r-sapphire substrates using MOCVD deposition technique. The deposition temperature and gas flow conditions are optimized for improved film structural and optical properties. The films were deposited in the temperature range of 400 – 580°C. The film's thickness was maintained at ~520nm for comparison. Variations in Mg composition are achieved by changing the Zn/Mg metalorganic gas-flow ratio. Typical growth rate of the films ranged from 450 – 500nm/hr.

3.2.1 Mg IN ZnO LATTICE

Thermodynamic solid solubility of MgO in ZnO is predicted to be ~5% [68]. Even though higher compositions of wurtzite $\text{Mg}_x\text{Zn}_{1-x}\text{O}$ have been demonstrated [9-11, 23], the precise position of Mg atom in ZnO lattice is uncertain. Mg atom could be substitutional to the Zn atom or stay as interstitial. For precise composition and film quality control it is required to know the position of Mg in the ZnO lattice. In collaboration with Prof. Ulrike Diebold's group at the Physics department at Tulane University, we studied this in detail. Figure 3.3 (a) shows a schematic of the Zn plane in the wurtzite lattice of ZnO. Figure 3.3 shows the Auger scattering intensity observed (b) from Zn and Mg atoms and (c) from O atoms with variation in the polar angle.

Auger electron spectroscopy (AES) with different polar angles is performed to investigate the position of Mg in ZnO lattice.

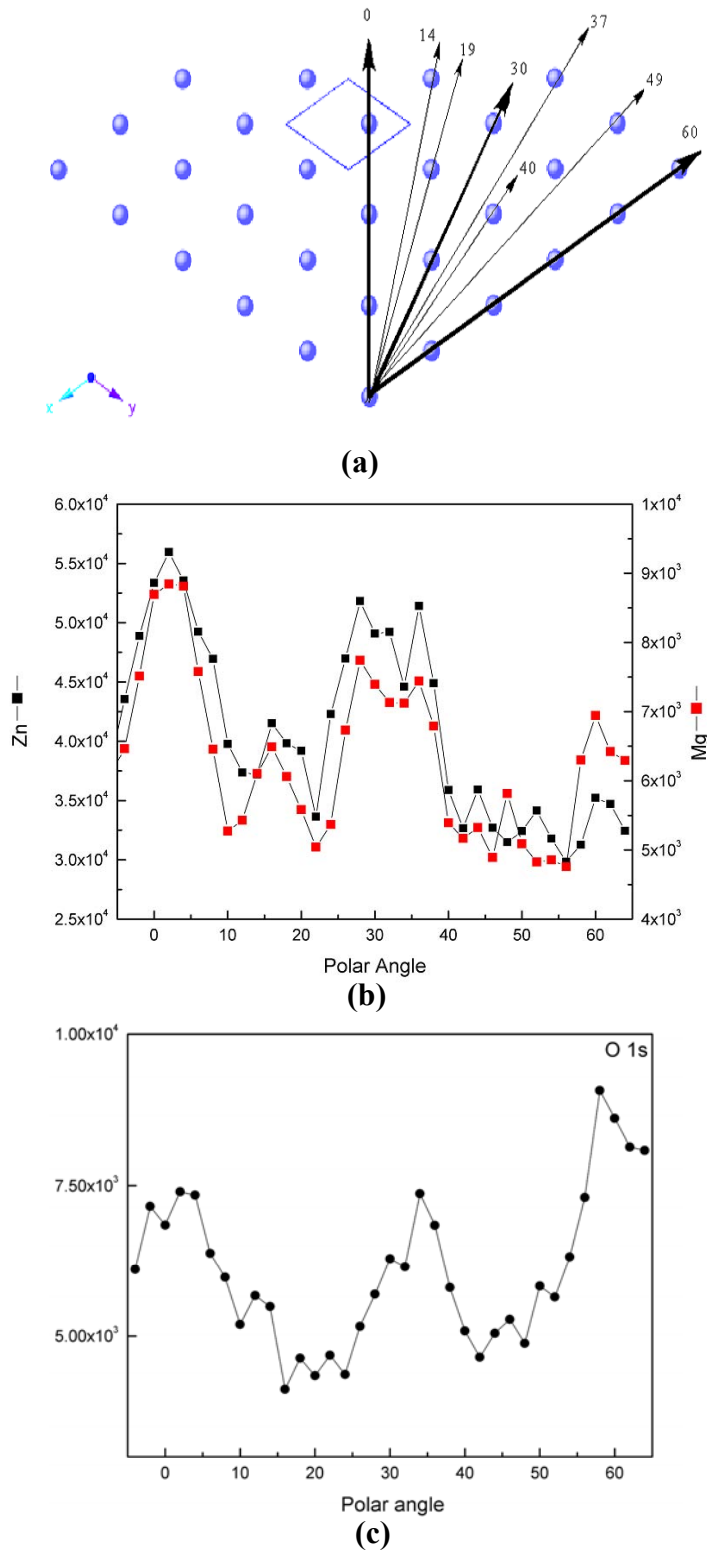


Figure 3.3 (a) shows a schematic of the Zn plane in the wurtzite lattice of ZnO, (b) and shows the Auger scattering intensity observed from Zn and Mg atoms and O atoms, respectively with variation in the polar angle.

Auger electron spectroscopy (AES) is one of the most widely used techniques for characterization of materials and their surface structure. In angle-resolved AES the signal intensity varies with angle of detection with respect to surface and is sensitive to the surface structure. So, varying the angle of incidence and collection angle can be used to identify the single crystalline surface of $\text{Mg}_x\text{Zn}_{1-x}\text{O}$ film.

It can be observed that the largest scattering is possible at polar angles of 0, 30 and 60 degrees respectively, due to larger number of atoms along these angles. The oxygen plane under the Zn plane has a similar array of atoms. It can be clearly observed that the highest intensity peaks are at 0, 30 and 60 degrees. Furthermore, the peak intensities for Zn and Mg have almost a one to one correspondence with polar angle variation. This indicates that the Zn and Mg atoms are present at similar locations in the ZnO lattice.

3.2.2 Mg composition:

One of the key issues in growth optimization of a-plane $\text{Mg}_x\text{Zn}_{1-x}\text{O}$ film is control of Mg composition. Mg composition is controlled during the MOCVD growth by controlling the Mg/Zn metalorganic gas-flow ratio. Mg composition is also affected by the deposition temperature during MOCVD growth. Muthukumar et. al. indicated that an increase in the deposition temperature reduces the Mg composition in a-plane $\text{Mg}_x\text{Zn}_{1-x}\text{O}$ films as discussed in section 2.2 [11].

The room temperature transmission spectra were measured with UV-visible spectrometer. Figure 3.4 shows a plot of % transmission versus wavelength (nm) for $\text{Mg}_x\text{Zn}_{1-x}\text{O}$ films with $x = 0, 0.18, 0.25, 0.34, 0.60$, respectively.

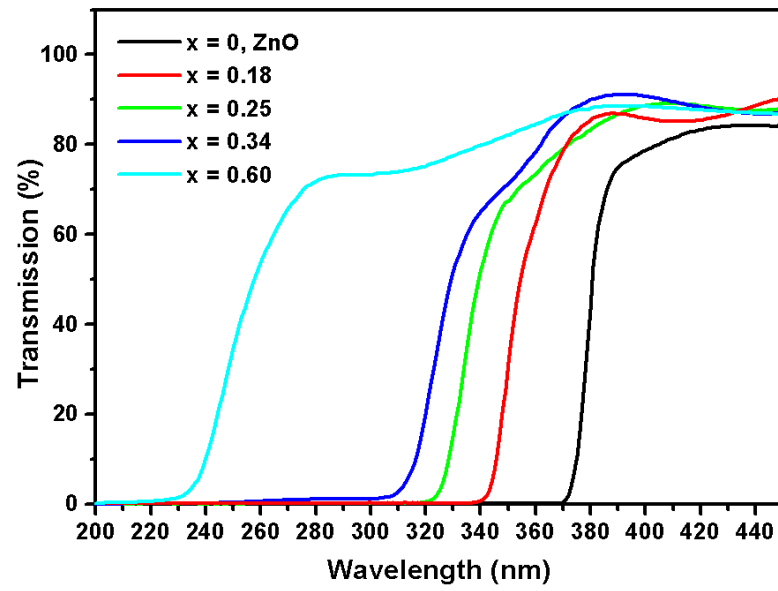


Figure 3.4 shows a plot of % transmission versus wavelength (nm) for $\text{Mg}_x\text{Zn}_{1-x}\text{O}$ films with $x = 0, 0.18, 0.25, 0.34, 0.60$, respectively.

The absorption coefficient α is calculated after excluding the substrate reflection loss. A simplified energy band edge model is adopted to determine the energy bandgap (E_g) of $Mg_xZn_{1-x}O$ for various Mg compositions as given by:

$$\alpha^2 \propto (h\nu - E_g)$$

The sharp transmission edge in figure 3.4 also confirms the good optical property of the $Mg_xZn_{1-x}O$ films. With the increase of the Mg composition, the changes in slopes of the transmission edges also show alloy-broadening effect. It is evident that an increase in the Mg composition moves the transmission edge towards lower wavelengths corresponding to increase in the direct bandgap of the $Mg_xZn_{1-x}O$ films. The increase in direct bandgap with Mg composition in $Mg_xZn_{1-x}O$, follows [9, 13, 33]:

$$E_g(Mg_xZn_{1-x}O) = [x \times 5.8 + (1 - x) \times 3.32] eV \quad (3.1)$$

And,

$$\Delta E_c / \Delta E_v = 70 / 30 \quad (3.2)$$

3.2.3 MORPHOLOGY, ORIENTATION AND CRYSTAL PROPERTIES

The morphology of the a-plane films was studied using a Leo Ziess field emission scanning electron microscopy (FESEM). The crystal orientation was studied using a Bruker D-8 x-ray diffraction system, while the crystallinity was studied using a x-ray synchrotron radiation source at Brookhaven National Labs.

Figure 3.5 (a) and (b), shows the FESEM images of a ZnO and $Mg_{0.12}Zn_{0.88}O$ film on r-sapphire, respectively. The films are dense and uniform over the entire substrate surface. X-ray θ -2 θ scans are used to determine the crystal orientation of the films. Figure 3.6, (a) and (b) show x-ray coupled scans for the ZnO and $Mg_{0.12}Zn_{0.88}O$ films,

respectively. It is observed that only $(11\bar{2}0)$ reflections are present indicating the films are purely a-plane oriented ZnO and $\text{Mg}_x\text{Zn}_{1-x}\text{O}$. It is also observed that the peak separation between the $(02\bar{2}4)$ r-sapphire peak and the $(11\bar{2}0)$ $\text{Mg}_x\text{Zn}_{1-x}\text{O}$ peak is lower than the corresponding $(11\bar{2}0)$ ZnO peak. This is because of change in the lattice parameters with MgO alloying of ZnO, as discussed in section 2.1. The epitaxial relationship between a-plane ZnO, $\text{Mg}_x\text{Zn}_{1-x}\text{O}$ films and r-sapphire substrates using X-ray diffraction was earlier identified to be $(11\bar{2}0)$ ZnO, $\text{Mg}_x\text{Zn}_{1-x}\text{O} \parallel (01\bar{1}2)$ Al_2O_3 and $[0001]$ ZnO, $\text{Mg}_x\text{Zn}_{1-x}\text{O} \parallel (0\bar{1}11)$ Al_2O_3 [33].

Crystal properties of the a-plane ZnO films are characterized with variations in MOCVD deposition temperature. Figure 3.7 shows a plot of full width at half maximum (FWHM) of ω -rocking curves and detector scan of a-plane ZnO films with variations in deposition temperature. The film thickness for all samples is maintained to be about $\sim 520\text{nm}$ for all the samples. It is observed that an increase in the deposition temperature from 400°C to 580°C decreases the FWHM of the detector scan, while increasing the FWHM of the ω -rocking curves. FWHM of the ω -rocking curves is indicative of the thin film mosaic, while the FWHM of the detector scan is indicative of thin film crystallinity and strain. Assuming a layer-by-layer (Van-der Marwe) growth mode, an increase in deposition temperature improves the crystallinity of the thin films by increasing the surface diffusion during the initial nucleation and growth. However, such an increase in deposition temperature also increases the mosaic in the films as result of the in-plane lattice mismatch with the r-sapphire substrate. Growth rate of the films also plays a key role in determining the crystallinity and mosaic in the films.

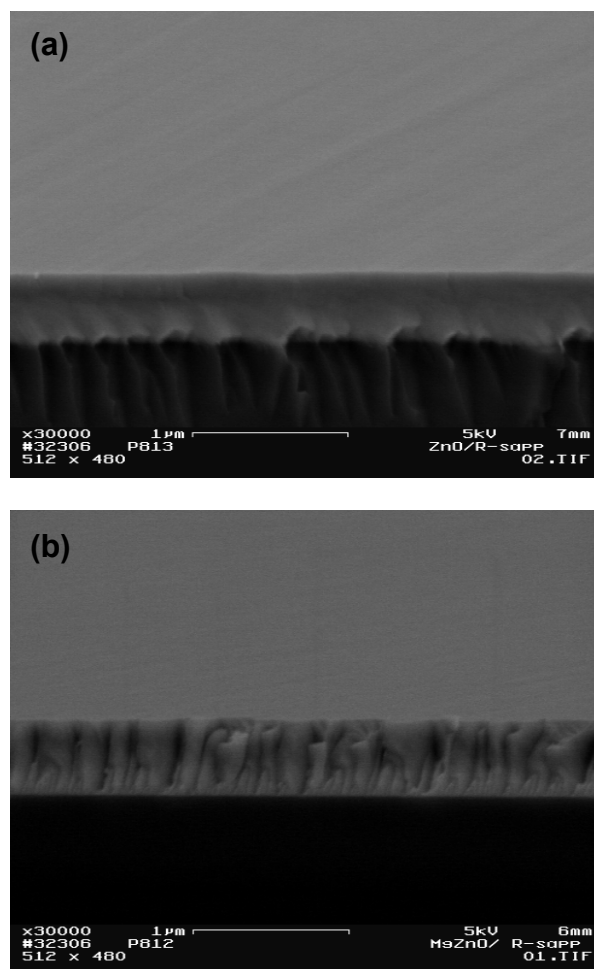


Figure 3.5: (a) and (b) shows the FESEM images of a ZnO and $\text{Mg}_{0.12}\text{Zn}_{0.88}\text{O}$ film on r-sapphire, respectively.

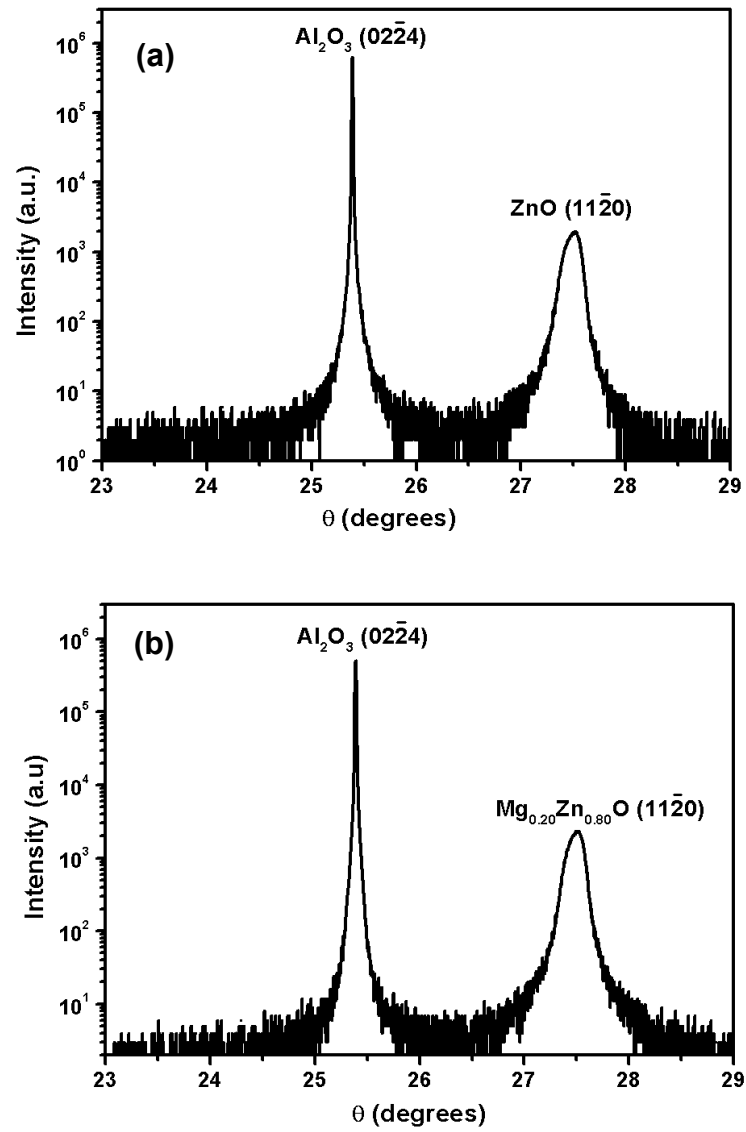


Figure 3.6: (a) and (b) show x-ray coupled scans for a-plane ZnO and $\text{Mg}_{0.12}\text{Zn}_{0.88}\text{O}$ on r-sapphire, respectively.

An increase in the growth rate due to gas-flow increase or deposition temperature increase would have different affect on the crystal properties. Increase in the metalorganic gas-flow while maintaining the same deposition temperature increases the growth rate, however leads to poorer crystal properties. This is again justified by the surface diffusion rate, as the reaction constituents reaching the substrate surface do not have enough surface diffusion time, leading to poorer film crystallinity. Another case is if, the growth rate is slightly faster than the rate of O_2 dissociation, intermediate products/ phases can be formed which get embedded into the growing film resulting in poor film structural quality. The a-plane ZnO films deposited at lower deposition temperatures than 400°C showed extremely poor crystal properties. Films deposited at 300°C did not show any peaks in XRD indicating amorphous structure, while the films deposited at 360°C showed FWHM of ω -rocking curves as 2.6142° and FWHM of the detector scan as 0.279° . Thus the optimized deposition temperature for good crystallinity as well as mosaic is in the range 520°C - 560°C , where the FWHM of the ω -rocking curves is about 0.4° - 0.5° and the FWHM of the detector scan is 0.037° - 0.039° .

3.2.4 OPTICAL PROPERTIES

The optical properties of the a-plane films were characterized using room temperature PL spectra. The PL measurements were done using a 325nm He-Cd laser. All the samples were grown at $\sim 520^\circ\text{C}$, with a film thickness of $\sim 520\text{nm}$ for comparison. Figure 3.8 shows the room temperature PL spectra for a-plane $\text{Mg}_x\text{Zn}_{1-x}\text{O}$ ($x = 0, 0.08$ and 0.12) films on r-sapphire substrate. The intensities of the peaks were normalized for comparison between different film compositions.

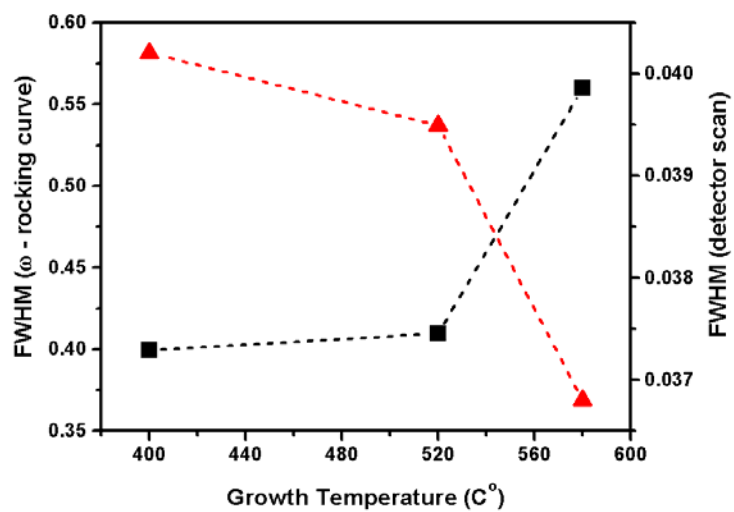


Figure 3.7 shows a plot of full width at half maximum (FWHM) of ω -rocking curves and detector scans of a-plane ZnO films with variations in deposition temperature.

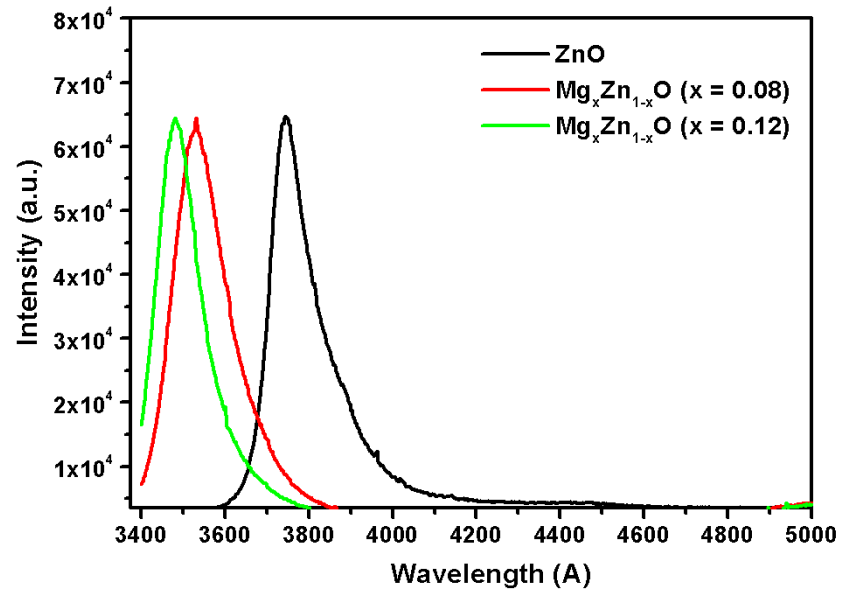


Figure 3.8 shows the room temperature PL spectra for a-plane $\text{Mg}_x\text{Zn}_{1-x}\text{O}$ ($x = 0$, 0.08 and 0.12) films on r-sapphire substrate, the intensities of the peaks were normalized for comparison between different film compositions.

A blue shift with increase in Mg composition is clearly observed with an increase in Mg composition in the films. This is consistent with an increase in the direct bandgap of $\text{Mg}_x\text{Zn}_{1-x}\text{O}$ films with Mg composition increase as indicated in equation 3.1. The absence of deep level peaks in the PL spectra indicates that the films have good optical properties. The FWHM of the films increase from $\sim 95\text{meV}$ for a-plane ZnO to $\sim 133\text{meV}$ observed for a-plane $\text{Mg}_{0.12}\text{Zn}_{0.88}\text{O}$ films. The peak intensities for all the samples are of the order of 10^4 counts.

The low FWHM and high intensity is also indicative of good structural properties of the films. Large dislocation density in the films lead to non-radiative recombination centers, thus lowering the intensity and increasing the FWHM of the PL peaks. Absence of deep level peaks is indicative of purity of the samples.

3.3 ZnO/ $\text{Mg}_x\text{Zn}_{1-x}\text{O}$ HETEROSTRUCTURE

With the advances in the epitaxial technology of ZnO and $\text{Mg}_x\text{Zn}_{1-x}\text{O}$, heterostructures and quantum well (QW) structures are of considerable practical interest. Due to the quantum confinement effect, quantum well structures may provide larger oscillation strength, enhanced exciton binding energy, and tunability of the operating wavelength. By reducing the dimensions of the active layer, the exciton binding energy and the oscillator strength can be greatly enhanced, which should further improve the lasing characteristics. This effect has been extensively studied in III–V narrow semiconductor QWs [69]. However, very few experimental results about the quantum size effect have been reported for II–VI wide band-gap semiconductor QWs [70, 71]. This is because the exciton radius of a wide band-gap semiconductor is relatively small so that the quantum size effect is pronounced only as its size in the confinement direction

becomes very small. Recently, Koinuma et. al. [72-78] have conducted extensive studies in ZnO/MgZnO based multiple quantum wells (MQW) grown on lattice matched ScAlMgO₄ (SCAM) substrates with (0001) orientation. They report improved structural and optical properties of ZnO MQWs by the adoption of lattice-matched SCAM substrates [78]. The lattice matching condition enabled them to achieve high controllability of layer thickness resulting in the quantum-confinement effect for the exciton energy for a well width in the order of 1.5 unit cells or more and a bright excitonic PL at room temperature [77]. They have also characterized the exciton binding energies due to the quantum confinement effect [72] with varying well widths and barrier heights and the effect of temperature on the excitonic properties [79] on these ZnO based MQWs. The binding energies of excitons in ZnO based MQWs were found to be much higher than those of bulk ZnO and were dependent on the well width. Their experimental results matched with the theoretical calculations [80] that took into account exciton–phonon interaction of these structures. They have also reported that the coupling strength between the exciton and LO phonon [73] in ZnO/MgZnO MQWs was largely reduced compared within bulk ZnO and this remarkable reduction was closely correlated with enhancement of the exciton binding energy, indicating that the stability of excitons was greatly increased by the enhancement of exciton binding energy in quantum wells. In other cases Mg_xZn_{1-x}O films have been used as capping layer to enhance optical properties of ZnO epitaxial layers [81]. The capped films were epitaxially grown on lattice-matched ScAlMgO₄ substrates by laser molecular-beam epitaxy. A photoluminescence spectrum taken from the ZnO layer at 5K showed emission bands at 3.389, 3.376, and 3.362 eV. The two higher bands were due to *A*- and *B*- free exciton

emissions and the lowest band was due to emission of a neutral-acceptor bound exciton (I_6). The linewidth of the I_6 emission in the uncapped sample (0.8 meV) was significantly smaller than that in the capped one (6 meV) which was explained as a result of the strain applied across the ZnO layer because of the difference in lattice constant between the two layers. Thus it is interesting to study ZnO/ $\text{Mg}_x\text{Zn}_{1-x}\text{O}$ films based heterostructures.

A key issue to successful growth the ZnO- $\text{Mg}_x\text{Zn}_{1-x}\text{O}$ based heterostructure by MOCVD is use of appropriate substrate temperature to facilitate surface diffusion of the reacting species and proper control of the gas flow during the growth to obtain required MgO-ZnO alloy composition. Achieving a sharp interface between the layers is required. Abruptness of the hetero-interface depends on various parameters including surface roughness of the initial layer, strain-relaxation at the initial-layer/substrate interface and at the hetero-interface. We have also observed that the optimum growth temperature to achieve good material properties between binary ZnO and its ternary $\text{Mg}_x\text{Zn}_{1-x}\text{O}$ is very different. Thus the difference in growth rates and optimum growth temperatures between layers has to be accounted for and optimized based on the alloy compositions for development of such heterostructures, quantum wells or super lattice structures.

We have grown ZnO-based heterostructures using $\text{Mg}_x\text{Zn}_{1-x}\text{O}$ as barrier layers by MOCVD. Figure 3.9, shows the FESEM image of a ZnO- $\text{Mg}_x\text{Zn}_{1-x}\text{O}$ single heterostructure. The small difference in valence electrons between ZnO and $\text{Mg}_x\text{Zn}_{1-x}\text{O}$ ($x = 0.15$) leads to low z-contrast observed between the two layers.



Figure 3.9: shows the FESEM image of a $\text{ZnO-Mg}_x\text{Zn}_{1-x}\text{O}$ single heterostructure.

Summary:

In summary, this chapter discusses the MOCVD growth optimization of a-plane ZnO and $\text{Mg}_x\text{Zn}_{1-x}\text{O}$ thin films. The position of Mg in the ZnO lattice was determined. The films' morphology, orientation and crystal properties were studied and analyzed in detail for optimum growth conditions. We also discussed the optical properties of the a-plane $\text{Mg}_x\text{Zn}_{1-x}\text{O}$ films, it was observed that the films have very good optical properties as indicated by room temperature PL spectra. In the final section an introduction and preliminary work in development of ZnO/ $\text{Mg}_x\text{Zn}_{1-x}\text{O}$ based heterostructures was discussed. The understanding of the MOCVD growth process and the optimization of the thin film properties paved way for the subsequent chapters in this work.

CHAPTER 4: IN-PLANE STRAIN ANISOTROPY IN a-PLANE $\text{Mg}_x\text{Zn}_{1-x}\text{O}$

Non-polar a-plane ZnO films grown on r-sapphire substrate has epitaxial relationship with the substrate. The anisotropic in-plane lattice mismatch between ZnO and r-sapphire lead to anisotropic in-plane strain components in the grown a-plane films. Figure 4.1 (a) and (b) show schematic and lattice structure of a-plane ZnO film on r-sapphire substrate, respectively. This chapter deals with the x-ray diffraction (XRD) measurement of the a-plane ZnO and $\text{Mg}_x\text{Zn}_{1-x}\text{O}$ films grown on r-sapphire substrate for the accurate determination of the in-plane and out-of-plane strain in these thin films. It is divided into three different sections: the first section analyzes strain and lattice parameter change in a-plane ZnO films grown under similar conditions of MOCVD growth, with variations in film thickness. The subsequent section analyzes strain and lattice parameter variation in a-plane $\text{Mg}_x\text{Zn}_{1-x}\text{O}$ films with variation in Mg composition. Finally, the last section of the chapter deals with reciprocal space maps of a-plane ZnO and $\text{Mg}_x\text{Zn}_{1-x}\text{O}$ films for qualitative analysis of the weak and strong defects such as vacancies, interstitials and dislocation loops. The significance of this study lies in the design and development of a-plane ZnO based quantum wells and heterostructures, where a lattice distortion will lead to spontaneous and piezoelectric polarization fields thus reducing the quantum efficiency. This study holds significance for design and development of electronic devices as well, where a strain state in the films could enhance the electron mobility [82]. Apart from device properties, strain in the films also directly affects physical properties of the semiconductor thin films [83].

The out-of-plane strain can be easily determined from the high-resolution symmetric ω - 2θ scan. However, detailed characterization of in-plane strain components

in non-polar a-plane ZnO films is a challenge, while using conventional high resolution x-ray systems in symmetric mode, primarily due to the absence of corresponding substrate peaks and difficulties in accessing multiple reciprocal space points in the Ewald's sphere. Furthermore, high order reflections have low intensity counts reducing the precision in the measurement. Thus in order to comprehensively characterize the in-plane strain components of the ZnO and $\text{Mg}_x\text{Zn}_{1-x}\text{O}$ films, we used x-ray synchrotron radiation source with a four-circle high-resolution diffraction setup at Brookhaven National Labs at beam-line X6B, with energy range 6.5 – 20keV. This system was equipped with a Si (111) mono-crystal channel-cut located 10m from source used as grating, with resolution (dE/E) of 2.0×10^{-4} @ 8keV. The spot size (mm) of the source is $0.3H \times 0.3V$ in focused state with an angular acceptance (mradians) of 3.0. Use of a synchrotron radiation overcomes the above mentioned problems. It also provides monochromatic source with high-resolution beam optics and high intensity counts for high-order reflections ensures precision in measurement. The use of a four-circle setup helps to access most of the high-order reflections in symmetric mode. An orientation matrix of the films is setup by accessing precise position of various x-ray reflections. Lattice refinement is performed using these reflections to give precise unit cell (a , b , c , α , β and γ). The measured lattice parameters are then evaluated against bulk ZnO lattice parameters to calculate strain, according to equation 4.1:

$$\text{Strain}(\%) = \frac{p[hkil] - p_o[hkil]}{p_o[hkil]} \times 100\% \quad (4.1)$$

Where, $p[hkil]$ and $p_o[hkil]$, correspond to the strained and relaxed lattice parameters along an arbitrary crystal direction $[hkil]$.

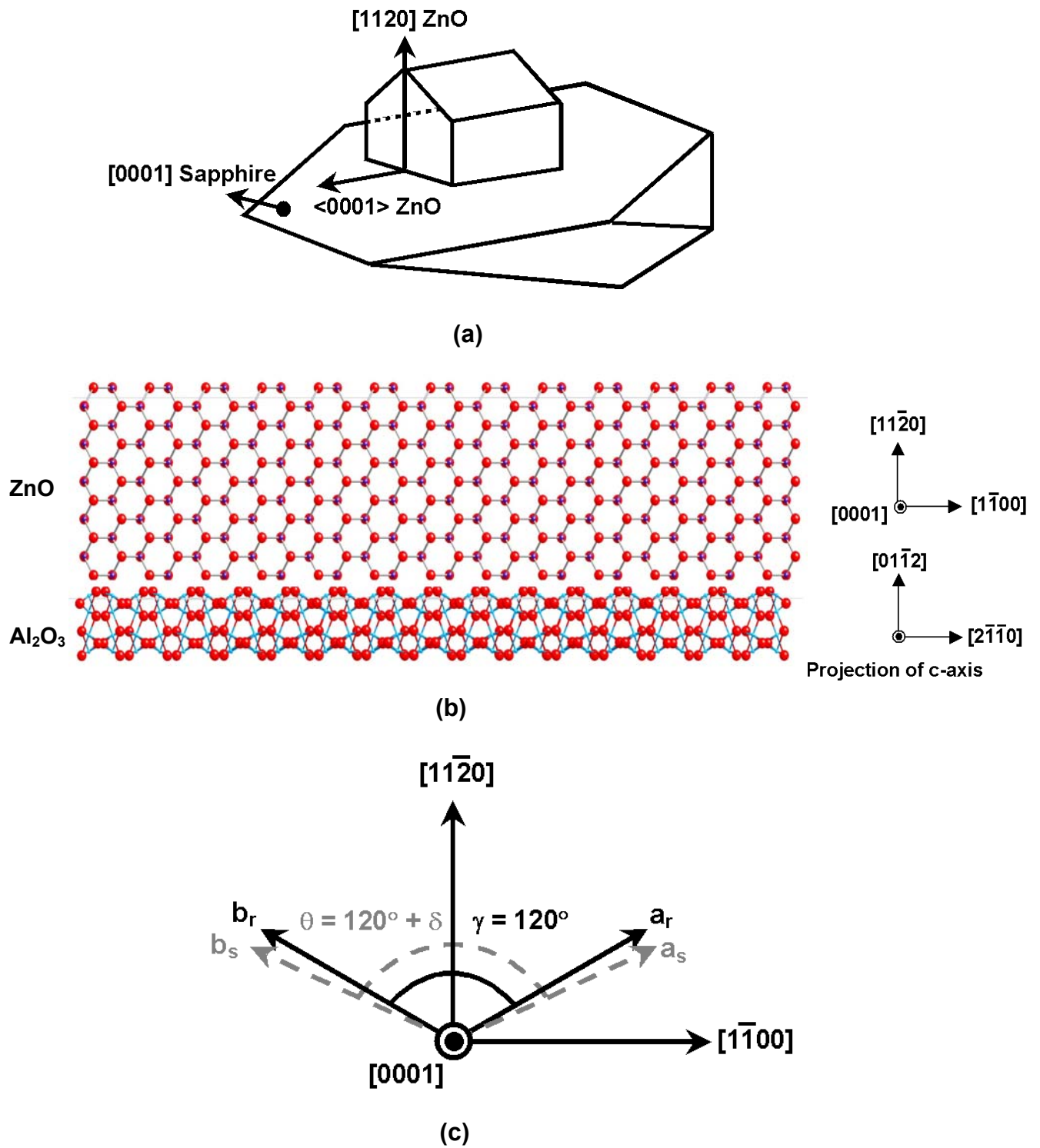


Figure 4.1: (a) and (b) show schematic and lattice structure of a-plane ZnO film on r-sapphire substrate, respectively. (c) Shows orthogonal axes for a hexagonal unit cell

A hexagonal unit cell ($a = b \neq c$, $\alpha = \beta = 90^\circ$ and $\gamma = 120^\circ$) distortion can be defined by a orthorhombic unit cell ($a \neq b \neq c$, $\alpha = \beta = \gamma = 90^\circ$) [84]. A hexagonal unit cell always has a pair of orthogonal axes, as discussed earlier in section 2.3 as shown in figure 4.1 (c). In case of a-plane films such orthogonal axes can be described using $a[11\bar{2}0]$ as out-of-plane axes, and $p[\bar{1}100]$ and $c[0001]$ as in-plane axes. The unit cell transformation from hexagonal to orthorhombic unit cell is given by:

$$\begin{pmatrix} h \\ k \\ l \end{pmatrix}_O = \begin{pmatrix} h \\ k \\ l \end{pmatrix}_H \begin{pmatrix} 1/2 & -1/2 & 0 \\ 1/2 & 1/2 & 0 \\ 0 & 0 & 1 \end{pmatrix} \quad (4.2)$$

The corresponding orthorhombic unit cell would have parameters given by [84]:

$$\begin{aligned} \vec{a}_O &= \vec{a}_H + \vec{b}_H \\ \vec{b}_O &= -\vec{a}_H + \vec{b}_H \\ \vec{c}_O &= \vec{c}_H \end{aligned} \quad (4.3)$$

Where, **a**, **b** and **c** are vector lattice parameters. Subscript (O) correspond to orthorhombic unit cell, while subscript (H) corresponds to hexagonal unit cell.

To evaluate the in-plane and out-of-plane strain in the a-plane films, the difference in the lattice parameters of a relaxed ZnO and a strained a-plane film is taken along the orthogonal axes system set in figure 4.1 (c). Where, a_r and b_r correspond to the relaxed lattice parameters and a_s and b_s correspond to the strained lattice parameters. Since, in a hexagonal system $a = b$, an average of the unit cell parameters a and b , measured from the unit cell refinement is taken. Also, the deviation in angle γ (defined as $\Delta\gamma$) affects a and b lattice parameters, but is assumed to have insignificant effect on c lattice parameter to the zeroth order. This assumption is valid since c-axis is orthogonal to both a-axis and b-axis as seen in figure 4.1 (c).

4.1. Strain with a-plane ZnO film thickness

Non-polar a-plane ZnO thin films were deposited on r-sapphire substrates. The growth temperature ($\sim 520^\circ\text{C}$) and the gas-flow conditions were maintained constant for all the samples during MOCVD growth, with a typical growth rate of $\sim 500\text{nm/hr}$. The deposition time of the samples was varied to achieve the difference in the film thickness. A step on the samples was created by wet etching of the samples to the sapphire substrate, using a photolithography mask. An alpha-stepper was used across the step to measure the thickness of the films. XRD measurements were carried out on the samples using a synchrotron radiation source at Brookhaven National Labs followed by lattice refinement to obtain the unit cell parameters. The lattice parameters $a[11\bar{2}0]$, $p[1\bar{1}00]$ and $c[0001]$ are then calculated along the orthogonal axes using the measured a and b lattice parameters, shown in table 4.1. The error factor for the lattice refinement was of the order of 10^{-4}nm . The error in film thickness measurement using an alpha stepper is typically less than 1%.

Table 4.1: Lattice parameters along orthogonal parameters $a[11\bar{2}0]$, $p[1\bar{1}00]$ and $c[0001]$ axis, with variation in a-plane ZnO film thickness.

<i>Film Thickness</i> (nm)	$a \pm \Delta a$ (\AA) $[11\bar{2}0]$	$p \pm \Delta p$ (\AA) $[1\bar{1}00]$	$c \pm \Delta c$ (\AA) $[0001]$	$\gamma \pm \Delta\gamma$ (degrees)
355	3.2595 ± 0.0007	5.65364 ± 0.0012	5.1726 ± 0.0001	120.31 ± 0.012
406	3.2576 ± 0.000228	5.65032 ± 0.00039	5.17286 ± 0.000151	120.282 ± 0.006
520	3.25396 ± 0.000517	5.64313 ± 0.00089	5.18115 ± 0.000344	120.250 ± 0.0126
1000	3.25001 ± 0.00021	5.63221 ± 0.00036	5.201 ± 0.00013	120.107 ± 0.007
2000	3.2498 ± 0.00035	5.6288 ± 0.0006	5.2065 ± 0.00023	120 ± 0.005

It is observed that γ for the films with thickness $< 2000\text{nm}$ is larger than 120° , while maintaining $\alpha = \beta = 90^\circ$, as shown schematically in figure 4.1 (c). Figure 4.2 (a), (b) and (c) show plots of lattice parameters $a[11\bar{2}0]$, $p[\bar{1}\bar{1}00]$ and $c[0001]$ on orthogonal axes with respect to the a-plane ZnO film thickness. It is observed that the $a[11\bar{2}0]$ and $p[\bar{1}\bar{1}00]$ lattice parameters decrease, while the $c[0001]$ lattice parameter increases with an increase in the film thickness. The lattice parameters relax to the bulk ZnO value for films with thickness $\geq 2000\text{nm}$.

Using the measured lattice parameters and bulk ZnO lattice parameters, strain is calculated according to equation 4.1, as shown in the plot of figure 4.3 (a). Figure 4.3 (b) shows a plot of the c/a ratio and (c) shows the plot of the strain anisotropy $|\epsilon_{\parallel}/\epsilon_{\perp}|$ with a-plane ZnO film thickness. The out-of-plane strain (ϵ_{zz}) along $a[11\bar{2}0]$ is non-zero for films with thickness $< 2000\text{nm}$, and decreases with increase in film thickness. The in-plane strains (ϵ_{yy}) along $p[\bar{1}\bar{1}00]$ and (ϵ_{xx}) along $c[0001]$ is observed to be anisotropic, with (ϵ_{yy}) decreasing and (ϵ_{xx}) increasing, with increase in film thickness. The negative value of (ϵ_{xx}) corresponds to a compressive stress along the in-plane c-axis and positive value of (ϵ_{yy}) is indicative of a tensile stress for film thickness $< 2000\text{nm}$, with out-of-plane stress to be zero as it is the direction of unrestrained growth. A sapphire crystal in a hexagonal crystal system with lattice parameters $a = 0.47592\text{nm}$ and $c = 1.2996\text{nm}$, gives a $(c/2a)$ ratio of ~ 1.3654 [85]. Since, the a-plane ZnO films are epitaxially grown on r-sapphire, the (c/a) ratio of strained ZnO films is closer to the sapphire value and increase from ~ 1.5874 to ~ 1.60212 with relaxation. It is also observed that the strain anisotropy $|\epsilon_{\parallel}/\epsilon_{\perp}|$ increases with increase in film thickness.

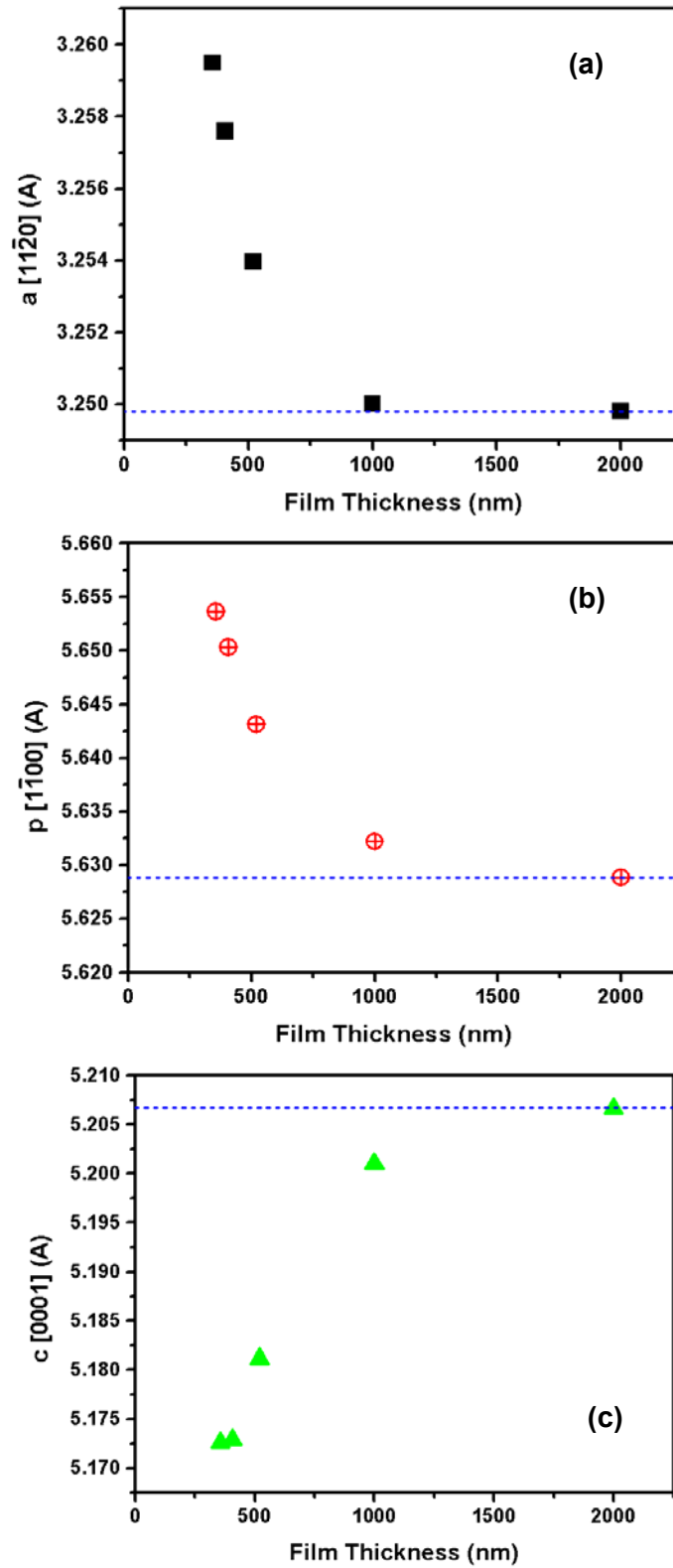


Figure 4.2: (a), (b) and (c) show plots of lattice parameters $a[11\bar{2}0]$, $p[1\bar{1}00]$ and $c[0001]$ on orthogonal axes with respect to the a-plane ZnO film thickness

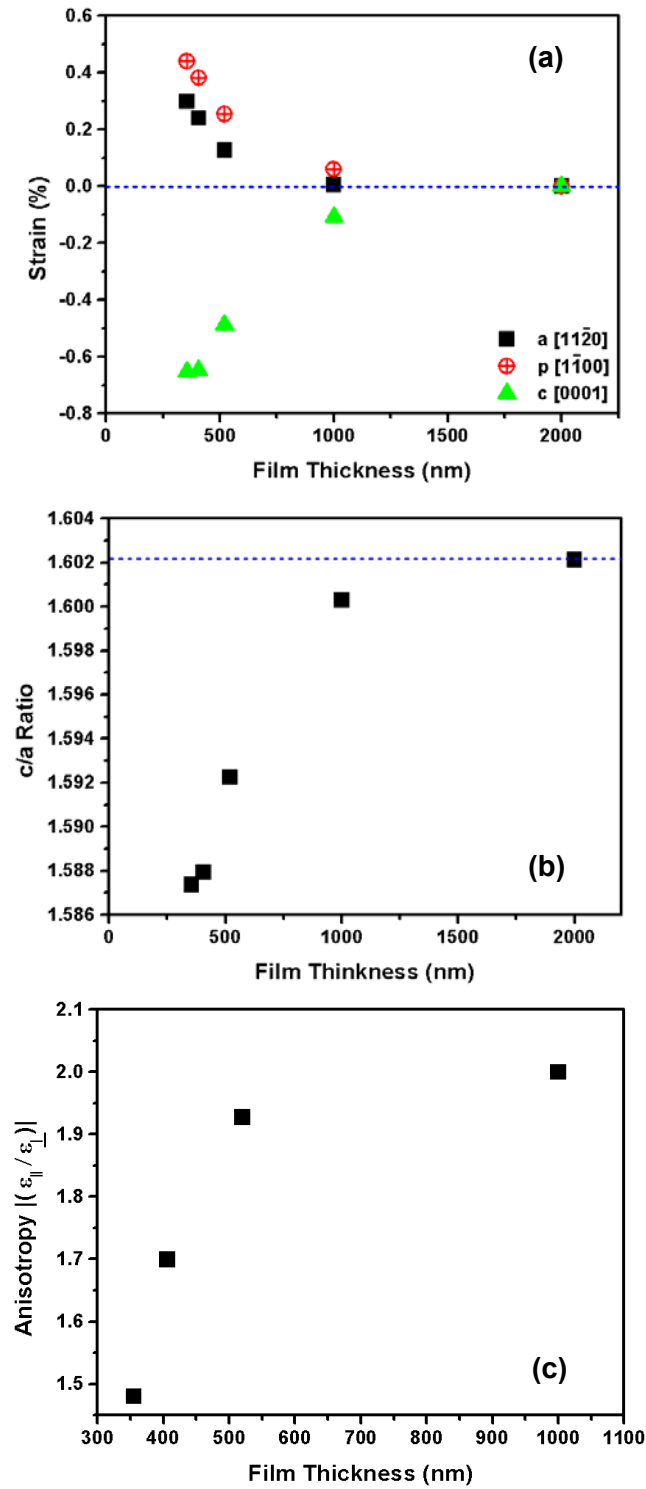


Figure 4.3: (a) Strain variation with a-plane ZnO films thickness, bulk ZnO lattice parameters used as reference, (b) plot of the c/a ratio and (c) Strain anisotropy $|(\epsilon_{||}/\epsilon_{\perp})|$ with a-plane ZnO film thickness.

4.2. Strain with Mg composition

ZnO can be alloyed with MgO to form $\text{Mg}_x\text{Zn}_{1-x}\text{O}$ as discussed earlier. It was also shown in section 3.2.1 that Mg atom substitutes a Zn atom in the wurtzite crystal lattice of ZnO. This is primarily because the tetrahedrally coordinated and octahedrally coordinated Zn^{2+} ion radii are very close to the tetrahedrally coordinated and octahedrally coordinated Mg^{2+} ionic radii respectively. This substitution would lead to lattice distortion in $\text{Mg}_x\text{Zn}_{1-x}\text{O}$ films with Mg composition [11]. However, as long as $\text{Mg}_x\text{Zn}_{1-x}\text{O}$ films retain the wurtzite crystal structure it can be treated in a similar way and compared to bulk ZnO films. Theoretically calculated change in the lattice parameters (nm) of bulk $\text{Mg}_x\text{Zn}_{1-x}\text{O}$ wurtzite crystal with Mg composition is given by: [9, 14]

$$\begin{aligned} c &= 0.520661 - 0.017x \\ a &= 0.324982 + 0.0036x \end{aligned} \tag{4.4}$$

Non-polar a-plane $\text{Mg}_x\text{Zn}_{1-x}\text{O}$ thin films were deposited on r-sapphire substrates. The growth temperature ($\sim 520^\circ\text{C}$) and the gas-flow conditions were maintained constant for all the samples during MOCVD growth, with a typical growth rate of $\sim 500\text{nm/hr}$. The film thickness of samples was maintained to be $\sim 520\text{nm}$, while changing the Mg/Zn metalorganic flow-ratio varied Mg composition in the films. The composition of the samples was monitored using optical transmission spectroscopy and photoluminescence (PL) spectra. The error in composition measurement between PL and transmission spectra is less than 0.1%. XRD measurements were done on the samples using a synchrotron radiation source at Brookhaven National Labs followed by lattice refinement to obtain the unit cell parameters. The error factor for lattice refinement was of order of 10^{-4}nm . The deviation in γ (denoted as θ), with Mg composition is listed in table 4.2.

Figure 4.4 (a), (b) and (c) show plots orthogonal axes lattice parameters along $a[1\bar{1}20]$ and $p[\bar{1}100]$ and $c[0001]$ of a-plane $\text{Mg}_x\text{Zn}_{1-x}\text{O}$ film with Mg composition.

Table 4.2: Lattice parameters along orthogonal parameters $a[1\bar{1}20]$, $p[\bar{1}100]$ and $c[0001]$ axis, with variation in a-plane $\text{Mg}_x\text{Zn}_{1-x}\text{O}$ film composition.

Mg (%)	$a \pm \Delta a$ (\AA) $[1\bar{1}20]$	$p \pm \Delta p$ (\AA) $[\bar{1}100]$	$c \pm \Delta c$ (\AA) $[0001]$	$\gamma \pm \Delta\gamma$ (degrees)
0	3.25396 ± 0.000517	5.64313 ± 0.00089	5.18115 ± 0.000344	120.25 ± 0.0126
12	3.26196 ± 0.000448	5.6551 ± 0.00078	5.17588 ± 0.000322	120.181 ± 0.0114
15	3.26571 ± 0.000499	5.6642 ± 0.00087	5.16892 ± 0.000189	120.271 ± 0.0127
25	3.27587 ± 0.000274	5.68196 ± 0.00047	5.15572 ± 0.000180	120.278 ± 0.0066

It is observed that the $a[1\bar{1}20]$ and $p[\bar{1}100]$ lattice parameters increase, while $c[0001]$ lattice parameter decreases with an increase in Mg composition.

Since, change in Mg composition changes the lattice parameters (not dependent on lattice relaxation) as mentioned in equation 4.2 and also changes strain-state due to mismatch with the r-sapphire substrate it is difficult to independently resolve lattice distortion and strain relaxation corresponding to substrate mismatch and Mg composition variation. However, as mentioned earlier as long as wurtzite crystal structure is retained, strain can still be calculated with respect to bulk ZnO lattice parameters as shown in figure 4.5 (a). It is observed that an increase in Mg composition in $\text{Mg}_x\text{Zn}_{1-x}\text{O}$ films increases the out-of-plane (along $a[1\bar{1}20]$) strain and in-plane strain along $p[\bar{1}100]$. In-plane strain along $c[0001]$ becomes more negative with increase in Mg composition. The in-plane strain along $p[\bar{1}100]$ and $c[0001]$ is observed to be anisotropic, corresponding to a tensile stress along in-plane $p[\bar{1}100]$ and a compressive stress along in-plane $c[0001]$.

The out-of-plane stress is assumed to be zero as it the direction of unrestrained growth. Theoretically calculated (c/a) ratio to measured (c/a) ratio is plotted in figure 4.5 (b). A comparison of theoretically calculated (c/a) lattice parameter ratio from equation 4.2 to the measured (c/a) ratio shows similar behavior and slope with varying Mg composition. The (c/a) ratio is observed to decrease linearly with increase in Mg composition in the $\text{Mg}_x\text{Zn}_{1-x}\text{O}$ films. The vertical shift between the theoretical and the measured value accounts for the strain in the samples. An increase in Mg composition decreases the (c/a) ratio towards relaxed wurtzite MgO (c/a) ratio of 1.204 [86]. An increase in Mg composition increases the unit cell volume of $\text{Mg}_x\text{Zn}_{1-x}\text{O}$ almost linearly to $\sim 47.5 \text{ \AA}^3$ (for $x = 0$) to $\sim 47.91 \text{ \AA}^3$ (for $x = 0.25$) and the strain anisotropy is observed to decrease from ~ 1.927 ($x = 0$) to ~ 1.03 (for $x = 0.25$) as seen in figure 4.5 (c).

4.3 Reciprocal space maps

Mapping the intensity of a reflection in reciprocal space is good analytical technique to study crystalline periodicity, orientation, and defects. Asymmetry in reciprocal space map (RSM) done in bisecting mode is indicative of weak defects such as vacancies and interstitials in crystalline thin films, while the presence of side lobes around the main intensity is indicative of dislocation loops. Broadening of the RSM in the lateral direction is indicative of bending of the atomic planes, while a broadening in the longitudinal direction is indicative of lattice distortion. The displacement of the center of RSM along the scanned azimuths gives a quantitative measure of the strain along the two axes.

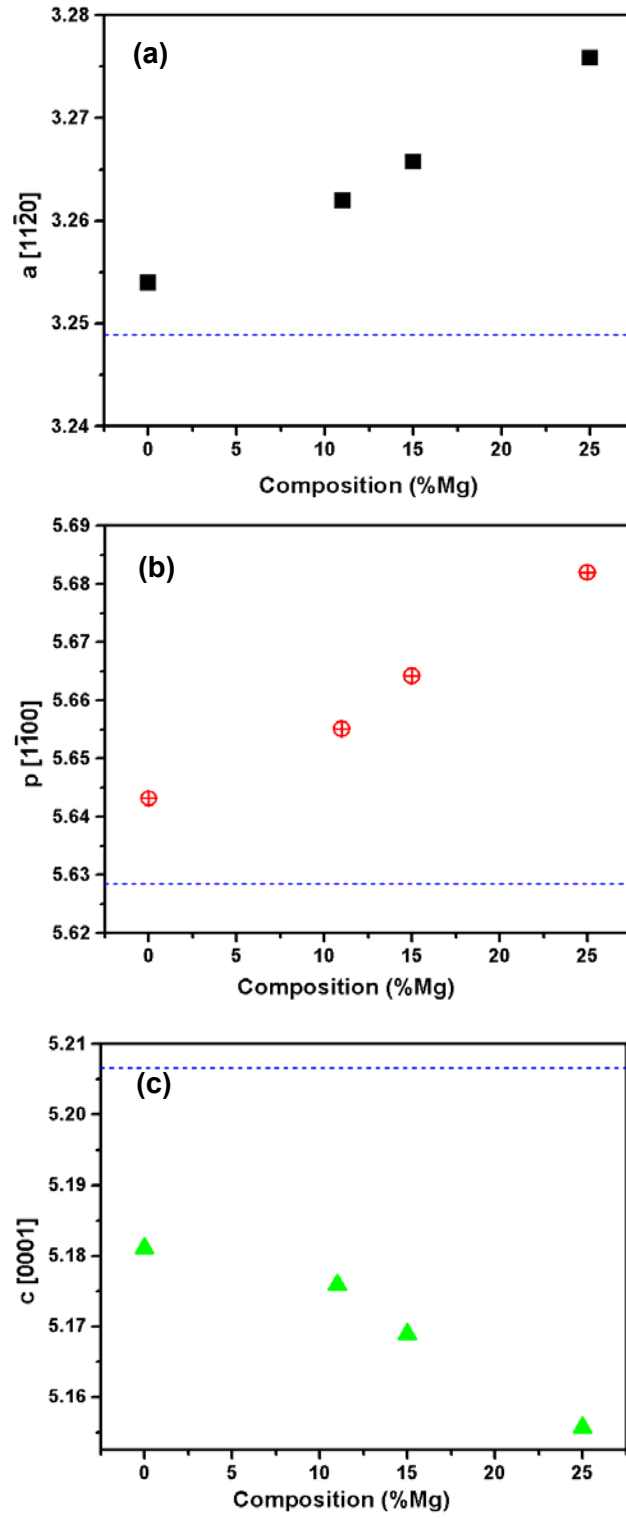


Figure 4.4 (a), (b) and (c) show plots orthogonal axes lattice parameters along $a[11\bar{2}0]$ and $p[1\bar{1}00]$ and $c[0001]$ of a-plane $\text{Mg}_x\text{Zn}_{1-x}\text{O}$ film with Mg composition.

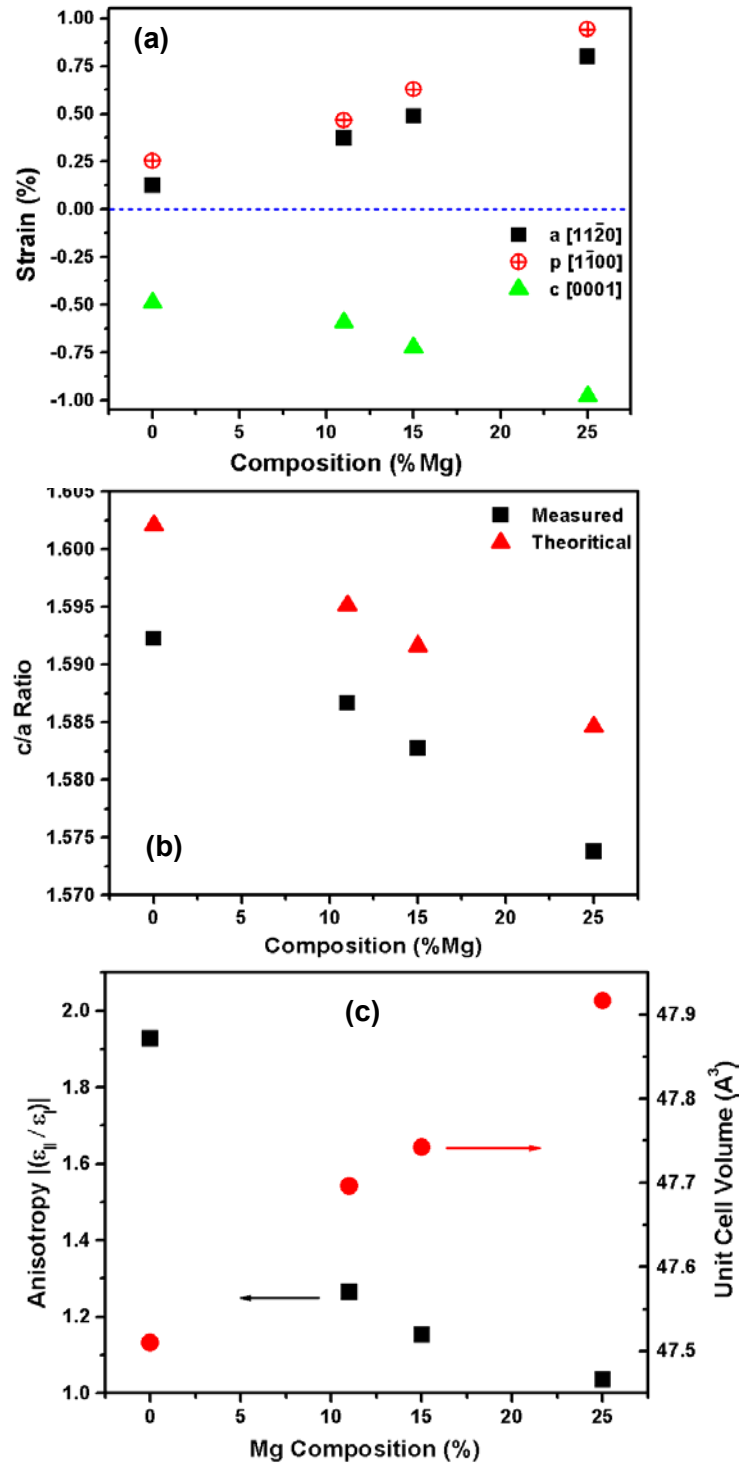


Figure 4.5 (a) Strain in a-plane $\text{Mg}_x\text{Zn}_{1-x}\text{O}$ film, (b) Plot of theoretically calculated (c/a) ratio to measured (c/a) ratio and (c) Strain anisotropy $|(\epsilon_{||}/\epsilon_{\perp})|$ and unit cell volume with Mg composition, reference relaxed lattice of bulk ZnO is used

For qualitative analysis of defects and mosaic in the a-plane ZnO and $\text{Mg}_x\text{Zn}_{1-x}\text{O}$ films, RSMs were done around a off-axis reflection. These scans were carried out using a synchrotron radiation at Brookhaven National Labs at beamline X6B, in bisecting mode around the $(20\bar{2}5)$ reciprocal points. Figure 4.6 (a) and (b), shows the reciprocal space maps along a-plane ZnO $(20\bar{2}5)$ and $\text{Mg}_{0.15}\text{Zn}_{0.85}\text{O}$ $(20\bar{2}5)$ reflections, respectively. The RSM is symmetric and do not show presence of additional lobes around the scanned region. Symmetry indicates low density of weak defects such as vacancies, interstitials, and absence of intensity additional lobes indicate low density of strong defects such as dislocation loops. The intensity spread along $(h0\bar{h}0)$ plane is similar to the intensity spread along $(000l)$ planes. It is also observed that the center of the peak is shifted from $(20\bar{2}5)$ reflection both along $(000l)$ and $(h0\bar{h}0)$ that the film is strained along both azimuths ZnO $(20\bar{2}0)$ and ZnO (0005) . The RSM of a-plane $\text{Mg}_{0.15}\text{Zn}_{0.85}\text{O}$ film is less symmetric compared to ZnO map.

The intensity spread along $(000l)$ is much larger than the intensity spread along $(h0\bar{h}0)$, thus the a-plane $\text{Mg}_{0.15}\text{Zn}_{0.85}\text{O}$ film has larger density of interstitials and vacancies compared to ZnO films grown under similar growth conditions. Side lobes are not observed from the RSMs indicating low density of dislocation loops. The lateral broadening in $\text{Mg}_{0.15}\text{Zn}_{0.85}\text{O}$ film is also observed to be much larger than ZnO films indicating larger bending of atomic planes compared to ZnO.

Summary

In this chapter we did comprehensive characterization and analysis of strain in a-plane ZnO and $\text{Mg}_x\text{Zn}_{1-x}\text{O}$ films using x-ray diffraction from a synchrotron source.

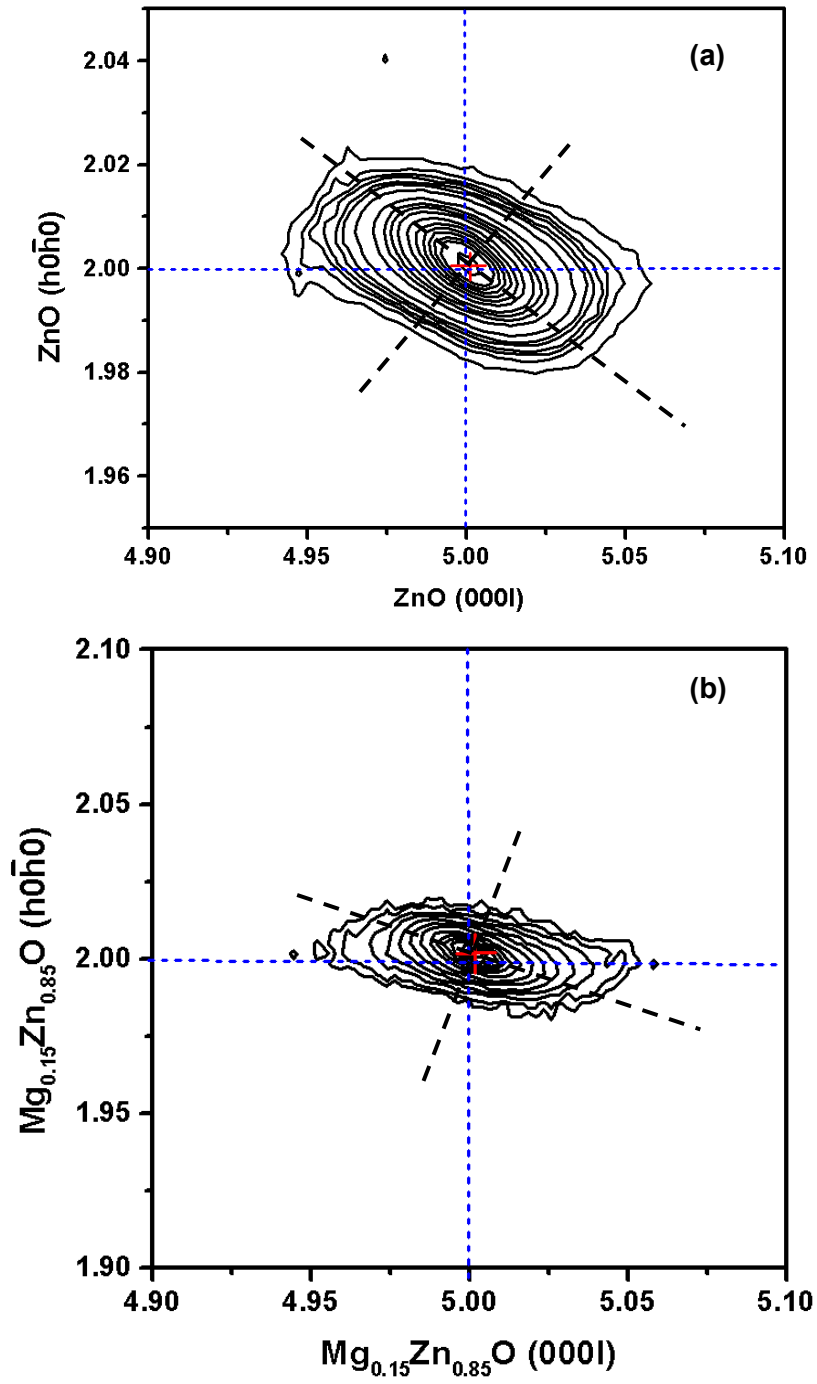


Figure 4.6: (a) and (b), shows the reciprocal space maps along a-plane ZnO ($20\bar{2}5$) and $\text{Mg}_{0.15}\text{Zn}_{0.85}\text{O}$ ($20\bar{2}5$) reflections, respectively.

Strain behavior was analyzed for film thickness and Mg composition variations. It was observed that the in-plane strain is anisotropic along and perpendicular (along $p[\bar{1}100]$) to the in-plane c-axis $[0001]$. The strain anisotropy is reduced as the film thickness increases till complete relaxation occurs at film thickness of $\sim 2000\text{nm}$. In-plane stress is also anisotropic with tensile component along $p[\bar{1}100]$ and compressive component along $[0001]$. When the Mg composition in the films is varied the in-plane stress and strain anisotropy increases. Reciprocal space maps done around the $(2\bar{0}25)$ reflections of films indicate low density of dislocation loops. Density of vacancies and interstitial defects is observed to be higher for $\text{Mg}_{0.15}\text{Zn}_{0.85}\text{O}$ films as compared to ZnO films. Films are observed to be strain along both $(2\bar{0}20)$ and (0005) azimuths.

CHAPTER 5: INTERFACE AND SURFACE PROPERTIES

For optimal performance, thin films should possess specific mechanical, electrical, or optical properties that are strongly influenced by the microstructural qualities of the films such as crystalline state, crystallographic orientation, crystallite size, stresses and strain etc. Furthermore, detailed understanding of the surface morphology and interface properties is imperative for development of heterostructures and quantum wells. In this section we discuss the stress-strain, surface and interface, and optical properties of the $\text{Mg}_x\text{Zn}_{1-x}\text{O}$ films using comprehensive characterizations and analysis.

5.1 INTERFACE PROPERTIES

Interface structure and properties of thin films are critical for several device applications. Interface defects and roughness plays a key role to achieve confinement effect in heterostructures and quantum wells. Especially in the case of a-plane ZnO and $\text{Mg}_x\text{Zn}_{1-x}\text{O}$ films, since the strain in the films is anisotropic, study of the interface structure and defects is important. In this section we discuss the interface of a-plane ZnO and $\text{Mg}_x\text{Zn}_{1-x}\text{O}$ films with r-sapphire substrate.

Interface structure of a-plane ZnO and $\text{Mg}_x\text{Zn}_{1-x}\text{O}$ films grown on r- Al_2O_3 substrates have been characterized by high-resolution transmission electron microscopy (HRTEM) using a 200KeV Topcon 002B with LaB_6 filament [11, 22, 23]. Figure 5.1 (a) and (b) shows the interface of non-polar ZnO film with r-sapphire and selected area diffraction (SAED) pattern from the film and the substrate, respectively. Figure 5.2 (a) and (b) shows the interface and SAED pattern from a non-polar $\text{Mg}_{0.30}\text{Zn}_{0.70}\text{O}$ films,

respectively. The c-axis of the films that lies in the growth plane is pointing normal to the plane of figures 5.1 (a) and 5.2 (a).

HRTEM images show that the interface of both ZnO and $\text{Mg}_{0.30}\text{Zn}_{0.70}\text{O}$ films with the r-sapphire substrate is abrupt and semi-coherent. The films are strained along the $[1\bar{1}00]$ direction near the interface and the strain relaxes away from the interface. Strain relaxation in the thin film leads to interface misfit dislocations. The misfit dislocations of the ZnO film are found to be equally spaced with average spacing of $\sim 3\text{nm}$ and restricted to the film-substrate interface extending towards the c-axis. When the misfit dislocation is formed at the film substrate interface by glide on a crystallographic plane, such as $(1\bar{1}00)$ plane in case of a-plane ZnO on r-sapphire, it does so by drawing elastic energy from background mismatch strain field. Thus resulting is partial relaxation of mismatch strain in the vicinity of the misfit dislocation. However, at certain distance from the dislocation line, the mismatch strain remains un-relaxed based on the initial mismatch with the substrate. In such a case, the misfit dislocations are equally spaced along the film substrate interface. The spacing of such misfit dislocations is dependent on the energy of the mismatch strain field [87]. In case of a-plane ZnO on r-sapphire substrate, since the mismatch along in-plane m-axis $[1\bar{1}00]$ is 18.3% which is much higher than the mismatch along c-axis $[0001]$ (1.53%), the dislocation line lies in the m-plane along the c-axis direction in an attempt to relax the larger mismatch.

In case of a-plane $\text{Mg}_x\text{Zn}_{1-x}\text{O}$ films, the mismatch strain field is different compared to ZnO and dependent upon Mg composition in the films. So, the average spacing of the misfit dislocations at the interface would also be Mg composition dependent.

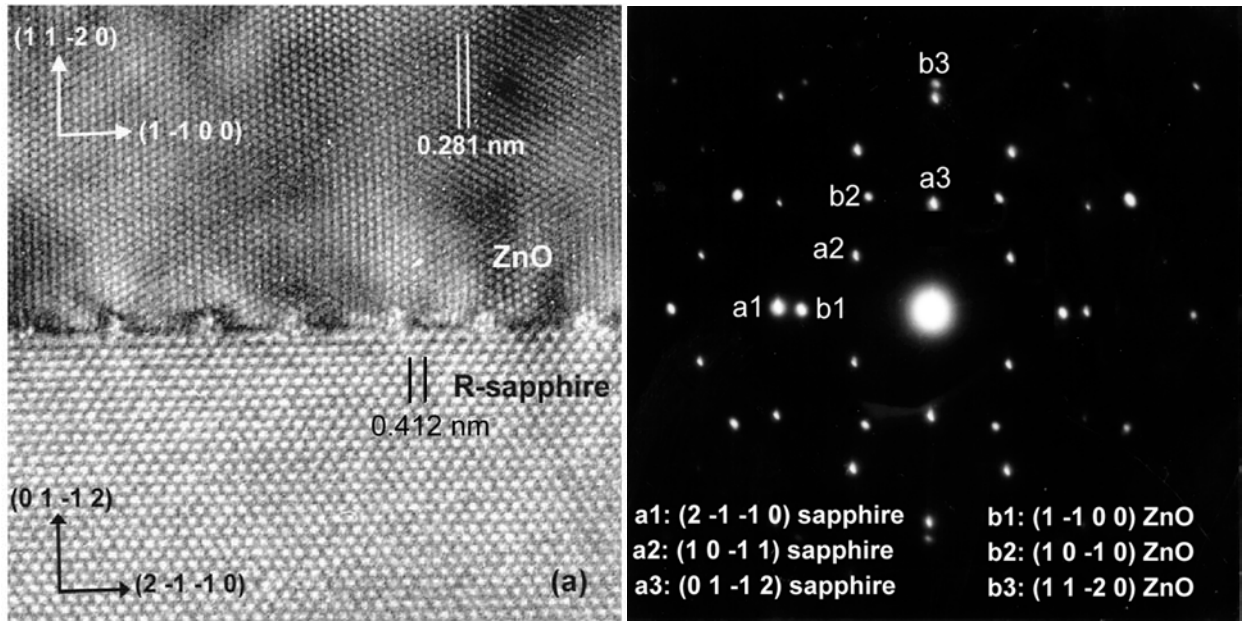


Figure 5.1 (a) and (b) show the interface of non-polar ZnO film with r-sapphire and selected area diffraction (SAED) pattern from the film and the substrate, respectively [22, 23].

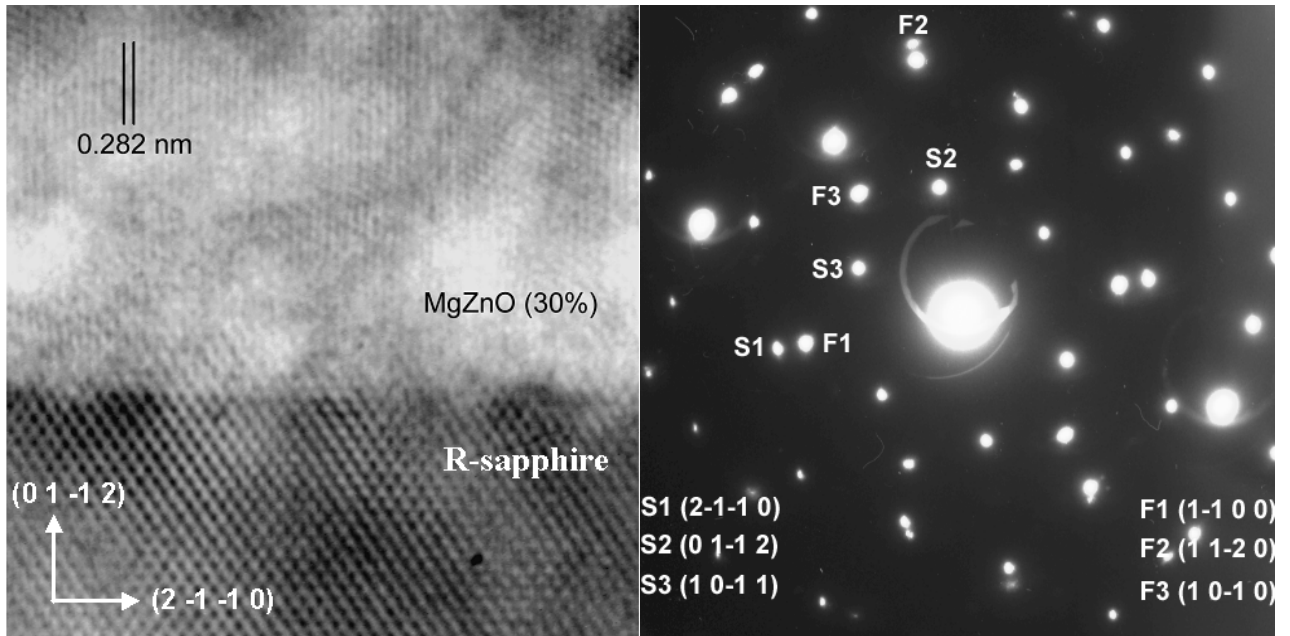


Figure 5.2 (a) and (b), show the interface and SAED pattern from a non-polar $\text{Mg}_{0.30}\text{Zn}_{0.70}\text{O}$ films, respectively [11, 23].

From the HRTEM image in figure 5.2 (a) it is observed that the d-spacing along $[1\bar{1}00]$ for the $\text{Mg}_{0.30}\text{Zn}_{0.70}\text{O}$ film away from the interface is found to be $\sim 0.282\text{nm}$, resulting in a-lattice parameter of $\sim 0.3255\text{nm}$ for the $\text{Mg}_{0.30}\text{Zn}_{0.70}\text{O}$ films, indicating partially relaxed films. The SAED patterns show sharp diffraction spots from the ZnO and $\text{Mg}_{0.30}\text{Zn}_{0.70}\text{O}$ films as well as the r-sapphire substrate, indicating good overall crystallinity of the films. It can be observed that the diffraction spots of the films do not overlap with the diffraction spots of the r-sapphire substrate, indicating partial relaxation in the films as observed in HRTEM images. The diffraction spots further confirm that the epitaxial relationship between the film and the r-sapphire substrate is retained for $\text{Mg}_{0.30}\text{Zn}_{0.70}\text{O}$ films as:

$$\begin{aligned} &\text{Mg}_{0.30}\text{Zn}_{0.70}\text{O} (11\bar{2}0) \parallel \text{Al}_2\text{O}_3 (01\bar{1}2), \\ &\text{and, } \text{Mg}_{0.30}\text{Zn}_{0.70}\text{O} [0001] \parallel \text{Al}_2\text{O}_3 (0\bar{1}11). \end{aligned}$$

Influence of Interface Misfit Dislocations

Interface misfit dislocations may also affect the surface and interface morphology in a-plane ZnO and $\text{Mg}_x\text{Zn}_{1-x}\text{O}$ films. We have already observed surface fluctuations in a-plane ZnO and $\text{Mg}_x\text{Zn}_{1-x}\text{O}$ thin films grown on r-sapphire substrates in figure 3.5 (a) and (b). Earlier, fluctuations in the surface shape of partially relaxed thin films have been correlated to the presence of interface misfit dislocations [87]. Figure 5.3 shows (a) schematic of periodic misfit dislocations at the epitaxial thin film – substrate interface, (b) Lattice schematic of the a-plane ZnO/r-sapphire interface with misfit dislocations. Misfit dislocations are produced as a consequence of strain relaxation in lattice mismatched thin films.

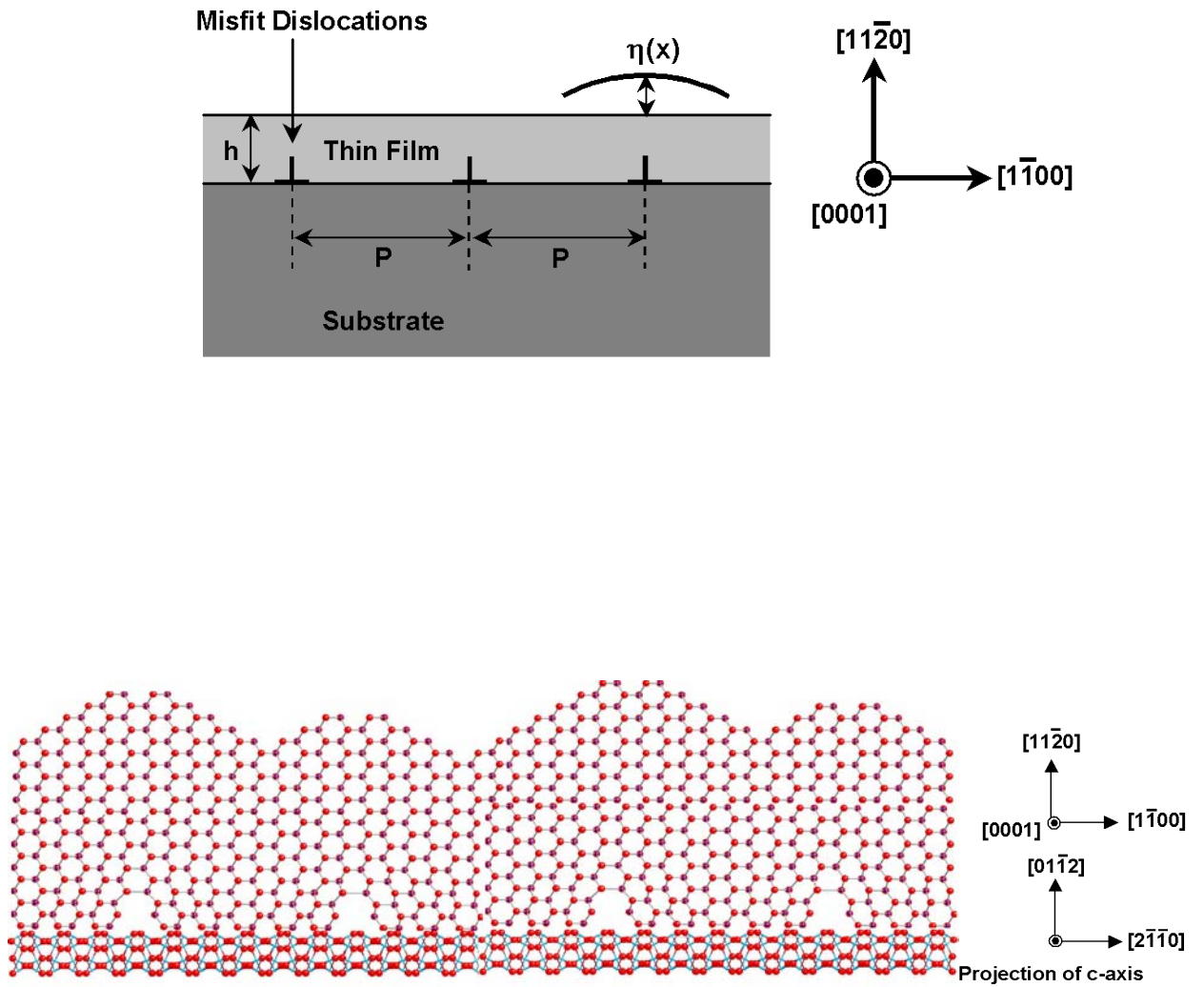


Figure 5.3 shows (a) schematic of misfit dislocations at the epitaxial thin film – substrate interface, (b) Lattice schematic of the a-plane ZnO/r-sapphire interface with misfit dislocations [87].

The site of misfit dislocation would be expected to have lower mismatch compared to rest of the film, thus subsequent nucleation on the growth surface would occur at sites with misfit dislocations. This results in anisotropic nucleation and mass transport on the growth surface leading to surface fluctuations $\eta(x)$. As observed in figure 5.1, the interface misfit dislocations produced at the ZnO/ r-sapphire interface is periodic with $P = \sim 3\text{nm}$. Furthermore, since the misfit dislocations propagate along the c-axis [0001] of a-plane ZnO, the resulting surface fluctuations would occur perpendicular and propagate in the direction of crystallographic c-axis [0001] of a-plane ZnO, resulting in anisotropic surface morphology. This could possibly explain the surface morphology of the a-plane films observed in FESEM images. In subsequent section we investigate the surface morphology anisotropy in a-plane ZnO and $\text{Mg}_x\text{Zn}_{1-x}\text{O}$ films.

5.2 SURFACE PROPERTIES

In order to study and control the surface morphology of the a-plane films our group at Rutgers University collaborated with Prof. Ulrike Diebold's research group at the Department of Physics, Tulane University, New Orleans, LA 70118. Surface characterizations were done using Scanning Tunneling Microscopy (STM) [23]. Surface morphology and structure was also studied using Atomic Force Microscopy (AFM) and Low Energy Electron Diffraction (LEED).

5.2.1 MORPHOLOGY ANISOTROPY

STM is a powerful technique for analyzing surface morphology and structure even at atomic levels. STM works on the principle of quantum tunneling of electrons

through the between a conductive tip probe and a metallic or semiconducting surface. The variations in the current as the probe passes over different surfaces are used for imaging. Though STM can reveal detailed information about surface morphology and structure, it is challenging technique because it requires very sharp probe tips, and conducting and extremely clean sample surfaces [88]. Thus before STM imaging the sample surface is usually cleaned to remove surface contaminants.

In this work STM imaging is done in an UHV system with a base pressure of less than 1×10^{-10} mbar. The system is also equipped with experimental facilities for low-energy electron diffraction (LEED) and Auger electron spectroscopy (AES). All STM data were collected at room temperature in the constant current mode with positive sample bias voltage between 1.9 and 2.5V and with tunneling currents of 0.3 – 2.3nA. X-ray photoelectron spectroscopy (XPS) experiments were performed using a non-chromatized x-ray source (Al $K\alpha$, $h\nu = 1486.6\text{eV}$) and a hemispherical analyzer in a separate UHV chamber equipped with XPS and LEED to characterize the surface contaminants. The photon incidence angle was 57.5° and the photoelectrons were collected normal to the surface. XPS and AES measurements on the samples without any *in-situ* treatment confirmed the surface composition and cleanliness with carbon as the only surface contaminant. Surface cleaning was required to remove the carbon contamination and to obtain high quality STM images of the surface. Two different cleaning procedures were used and compared to ensure that the cleaning process does not modify the surface. In the first method, the samples were annealed in an oxygen background pressure of 1×10^{-6} mbar at $\sim 500^\circ\text{C}$ for 10-15 min, giving well-defined (1x1) patterns showing a good long-range periodic order on the surface. In the second method,

the samples were sputtered using 1-3 keV Ar^+ ions at current of $\sim 1\mu\text{A}$ for 5 - 10min ($p_{\text{Ar}} = 10^{-5}$ to 10^{-6} mbar) followed by UHV annealing at ~ 500 - 600°C .

The annealing temperature during cleaning was maintained similar to film growth temperature, to avoid any surface modification. The overall surface morphology of oxygen-annealed films was found to be similar to those of the sputtered/UHV-annealed films. Both cleaning procedures were adequate to remove any contamination detectable in XPS and AES. The large-scale STM images presented in Figure 5.4 (a) and (b) shows STM images taken at $2000\text{nm} \times 2000\text{nm}$ and $50\text{nm} \times 50\text{nm}$ scale of a-plane ZnO film surface, respectively. The figures show a characteristic ripple-like surface morphology with needle-like features, typically 150 - 400nm wide, 10 - 40nm high and 1500 - 3000nm long. The needles run predominantly along the crystallographic c-direction. The smaller-scale ($50\text{nm} \times 50\text{nm}$) STM images shown in Figure 5.4(b) reveal surfaces with many small terraces (15 - 30nm wide and 20 - 40nm long) terminated by mono-atomic step edges. The a-plane ZnO film exhibited significant surface roughness anisotropy (ripples), with long narrow and elongated terraces parallel to the c-axis. The ripples had a symmetrical stacking on both sides. The ripple-like morphology, initially seemed to be similar to the one observed for the heteroepitaxial growth of SiGe/Si(001) [40, 41, 89-91], and even for Si/Si(001) [89-91] homoepitaxy. Step bunching observed in Si/Ge superlattices has also been major cause of anisotropic surface morphology. Step bunching has one-fold symmetry with surface waviness occurring in a specific direction, with the orthogonal in-plane direction being smooth. Step bunching occurs due to substrate mono-atomic steps causing strain in the grown films. The anisotropic surface is an attempt to release this strain by step bunching.

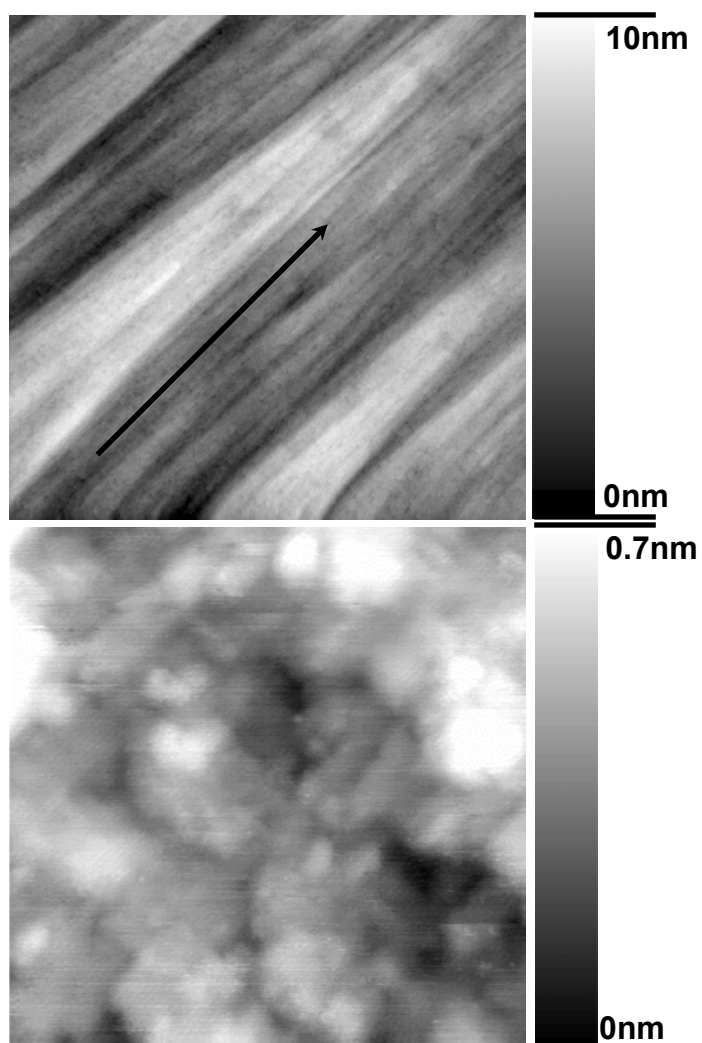


Figure 5.4 (a) and (b) shows STM images of the film surface taken at 2000nm x 2000nm and 50nm x 50nm scale, respectively. The arrow shows the direction of c-axis.

The lateral correlation length of the film surface morphology in such case is related to the average distance of the step edges on the substrate surface [41]. However, in the case of ZnO, small-scale atomically resolved STM images with higher resolution as shown in figure 5.5, do not show step bunching, and show high surface ordering of atoms. Furthermore, as observed from the STM images (figure 5.4) the lateral correlation distance does not match with the distance of step edges on the r-sapphire substrate. Nevertheless even though step bunching may not be primary cause of the observed anisotropic surface morphology, the orientation of the step edges can decide the orientation of the observed ripples. Local strain fields due to step edges can cause such an effect, because this process will be energetically less costing as compared to random formation of surface morphology.

The surface structure and morphology a-plane $\text{Mg}_x\text{Zn}_{1-x}\text{O}$ ($x = 0.15$) films were studied using STM in UHV for comparison. The a-plane $\text{Mg}_{0.15}\text{Zn}_{0.85}\text{O}$ films were grown under similar conditions of deposition temperature and gas flows using MOCVD.

XPS measurements on the a-plane $\text{Mg}_{0.15}\text{Zn}_{0.85}\text{O}$ films also indicated that carbon was the only detectable surface contaminant. Thus the films were cleaned using similar cleaning process described for a-plane ZnO films. XPS measurements did not show any Mg segregation in the as-grown or in oxygen-annealed films and the sputtered/UHV-annealed films. Figure 5.6 (a) and (b) shows STM images of a-plane $\text{Mg}_{0.15}\text{Zn}_{0.85}\text{O}$ film at 2000nm x 2000nm and 50nm x 50nm scale, respectively. While the measured overall surface roughness of the $\text{Mg}_{0.15}\text{Zn}_{0.85}\text{O}$ film shown in figure 5.6 was somewhat higher, this is not considered significant, as STM probes only relatively small patches of the sample.

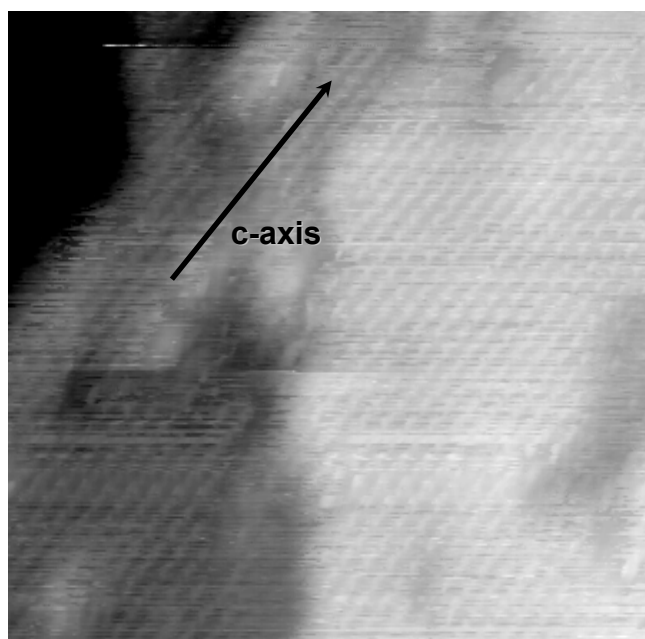


Figure 5.5 shows atomically resolved (20nm x 20nm) STM image of the non-polar ZnO film surface, respectively.

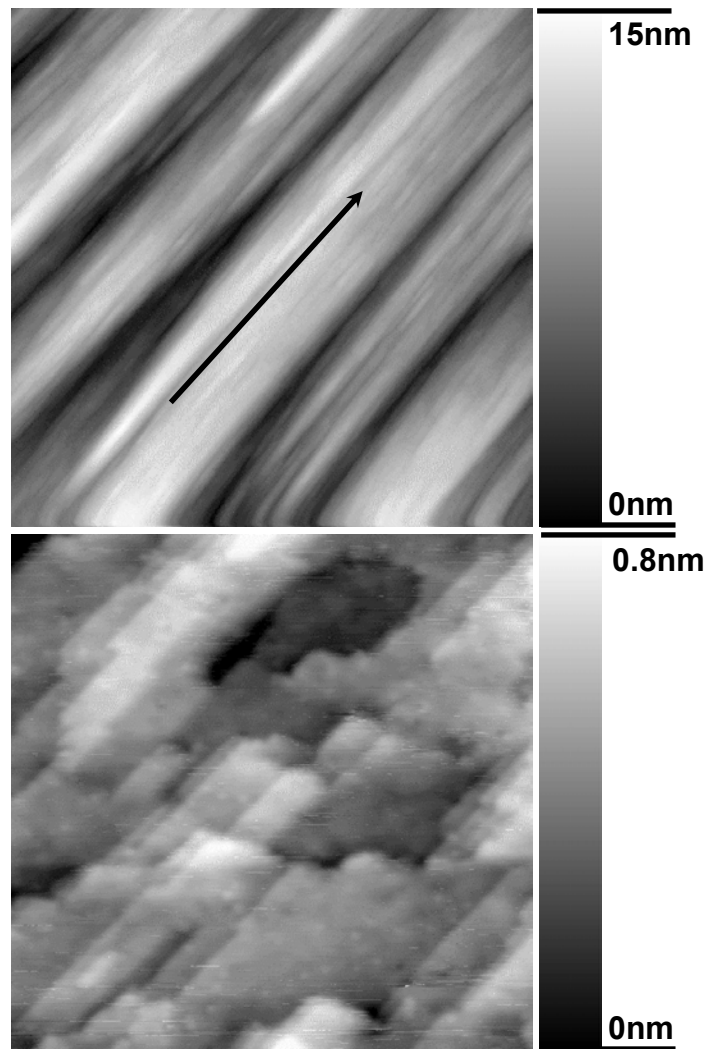


Figure 5.6 (a) and (b) shows STM images of the a-plane $\text{Mg}_{0.15}\text{Zn}_{0.85}\text{O}$ film surface taken at 2000nm x 2000nm and 50nm x 50nm scale, respectively. The arrow indicates the direction of in-plane c-axis.

LEED measurements that average over a larger fraction of surface ($\sim 1\text{mm}^2$) showed qualitatively similar roughness of the two surfaces.

The surface terraces with mono-atomic step edges on a-plane $\text{Mg}_{0.15}\text{Zn}_{0.85}\text{O}$ films observed in smaller-scale ($50\text{nm} \times 50\text{nm}$) STM images are sharper and better defined as compared to that of respective a-plane ZnO films. High resolution atomically resolved STM images could not be taken on $\text{Mg}_{0.15}\text{Zn}_{0.85}\text{O}$ films due to lower conductivity of the films. The film conductivity further reduced with increase in Mg composition making it difficult to obtain STM images of higher Mg composition a-plane $\text{Mg}_x\text{Zn}_{1-x}\text{O}$ films.

Variation of morphology with film composition and thickness:

In order to analyze the surface structure and morphology of higher Mg composition a-plane $\text{Mg}_x\text{Zn}_{1-x}\text{O}$ films, LEED and AFM was used. For comparison, Mg composition difference in the films was achieved by only changing the Zn/Mg metalorganic flow ratio, while keeping the same deposition temperature and, Ar and O_2 flow. Since, LEED involves low energy electrons it is extremely surface sensitive and thus requires highly ordered surfaces to be measured in UHV. LEED works on the theory of multiple scattering of electrons in contrast with single scattering kinematic theory used for x-ray diffraction. Thus the LEED pattern is a two-dimensional reciprocal lattice of the ordered surface projected onto a two-dimensional real space plane [92]. Using the kinematic theory of diffraction the surface ordering and symmetry of atoms can be determined using LEED. AFM uses a micro-cantilever with a sharp tip to scan the surface of a sample. Although resolution obtained for STM is much higher compared to AFM because of exponential dependence of the tunneling current to the distance from the

sample, AFM can be used to scan larger surface area [88]. When the tip is brought close to the surface of the sample, the force between the tip and surface causes a deflection in the cantilever, providing information of the sample surface. AFM does not involve tunneling current unlike STM and can be used for insulating samples [93].

Figure 5.7 shows LEED pattern for varying Mg composition to analyze the surface ordering and crystallinity of a-plane $\text{Mg}_x\text{Zn}_{1-x}\text{O}$ films, with variation in Mg composition. It is observed that the diffraction spots are sharper with increase in Mg composition. This implies an improvement in the surface ordering and symmetry with increase in Mg composition. It is also observed that the diffraction spots are rounder compared to elliptical shape as observed for a-plane ZnO films, possibly due to difference in strain distribution in the films with an increase in the Mg composition.

To better understand the effect of strain and growth kinetics, AFM measurements are carried on the a-plane $\text{Mg}_x\text{Zn}_{1-x}\text{O}$ films to measure the root mean square (rms) surface roughness (ripples) with variation in ZnO film thickness (d) and Mg composition (x) in $\text{Mg}_x\text{Zn}_{1-x}\text{O}$. The rms surface roughness is measured perpendicular to the direction of the surface needles shown in figure 5.4 (a) and figure 5.6 (a).

Figure 5.8 (a) shows a log-log plot of rms roughness of a-plane ZnO films with film thickness. It is observed that the rms roughness increases drastically with increase in 'd' from ~20nm to ~100nm (Region 1) thickness, the roughness increase is more gradual for $\sim 100\text{nm} < d < \sim 1000\text{nm}$ (Region 2). For $d > 1000\text{nm}$ (Region 3), the rms roughness of the films does not change significantly. The observed behavior in the plot of rms roughness versus thickness can be associated with anisotropic mass transport. Anisotropic mass transport can be strain assisted or structure motivated anisotropy in

surface diffusion. Since, the a-plane surfaces of ZnO are terminated with rows of Zn - O dimers, running parallel to the c-axis. These dimer rows represent a template for anisotropic surface diffusion [23, 36, 37]. Anisotropic strain on the other hand causes anisotropic energy barrier to surface diffusion of atoms [87]. Hur et. al. have shown relationship of surface roughness (σ) with deposition time (t) for ZnO films sputtered on c-sapphire substrates, based on kinetics of roughening.

$$\sigma \sim (t)^\beta \quad (5.1)$$

Based on strain-relaxation in the films, the rms roughness of the films was studied and highest roughness was observed for a completely relaxed film [94]. The deposition time (t) can be directly co-related to film thickness (d) [87, 94]. For a layer-by-layer growth mechanism, structure associated surface diffusion and strain contribute to the final morphology and roughness of the films with film thickness (d). Strain assisted energy barrier to surface diffusion is usually larger as compared to structure assisted [87]. In region 1 where the film thickness is small, surface diffusion is primarily strain dominated. Anisotropic in-plane strain as observed in chapter 4 cause anisotropic surface diffusion of atoms leading to formation of ripples as shown in figure 5.4 (a). These ripples increase in height, while not increasing much in width with film thickness, thus increasing the overall rms roughness. For region 2, $\sim 100\text{nm} < d < \sim 1000\text{nm}$, the film is somewhat relaxed due to misfit dislocations. Thus the slope of increase in rms roughness is smaller. In Region 3 ($d > 1000\text{nm}$), the strain in the films is almost relaxed, structure assisted anisotropic mass transport is primary mechanism of surface diffusion, leading to very small increase in roughness with film thickness (d). Figure 5.8 (b) shows a plot of rms roughness of a-plane $\text{Mg}_x\text{Zn}_{1-x}\text{O}$ films with Mg composition.

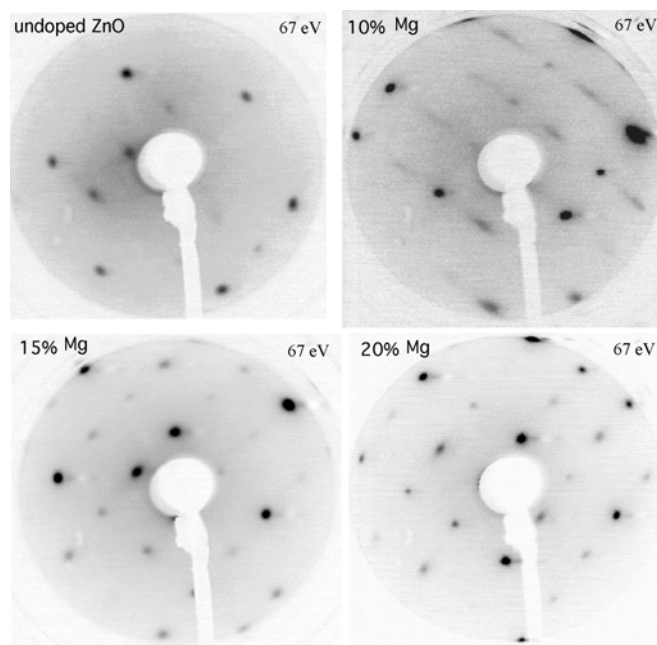


Figure 5.7 shows LEED pattern for varying Mg composition to analyze the surface ordering and crystallinity of a-plane $\text{Mg}_x\text{Zn}_{1-x}\text{O}$ films, with variation in Mg composition.

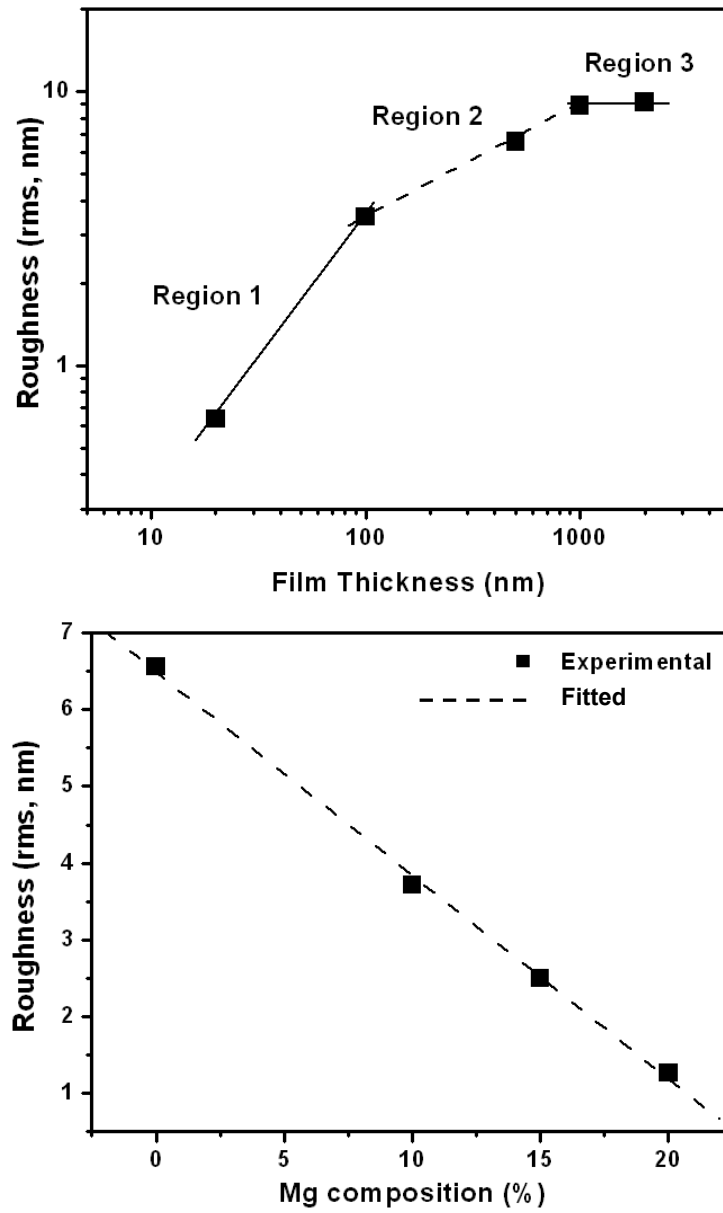


Figure 5.8 (a) shows a log-log plot of rms roughness of a-plane ZnO films with film thickness, (b) shows a plot of rms roughness of a-plane $\text{Mg}_x\text{Zn}_{1-x}\text{O}$ films with Mg composition.

It is evident that the rms roughness is lowered with increase in the Mg composition (x), as also evident from sharper LEED spots in figure 5.7, indicating better surface ordering and symmetry. A linear fit of the rms roughness (σ) with Mg composition (x) shows:

$$\sigma(Mg_xZn_{1-x}O) = \sigma(ZnO) - 0.265(x\%) \quad (5.2)$$

The lowering of the surface roughness could be associated with the difference in growth kinetics and larger strain distribution with Mg composition (reference chapter 4). The change in lattice parameters with Mg composition (x) ('a' lattice parameter increases while the 'c' lattice parameter decreases) also results in overall structure change leading to lower growth rate anisotropy compared to pure ZnO films [9, 13]. The growth kinetics also changes with Mg composition (x) due to lower vapor pressure and lower surface diffusion of heavier metalorganic Mg (MCP₂Mg) as compared to Zn (DEZn).

Thus several reasons could be invoked for the observed surface anisotropy in a-plane Mg_xZn_{1-x}O films, including 1) higher growth rate along [0001] [24]; 2) increased bulk-diffusion along the dislocations; 3) Anisotropic residual strain; 4) high step edge energy [37, 38] for polar step edges (at the narrow end of the terraces), 5) substrate miscut etc.

5.2.2 EFFECT OF SUBSTRATE MISCUT

Substrate miscut is another critical issue that shows a rich influence on surface morphology. Substrate miscut is defined as misorientation in the surface of single crystals. Miscut may be unintentional result of wafer cutting from a single boule, or due to surface polishing of the wafer. Miscut may also be intentional to create vicinal surfaces

with specific well-ordered crystalline step-terrace distribution. Figure 5.9 shows a schematic of the substrate miscut, including the miscut angle (δ) and direction of the miscut. Surface miscut is very important for specific device properties, such as to obtain anisotropic optical and acoustic properties with specific polarization and propagation properties the surfaces need to be cut and polished within a few arc seconds [95]. Surface miscut of a substrate also has significant impact on the thin film properties in case of homo-epitaxial and hetero-epitaxial film growth. Substrate miscut affects the strain distribution and surface diffusion during the epitaxial growth of epitaxial films, thus affecting the overall surface morphology. There have been several reports on miscut measurement of substrates using x-ray rocking curves [95], x-ray reflectivity measurements [40] and surface measurement techniques such as atomic force microscopy [41] and STM [42]. Since, miscut is on the substrate surface; precise miscut measurement requires coupled optical system that keeps a track of the surface tilt and rotation with a diffraction system to align the correct crystallographic orientation.

To measure the miscut of the r-sapphire substrates a Rigaku 4-circle x-ray diffractometer system is used. This system is coupled with a laser beam reflecting off the substrate surface. The substrate is mounted on a goniometer head. Figure 5.10 shows a schematic XRD four-circle configuration setup used for substrate miscut measurement, the figure also shows rotational degrees of freedom of the substrate with respect to the x-ray source and detector. Corrections for initial tilt in mounting is achieved by ensuring that substrate reflecting plane normal is bisecting the incident and reflected x-rays. To achieve this, the sample is rotated about the ϕ -axis and an average of θ -values satisfying diffraction condition is calculated for different ϕ angles.

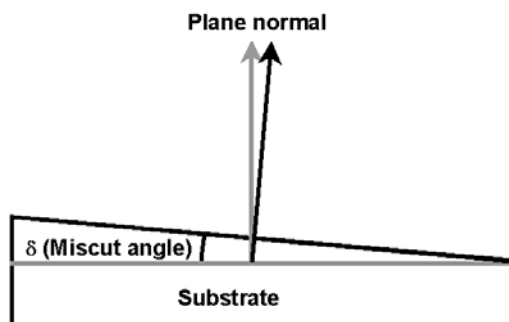


Figure 5.9: Shows a schematic of the substrate miscut, including the miscut angle (δ) and direction of the miscut

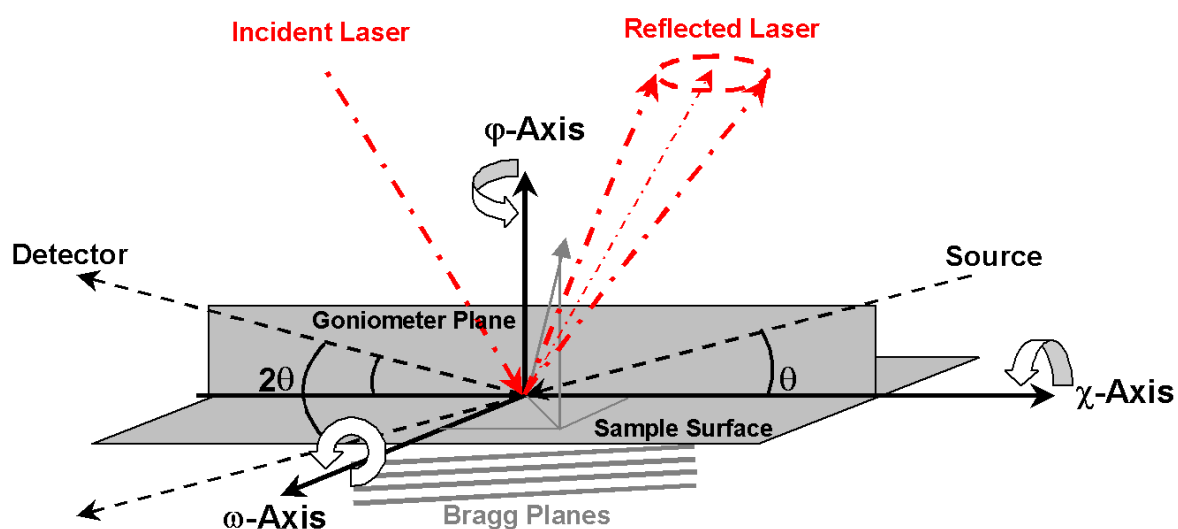


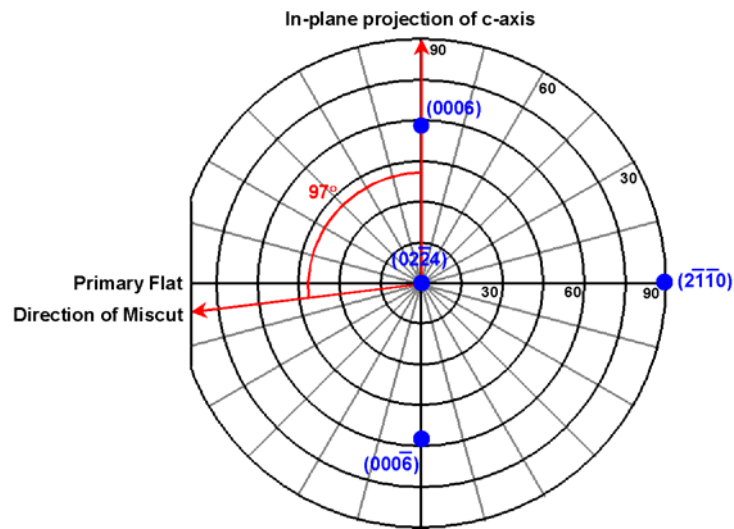
Figure 5.10: Shows a schematic XRD four-circle configuration setup used for substrate miscut measurement, the figure also shows rotational degrees of freedom of the substrate with respect to the x-ray source and detector.

The θ -axis is then moved to this average value and then set to half of the 2θ for the diffraction condition. Once, the mounting tilt is corrected, the Bragg planes of the substrate is then aligned by correcting the ω -axis on the goniometer head for different φ -angles varying from 0° to 360° to ensure that the diffracted beam intensity does not change with substrate rotation about φ -axis. The trajectory followed by the laser beam reflected-off the sample surface during rotation about φ -axis in this setup gives a measure of the substrate miscut. The absolute miscut of the substrate is related to the orthogonal miscut components $\delta_{1,2}$ and $\delta_{3,4}$, according to equation: [95]

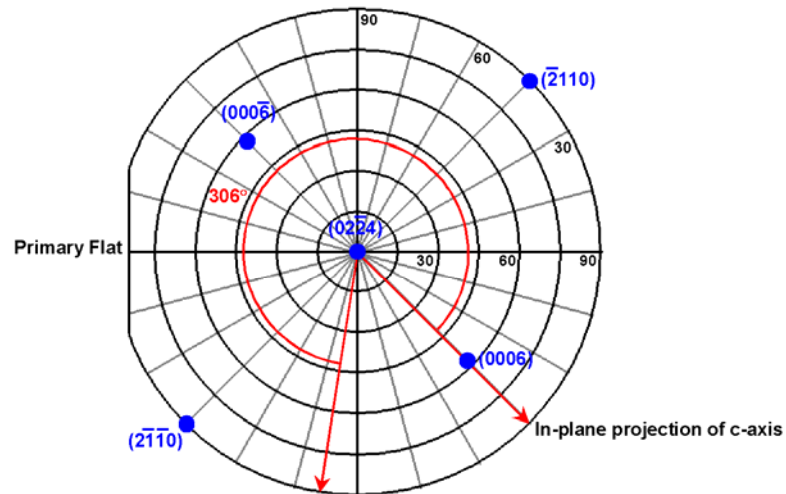
$$(\tan \delta_{sub})^2 = (\tan \delta_{1,2})^2 + (\tan \delta_{3,4})^2 \quad (5.3)$$

Here, $\delta_{1,2}$ correspond to miscut component (average difference in x-ray peak position about ω -axis) for φ -rotation of 0° and 180° , while $\delta_{3,4}$ correspond to substrate miscut component for φ -rotation of 90° and 270° . Figure 5.11 shows the polar plots of a) R-1, b) R-2 and c) R-3, showing the direction of the miscut. The degree of miscut measured for R-1, R-2 and R-3 are listed in Table 5.1.

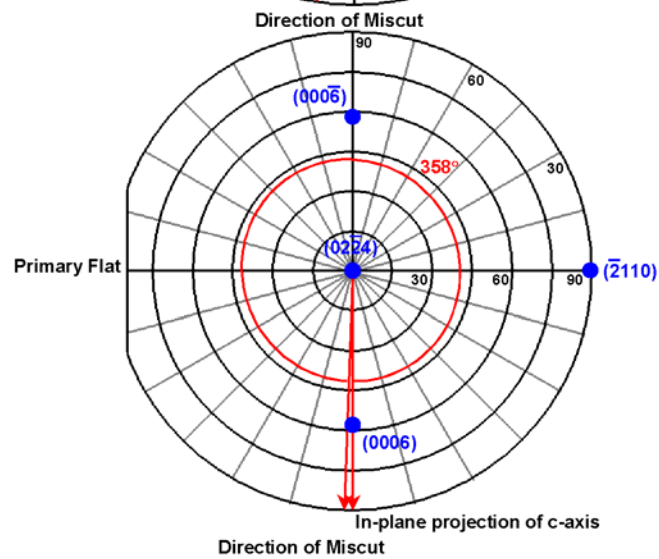
The effect of r-sapphire substrate miscut on the surface morphology anisotropy is studied using STM images taken in UHV. The a-plane ZnO films are deposited on three different miscut r-sapphire substrates (labeled as R-1, R-2 and R-3) under identical MOCVD growth conditions. The surface cleaning procedure to remove surface carbon contamination before STM imaging is identical for films on R-1, R-2 and R-3 (as discussed earlier in section 5.2). Low energy electron diffraction (LEED) and XRD is used to determine the direction of in-plane c-axis of a-plane ZnO films.



(a) R-1



(b) R-2



(c) R-3

Figure 5.11 shows the polar plots of a) R-1, b) R-2 and c) R-3, showing the direction of the miscut.

Table 5.1: The degree of miscut measured for R-1, R-2 and R-3

Substrate	$\delta_{1,2}$ (°)	$\delta_{3,4}$ (°)	δ_{sub} (°)	Miscut direction (counter-clockwise from in-plane projection of [0006])
R – 1	0.04	0.18	0.186	97°
R – 2	0.386	0.068	0.392	306°
R – 3	1.93	0.07	1.931	358°

. Figure 5.12 (a), (b) and (c) shows STM images for a-plane ZnO films at 500nm×500nm resolution, deposited on R-1, R-2 and R-3 respectively. The inset in each figure shows the roughness measured along and perpendicular to in-plane c-axis. The c-axis directions as characterized by LEED, is indicated in the figures with a blue arrow. The surface morphology of the films is similar to that observed in figure 5.4 with ripples elongated along one direction and flattened along the orthogonal direction. The horizontal co-relation length of the ripples is similar for all samples, with periodicity of ~100nm. However the depth and the direction of observed ripples is found to be strongly dependent the degree and direction of r-sapphire substrate miscut. The rms roughness measured along the c-axis (blue line, denoted as $rms_{||}$) does not change much from R – 1 to R – 3. However the rms roughness measured perpendicular to c-axis (along red line, denoted as rms_{\perp}) shows significant variation with r-sapphire substrate. It is observed that rms_{\perp} decreases from ~4.4nm to ~1.4nm from R – 1 ($\delta = 0.186^\circ$) to R – 3 ($\delta = 1.931^\circ$), with rms_{\perp} for R – 2 ($\delta = 0.392^\circ$) being 1.7nm. The direction of in-plane c-axis of ZnO measured using both LEED and x-ray diffraction techniques are found to be consistent.

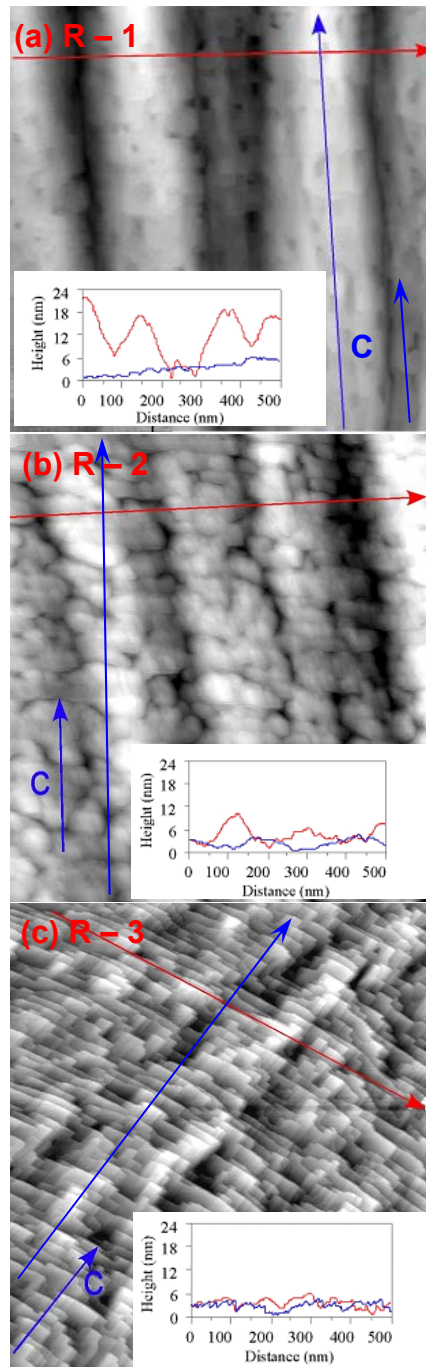


Figure 5.12: (a), (b) and (c) shows STM images for a-plane ZnO films at 500nm×500nm resolution, deposited on R-1, R-2 and R-3 respectively. The inset shows the roughness measured along (blue line) and perpendicular (red line) to in-plane c-axis.

As observed from STM images, the direction of miscut is known by the direction of the step edges. The step edges are formed perpendicular to the direction of miscut in the r-sapphire substrate [96]. From XRD and STM, it is observed that the angle between the in-plane c-axis of ZnO films with respect to the miscut direction is same as angle between in-plane projection of r-sapphire c-axis and the miscut direction.

Difference in the degree and direction of miscut in sapphire substrate affects the growth kinetics and misfit strain in ZnO films. Siah et. al. have shown that a miscut in c-sapphire substrate causes anisotropic strain in the grown c-axis ZnO films [97]. Strain anisotropy ($\Delta\varepsilon$) was found to be related to the thermal expansion coefficient (α) and degree of miscut (δ) according to:

$$\Delta\varepsilon = (\alpha_c - \alpha_a) \Delta T \sin^2 \delta \quad (5.4)$$

Where, α_c and α_a , are the thermal expansion coefficients of sapphire along ‘c’ and ‘a’ axis respectively. ΔT is the difference in difference in the film growth temperature and the room temperature.

The step edges caused due to substrate miscut running perpendicular to the miscut direction provide lower energy barrier for nucleation and film growth. The depth of the step edges dependent on the degree of miscut play a key role in the final morphology and rms roughness of the a-plane films. An increase in sapphire miscut angle corresponds to an increase in the strain in the films, thus resulting in lower rms_{\perp} observed for R – 1 to R – 3. The direction of miscut with respect to the in-plane projection of r-sapphire c-axis determines the direction of the ripples because of epitaxial relationship between a-plane ZnO and r-sapphire, wherein $[0001] \text{ ZnO} \parallel [0001] \text{ Al}_2\text{O}_3$ [22, 23]. The roughness of the starting substrate (r-sapphire) can also influence the overall morphology of the thin films.

However, in this case the rms roughness of the r-sapphire substrates obtained from the commercial vendor is $\sim 0.13\text{nm}$, which is small compared to the observed rms roughness of the a-plane ZnO films, thus it can be neglected.

5.2.3 EFFECT OF GROWTH TEMPERATURE

Another key issue that significantly affects the surface morphology (ripples) is the MOCVD growth temperature. An increase in deposition temperature generally increases the surface roughness and crystallite size of thin films, and results in lowering of ω -rocking curve FWHM indicating improved crystallinity [98, 99]. This section of the chapter discusses the effect of growth temperature on the morphology in a-plane ZnO films. All the samples for this study are deposited under identical gas flow conditions and on identical miscut r-sapphire substrates ($R = 2$). The sample thickness was maintained to be $\sim 500\text{nm}$. The deposition temperature during the MOCVD growth is varied from $\sim 300^\circ\text{C}$ to 580°C to obtain different samples. The surface morphology of all the samples is studied using STM in UHV. Except for samples deposited at 300°C , all other samples show similar rippled surface morphology as observed in figure 5.4 (a). Sample deposited at 300°C shows very smooth surface morphology lacking ripples.

Figure 5.13 shows a plot of the rms surface roughness variation of a-plane ZnO films with growth temperature. As in the previous section, the roughness is measured perpendicular to in-plane c-axis direction (rms_{\perp}). It is observed that the rms roughness of the films initially increase with an increase in deposition temperature from $\sim 0.9\text{nm}$ for 300°C to $\sim 5.6\text{nm}$ for 460°C , and then decreases with further increase in temperature to $\sim 1\text{nm}$ for 580°C .

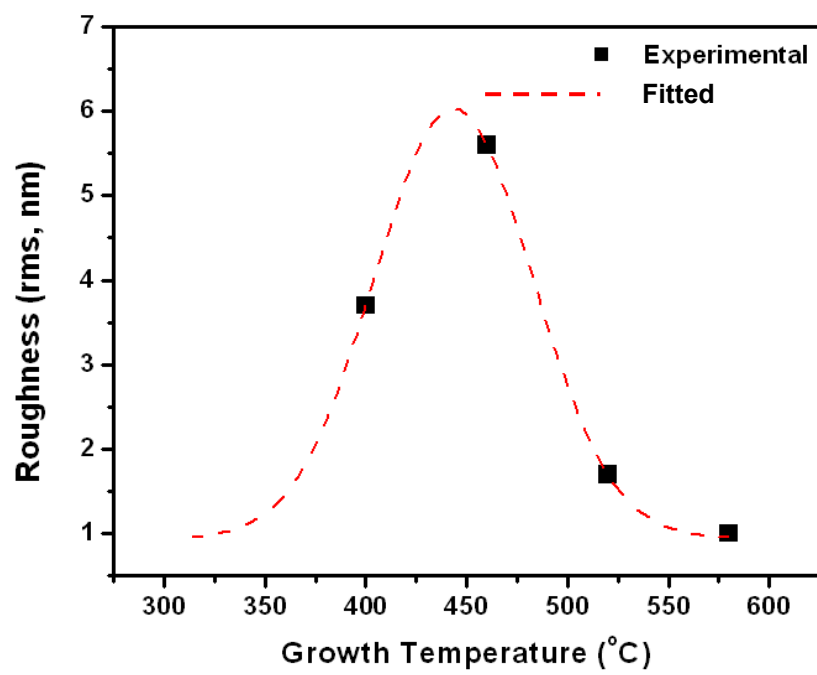


Figure 5.13: Shows a plot of the rms surface roughness variation of the a-plane ZnO films with growth temperature.

Roughness versus deposition temperature is fitted using a Gaussian curve as shown in figure 5.13. The fitted curve shows roughness peaking of $\sim 6.02\text{nm}$ at $\sim 443^\circ\text{C}$. The simulated roughness decreases for increase in temperature above $\sim 443^\circ\text{C}$.

The observed behavior can be explained based on change in the growth mode from cluster growth to a layer-by-layer growth mode with increase in temperature. The change in film crystallinity observed by XRD FWHM in chapter 3 confirms this analysis. At low deposition temperatures, the surface nuclei do not have enough energy for surface diffusion leading to formation of clusters [87]. Thus the lack of ripples on 300°C deposited samples. As the deposition temperature increases the rms roughness increases due to enhanced surface diffusion and also an increase in crystallite size, with samples showing similar rippled surface morphology with periodicity of $\sim 100\text{nm}$ observed in figure 5.4. Increase in deposition temperature improves surface diffusion and thus the film crystallinity (reference figure 3.7, chapter 3). Temperature increase in range $\sim 400^\circ\text{C} < T < \sim 443^\circ\text{C}$ is would be a mixed growth mode between clustered and layer-by-layer. Since, x-ray peak starts appearing at $\sim 400^\circ\text{C}$. Such samples still have poor crystallinity (reference figure 3.7 in chapter 3. Further increase in deposition temperature corresponds to purely layer-by-layer growth mode. Decrease in roughness in this range corresponds to competing process of misfit strain versus surface diffusion, leading to lowering of the roughness. As observed earlier in figure 5.8 (b) that strained films have lower roughness compared to relaxed films. High deposition temperature corresponds to better crystalline films with low density of defects and higher strain components.

Summary:

In this chapter the surface and interface properties of a-plane $\text{Mg}_x\text{Zn}_{1-x}\text{O}$ films deposited on r-sapphire substrates was characterized and the surface morphology was analyzed with respect to film thickness and Mg composition. The effect of substrate miscut and MOCVD deposition temperature on surface morphology was analyzed. The interface was observed to be sharp and semi-coherent. The periodic misfit dislocations observed at the substrate-film interface could lead to fluctuations in surface morphology. The surface of the a-plane films was observed to have anisotropic morphology with ripples elongated along one direction and flattened along the orthogonal in-plane direction. The roughness of the films was observed to increase with films thickness and decrease linearly with Mg composition following: $\sigma(\text{Mg}_x\text{Zn}_{1-x}\text{O}) = \sigma(\text{ZnO}) - 0.265(x\%)$. Increase in substrate miscut from 0.186° to 1.931° decrease the roughness from $\sim 4.4\text{nm}$ to $\sim 1.4\text{nm}$. The direction of miscut in r-sapphire is observed to govern both the roughness as well as the direction of surface ripples. A Gaussian fit is observed for roughness versus deposition temperature. The change in roughness is due to the change in the growth mode of the films from cluster to layer-by-layer growth with increase in temperature.

CHAPTER 6: OPTICAL AND ELECTRICAL PROPERTIES

Optical anisotropy in semiconductor thin films have been used for high-contrast and high-speed modulation of normal incident light [2]. These techniques rely upon manipulation of polarization rotation and phase retardation of linearly polarized light associated with a processing or growth-induced lowering of symmetry [100, 101]. Optical data from bulk ZnO indicates that such films, if single crystal, would possess a strong optical anisotropy at near band gap photon energies around the lowest exciton resonances primarily due to the different selection rules for light polarized parallel and perpendicular to the in-plane c -axis [102]. The in-plane optical anisotropy of ZnO films grown on r-sapphire has been studied, and the anisotropic absorption near the fundamental band edge of ZnO has been used to realize a high contrast, ultrafast optically addressed ZnO UV modulator [2]. In-plane electrical anisotropy is also interesting for development of novel devices. In this chapter we characterize and study the optical and electrical anisotropy in a-plane ZnO and $\text{Mg}_x\text{Zn}_{1-x}\text{O}$ films deposited on r-sapphire substrates. We also do a feasibility study on a-plane ZnO thin film transistors showing anisotropic device characteristics in the two in-plane directions.

6.1 OPTICAL ANISOTROPY

The a-plane ZnO and $\text{Mg}_{0.12}\text{Zn}_{0.88}\text{O}$ thin films are deposited on r-sapphire substrates using MOCVD. The growth conditions and the film thickness ($\sim 520\text{nm}$) of the samples are maintained to be similar for comparison. Mg composition was adjusted by changing the Zn/Mg metalorganic gas-flow ratio. Optical anisotropy in the films is studied using room temperature polarized transmission spectra. A synchronous testing

configuration with a lock-in amplifier and a low-noise transimpedance preamplifier was used to measure the polarized transmission spectra.

Figure 6.1 (a), shows the transmission spectrum of a-plane ZnO films, with light polarization parallel and perpendicular to the in-plane c -axis, respectively. The transmission curve of $\mathbf{E} \perp c$ shows similar shape but a redshift compared with that of $\mathbf{E} \parallel c$. The bandgap energy E_g ($E \parallel c$ -axis) is observed to be $\sim 3.339\text{eV}$, and E_g ($E \perp c$ -axis) is $\sim 3.325\text{eV}$, with the difference in the energies being $\sim 14.34\text{meV}$. This phenomenon can be explained by the different selection rules for A, B and C bands in the valence band structure as well as the presence of in-plane anisotropic strain (discussed in chapter 2). The transition between A (B) valence band and the conduction band is mainly allowed for the $\mathbf{E} \perp c$, while transition between C valence band and the conduction band is mainly allowed for $\mathbf{E} \parallel c$.

In comparison with those of ZnO, the cutoff wavelengths of $\text{Mg}_{0.12}\text{Zn}_{0.88}\text{O}$ film for $\mathbf{E} \perp c$ and $\mathbf{E} \parallel c$ shift to shorter wavelengths, where \mathbf{E} is the electric field component of the incident light as seen in figure 6.1 (b). The corresponding bandgap energies for parallel and perpendicular electric field polarization are E_g ($E \parallel c$ -axis) $\sim 3.4382\text{eV}$ and E_g ($E \perp c$ -axis) $\sim 3.428\text{eV}$. The parallel polarization is again observed to be larger than the perpendicular component by $\sim 9.816\text{meV}$. The difference between the parallel and perpendicular polarization bandgap is lower in case of $\text{Mg}_{0.12}\text{Zn}_{0.88}\text{O}$ as compared to a-plane ZnO films indicating a reduction of overall anisotropy with MgO alloying of ZnO. This is expected due to lattice distortion with Mg alloying, as MgO is cubic rocksalt structure while ZnO is wurtzite structure.

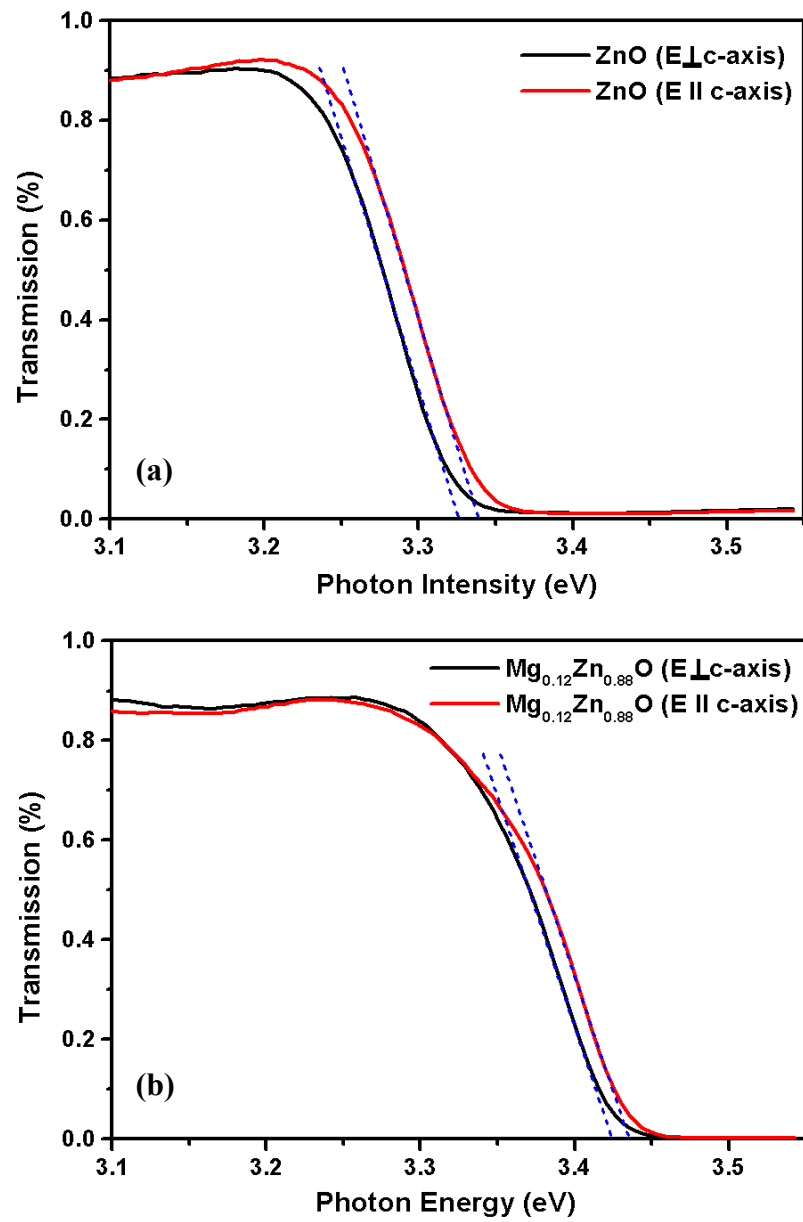


Figure 6.1: Shows the transmission spectrum of a-plane (a) ZnO and (b) $Mg_{0.12}Zn_{0.88}O$ films with light polarization parallel and perpendicular to the c-axis, respectively.

Alloying of ZnO with MgO reduces the c/a ratio from ideal hexagonal structure thus reducing the overall structural anisotropy (reference chapter 4). It has been also observed that the in-plane optical anisotropy dramatically decreases or disappears in textured $\text{Mg}_x\text{Zn}_{1-x}\text{O}$ films *i.e.* films grown without a ZnO buffer.

6.2 ELECTRICAL ANISOTROPY

The availability of anisotropic transport properties can be advantageous or detrimental depending on device structure and application. It can be used to optimize the performance of devices such as Schottky contacts or p-n junction diodes, which exhibit a predominantly a one-dimensional current flow by choosing appropriate in-plane crystal orientation. Further development and understanding of such applications require better understanding of the anisotropy in the electrical properties. In this section we investigate the Hall mobility anisotropy in a-plane $\text{Mg}_x\text{Zn}_{1-x}\text{O}$ films with Mg composition.

The a-plane $\text{Mg}_x\text{Zn}_{1-x}\text{O}$ thin film samples are deposited on r-sapphire substrates by MOCVD. MOCVD growth conditions and film thickness of the samples (~520nm) are maintained constant for comparison. Composition variation in the samples is achieved by varying the Zn/Mg metalorganic gas-flow ratio. In-plane anisotropy in Hall mobility of the samples is characterized using Hall bar patterns on the samples. This work was done in collaboration with Dr. D. C. Look at Wright State University, Ohio.

Figure 6.2, shows Hall mobility measurement (a) for a-plane $\text{Mg}_{0.08}\text{Zn}_{0.92}\text{O}$ films grown on r-sapphire substrates with magnetic field and (b) for a-plane $\text{Mg}_x\text{Zn}_{1-x}\text{O}$ films with Mg composition at magnetic field of 2000G.

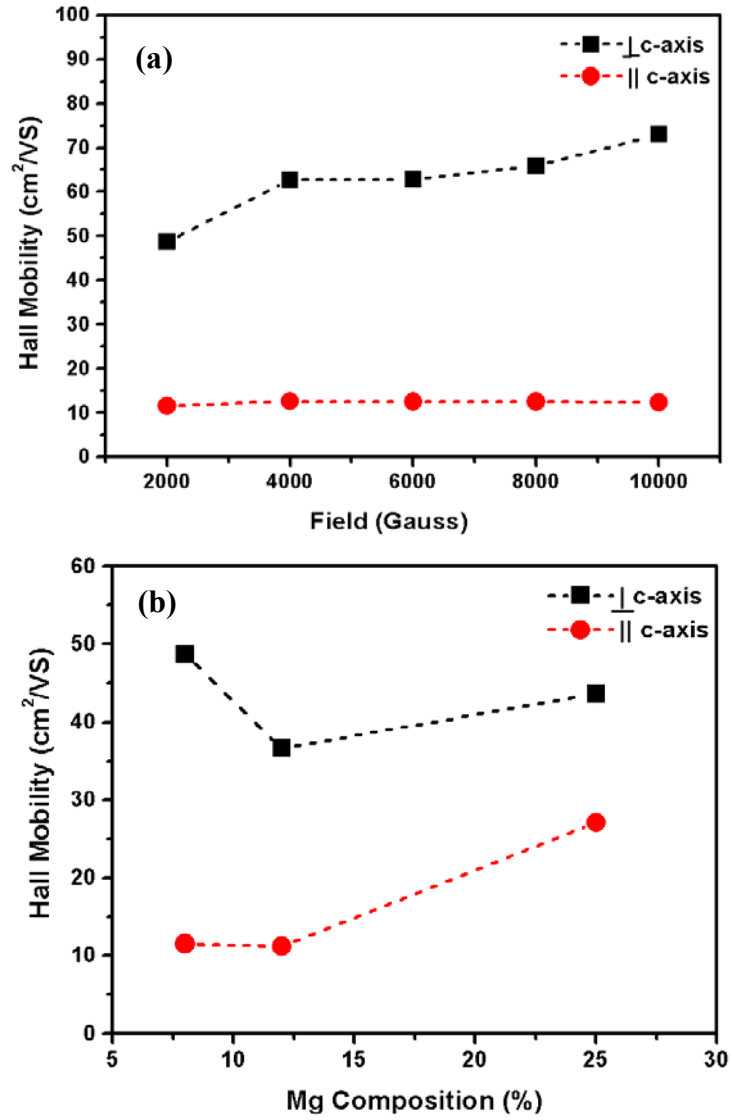


Figure 6.2: Shows Hall mobility measurement (a) for a-plane $\text{Mg}_{0.08}\text{Zn}_{0.92}\text{O}$ films grown on r-sapphire substrates with magnetic field and (b) for a-plane $\text{Mg}_x\text{Zn}_{1-x}\text{O}$ films with Mg composition at magnetic field of 2000G

It is observed that the Hall mobility in the films is anisotropic in-plane along the c-axis [0001] and perpendicular to c-axis (along m-axis [$1\bar{1}00$]). The mobility perpendicular to c-axis is larger than the mobility parallel to c-axis. Earlier, Matsui et. al. observed in-plane anisotropic transport properties in homoepitaxial non-polar ($10\bar{1}0$) ZnO films [103]. It was observed that the Hall mobility along the in-plane c-axis [0001] was larger than the in-plane a-axis [$11\bar{2}0$]. Anisotropy in mobility was attributed to the observed anisotropic surface morphology with needles running parallel to the in-plane c-axis. Temperature dependent mobility measurements indicated that phonon and other scattering mechanisms pre-dominated the band conduction. Higher mobility along the c-axis was attributed to lower scattering cross-section compared to in-plane a-axis. In our case however we observe higher mobility along the in-plane m-axis (analogous to a-axis in case of ($10\bar{1}0$) ZnO films) as compared to in-plane c-axis. Although we observe similar surface morphology anisotropy in a-plane ZnO and $\text{Mg}_x\text{Zn}_{1-x}\text{O}$ films (reference chapter 5), in our case it seems that band conduction dominates. Since, the bandgap perpendicular to in-plane c-axis (along m-axis) is smaller than that parallel to c-axis (reference figure 6.1), the mobility is expected to be larger along m-axis. Higher dislocations density and in-plane strain along the c-axis (reference chapter 4 and chapter 5) compared to in-plane m-axis could also justify higher mobility observed along the m-axis. Strain would play an important role in this case due to large lattice mismatch with the r-sapphire substrate as compared to homoepitaxial films characterized by Matsui et. al.. It is observed that an increase in Mg composition in the a-plane $\text{Mg}_x\text{Zn}_{1-x}\text{O}$ films reduces the mobility anisotropy. The ratio ($\mu_{H \perp} / \mu_{H \parallel}$) decreases from ~ 4.23 for $\text{Mg}_{0.08}\text{Zn}_{0.92}\text{O}$ to ~ 1.61 for $\text{Mg}_{0.25}\text{Zn}_{0.75}\text{O}$. This could be due to different in-plane strain

distribution and lowering of bandgap anisotropy with Mg incorporation (reference figure 6.1).

6.3 ZnO TFT – A FEASIBILITY STUDY

One of the simplest and most efficient ways to study anisotropic transport characteristics is via the fabrication of thin film transistors (TFT). In this section we discuss results on a normally ON – depletion type ZnO based thin film transistor. The key features of a good depletion type device includes high mobility and low carrier concentration. The dependence of mobility and carrier concentration in the thin films is studied with film deposition temperature and oxygen partial pressure.

Figure 6.3 (a) and (b) show the variation of average mobility and carrier concentration in a-plane ZnO films with deposition temperature and oxygen partial pressure in MOCVD, respectively. All the films are grown on r-sapphire substrates with a film thickness ranging from 70 - 90nm. Hall mobility and carrier concentration in the films is monitored using Van der Pauw method. It is observed that an increase in deposition temperature improves the Hall mobility and also the carrier concentration in the films. An increase in the oxygen partial pressure during the growth is observed to reduce the carrier concentration for the entire temperature range. Oxygen partial pressure also significantly affects the mobility. An increase in oxygen flow is observed to increase the mobility for films deposited at low temperatures, however for films deposited at high temperatures the mobility is reduced. For all the samples the carrier concentration is observed to be larger than 10^{17}cm^{-3} . One of the reasons for high carrier concentrations observed could be n-type defects at the ZnO/ r-sapphire interface. Al diffusion across the

ZnO/ r-sapphire interface into ZnO would also increase the carrier concentration, since Al is shallow n-type donor in ZnO [104]. Al diffusion into ZnO to form of Al_2O_3 -ZnO complex at the ZnO/r-sapphire interface has been observed by Gorla et. al. for high temperature annealed ZnO films [105]. An increase in deposition temperature would thus increase the overall n-type carrier concentration in the samples by increasing Al diffusion. Other key effects of increase in deposition temperature include improvement in crystalline quality of the films (reference chapter 3), which would also affect the mobility and carrier concentration. Increase in oxygen partial pressure during growth reduces n-type carrier concentration due to compensation of n-type oxygen vacancies observed for oxide films. Based on the optimized oxygen flow and deposition temperature the TFT device is fabricated on non-polar ZnO thin film deposited on r-sapphire substrate. The ZnO film thickness is designed to be 70nm – 100nm. After the MOCVD deposition of the thin ZnO film, the sample is annealed at $\sim 500^\circ \text{C}$ for 30mins in oxygen ambience to further reduce n-type carrier concentration. A plasma enhanced chemical vapor deposited (PECVD) SiO_2 film is used as the dielectric layer, with thickness $\sim 110\text{nm}$. The thickness of the SiO_2 layer is designed in order to avoid leakage from the dielectric layer. Al metal is used as the gate as well as the source and drain contacts using e-beam evaporation. The fabricated devices were aligned along the two in-plane directions (namely $\parallel c$ -axis and $\perp c$ -axis) in order to measure the anisotropy in the device characteristics. Figure 6.4, shows the schematic of the TFT device. The I-V characteristics of the device are measured as shown in figure 6.5 (a). Figure 6.5 (b) shows anisotropic I_{DS} and g_{m} versus I_{GS} characteristics of the devices aligned along the two in-plane directions.

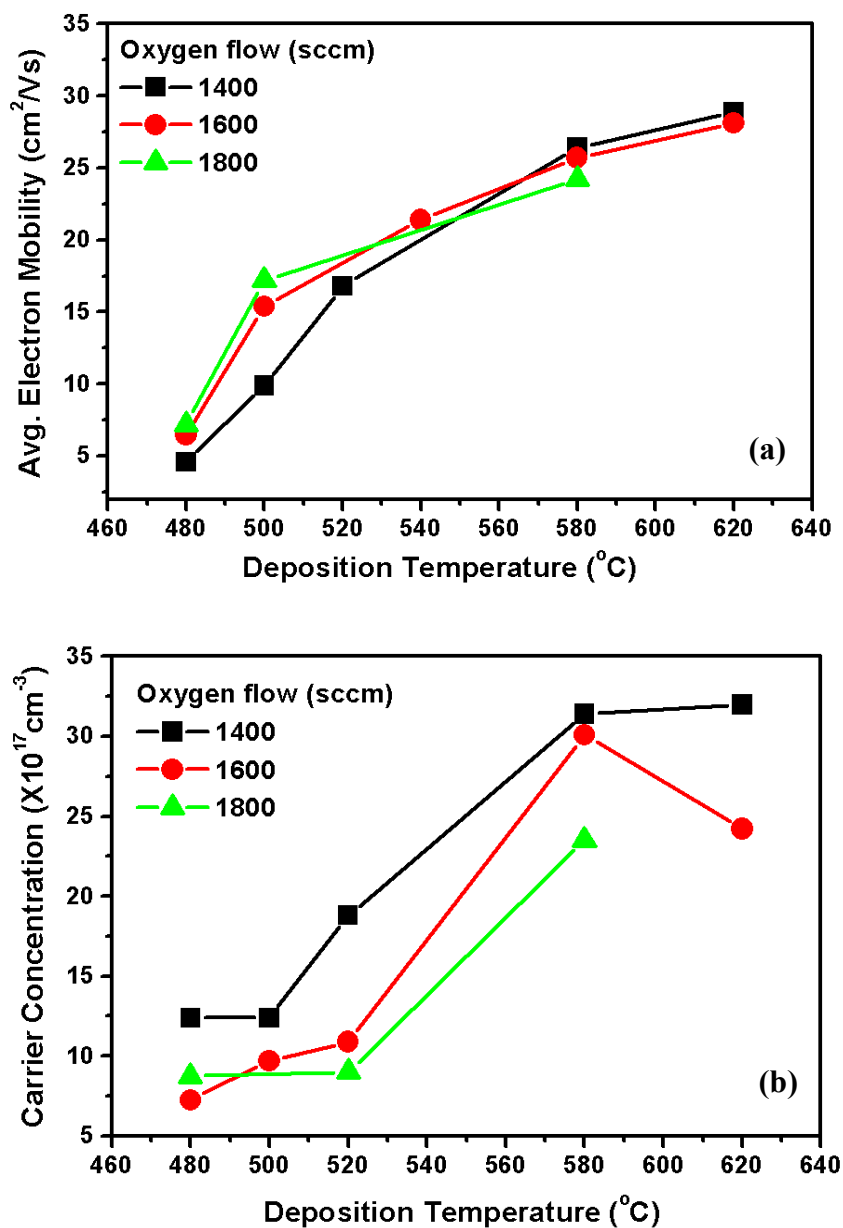


Figure 6.3: (a) and (b) show the variation of average mobility and carrier concentration in a-plane ZnO films with deposition temperature and oxygen partial pressure in MOCVD, respectively

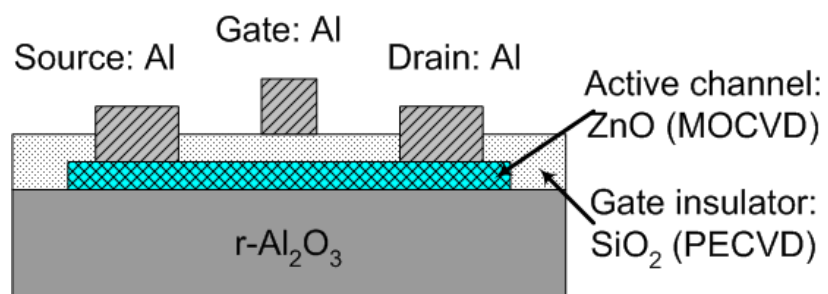


Figure 6.4: Shows the schematic of the ZnO TFT device on r-sapphire

The device parameters extracted from the I-V characteristics listed in table 6.1.

Table 6.1: The extracted device parameters for the two in-plane directions

	 c-axis [0001]	⊥ c-axis [$\bar{1}\bar{1}00$]
V_{th} (V)	-22.8	-25.4
μ_{sat} (cm²/Vs)	28.7	35.5
g_m (mS/mm)	1.0 at V _{gs} = -9.8V	1.09 at V _{gs} = -13.2V
I_{ds} (A)	7.68E-4 (V _{gs} = 0V) 5.3E-13 (V _{gs} = -30V)	8.94E-4 (V _{gs} = 0V) 4.87E-12 (V _{gs} = -30V)
On/Off ratio	1.45×10 ⁹	1.84×10 ⁸

It is observed the devices aligned along the two in-plane directions show anisotropic characteristics. The threshold voltage required to completely deplete the channel is large. Threshold voltage is affected due to factors such as defects at the interface between the ZnO / r-sapphire, large carrier concentration in ZnO films, the dielectric layer thickness, trapped charges at the dielectric layer (SiO₂)/film (ZnO) interface etc. The device shows high On/Off ratio in both the directions, however the field-effect mobility in both directions is low. This is possibly due to low hall mobility in the thin film ZnO deposited on r-sapphire. Highest mobility reported for CVD deposited ZnO films (thickness ~1 - 2μm) is about 125cm²/Vs. Low mobility of the films could be due to smaller film thickness (70nm – 100nm) of the ZnO films. The field effect mobility is higher perpendicular to in-plane c-axis as compared to parallel to c-axis.

Summary

In summary we characterized and studied in-plane anisotropy in optical and electrical properties of a-plane ZnO and Mg_xZn_{1-x}O films on r-sapphire. Mechanism involved with mobility and carrier concentration variation with film deposition conditions as well as composition requires detailed study and analysis.

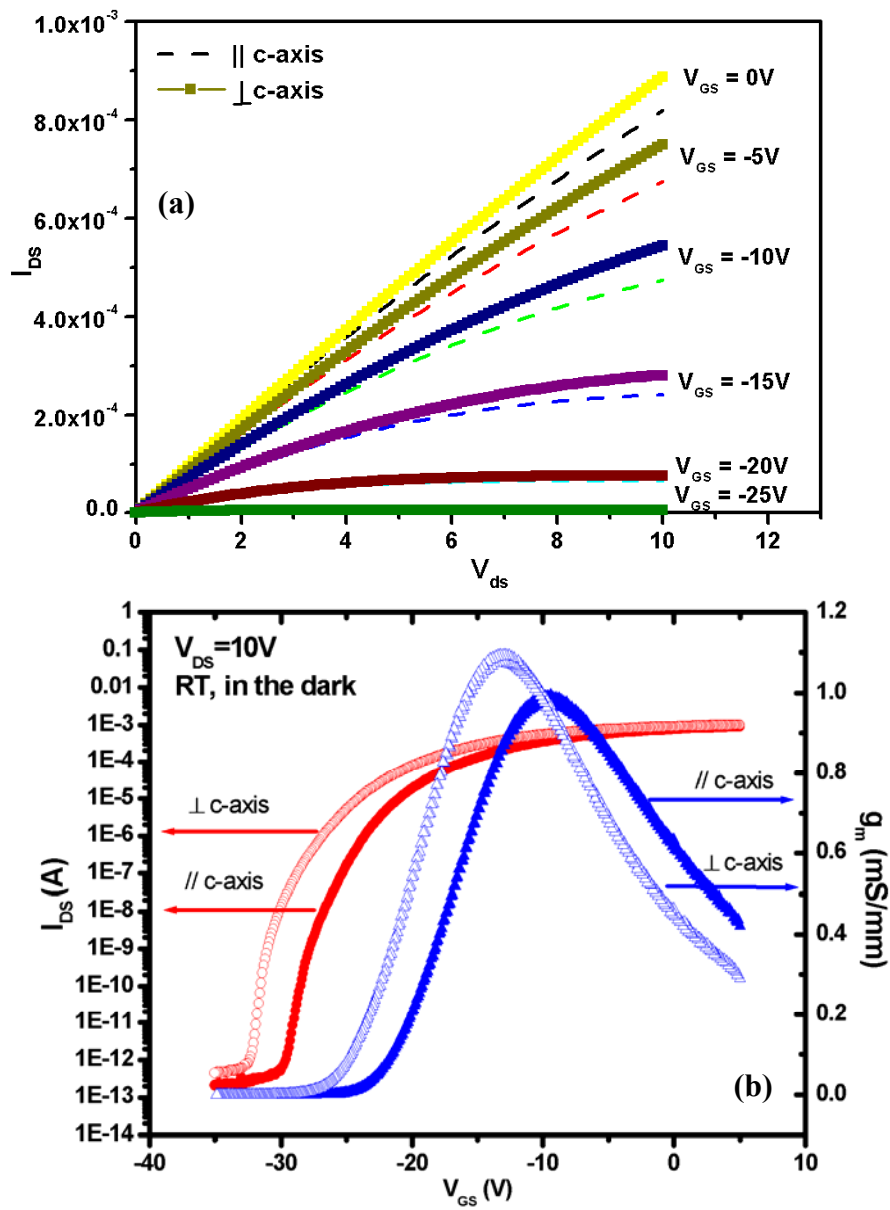


Figure 6.5 (a) shows the anisotropic I_{DS} - V_{DS} characteristics, (b) shows anisotropic I_{DS} and g_m versus I_{GS} characteristics of the devices aligned along the two in-plane directions.

A prototype TFT on a-plane ZnO thin films was demonstrated. Optimization of TFT device parameters requires in depth analysis of dielectric layer design, study of the film/ substrate interface etc.

CHAPTER 7: CONCLUSIONS AND SUGGESTIONS FOR FUTURE WORK

Conclusions

Anisotropy in in-plane structural, optical and electrical properties in non-polar ZnO films can be both advantageous as well as disadvantageous. In-plane optical and electrical anisotropy can be used for novel device applications, while in-plane structural anisotropy may present challenges in thin film growth and successful realization of optoelectronic devices. In this work we optimize the MOCVD growth of a-plane $\text{Mg}_x\text{Zn}_{1-x}\text{O}$ thin films on r-sapphire substrates and study the in-plane anisotropy in structural, optical and electrical properties of these thin films.

Metalorganic chemical vapor deposition technique (MOCVD) was successfully used to optimize the growth epitaxial a-plane ZnO and $\text{Mg}_x\text{Zn}_{1-x}\text{O}$ thin films on r-sapphire substrates. It was demonstrated that Mg is substitutional to Zn in the wurtzite ZnO lattice. Change in the optical transmission edge indicated an increase in direct bandgap with Mg composition increase in the a-plane films. Optimization of the crystal properties was investigated by variation in deposition temperature for a-plane ZnO films. It was observed that increase in deposition temperature improved the overall crystallinity and also the mosaic in the films. Based on this observation, the optimized MOCVD deposition temperature was found in range 500 – 560°C for a-plane $\text{Mg}_x\text{Zn}_{1-x}\text{O}$ films on r-sapphire, with typical growth rate of ~500nm/hr. The PL properties of the a-plane films deposited using the optimized conditions was investigated. It was observed that the films showed good optical properties, with the absence of deep level emissions. A blue shift in the PL peaks was observed with increase in Mg composition in the films, indicating an increase in the direct bandgap. The optical properties of $\text{Mg}_x\text{Zn}_{1-x}\text{O}$ films can be tuned by

adjusting the Mg composition, providing energy bandgap engineering. $\text{Mg}_x\text{Zn}_{1-x}\text{O}$ ($0 < x < 0.33$) films and heterostructures with ZnO are thus suitable for producing devices that operating in the ultraviolet wavelengths regime. The FWHM of the PL peaks was found to increase from $\sim 95\text{meV}$ for pure ZnO films to $\sim 133\text{meV}$ for $\text{Mg}_{0.12}\text{Zn}_{0.88}\text{O}$ films.

In-plane structural, optical and electrical anisotropy in the a-plane films was characterized and analyzed. In-plane strain anisotropy in the films was characterized using XRD method. A synchrotron radiation source was used for precision in measurements. Precise lattice parameters were obtained by lattice refinement. It was observed that the in-plane strain in the epitaxial films cause orthorhombic distortion in the wurtzite lattice of a-plane $\text{Mg}_x\text{Zn}_{1-x}\text{O}$ films grown on r-sapphire substrates. The in-plane strain was found to be anisotropic along and perpendicular to c-axis. The strain was tensile along the in-plane m-axis, while being compressive along the in-plane c-axis. The out-of-plane strain was found to be tensile. For pure ZnO films the strain relaxed with increase in film thickness. Strain was found to increase both along the in-plane directions and the out-of-plane direction with increase in Mg composition in the films. Qualitative analysis of the films using reciprocal space maps (RSMs) indicated low density of weak and strong defects in the films. However, the mosaic was found to be larger in case of $\text{Mg}_{0.15}\text{Zn}_{0.85}\text{O}$ films as compared to pure ZnO films. Structural anisotropy study also included detailed analysis of the surface and interface morphology of the a-plane films. The surface of a-plane films showed anisotropic morphology with needles running parallel to the crystallographic c-axis of the films. The effect of substrate miscut and film deposition temperature on the morphology anisotropy was studied in detail. The design of proper substrate miscut is important to control the morphology fluctuations in the thin

films. The in-plane optical anisotropy is found to be result of the in-plane structural anisotropy in the $\text{Mg}_x\text{Zn}_{1-x}\text{O}$ film. In-plane optical anisotropy is of strong interest for applications in the polarization-sensitive optoelectronic devices. Such anisotropic behavior can be exploited for novel device applications, such as high-contrast UV modulators. In-plane electrical anisotropy was found to be a result of both structural as well as in-plane optical anisotropy in the films. A prototype thin film transistor was developed with anisotropic I-V characteristics.

Suggestions for future work

Even now the biggest challenges in the area of ZnO based semiconductor is successful realization of stable and reliable p-type doping and energy band engineering for the fabrication of heterostructures and quantum wells. Significant effort have been devoted towards development of ZnO based heterostructures. This work is focussed in improvement of these heterostructures, and paving way for realization of anisotropy based novel devices.

In this dissertation we have characterized and studied anisotropy in structural, optical and electrical properties of non-polar a-plane $\text{Mg}_x\text{Zn}_{1-x}\text{O}$ film grown on r-sapphire substrates by MOCVD. The recommendations for future research and development based on the present work are:

1. More detailed study of the anisotropic surface morphology with variations in MOCVD growth. Control of surface and interface morphology by use buffer or transition layers for development of non-polar heterostructures and QWs.

2. Detailed understanding of the underlying mechanism of the observed morphology anisotropy.
3. Detailed characterization of the defects in the non-polar films using transmission electron microscopy and other spectroscopic techniques.
4. Detailed study of the transport anisotropy in correlation with strain, surface morphology and electronic properties for development of a-plane ZnO and $\text{Mg}_x\text{Zn}_{1-x}\text{O}$ thin film based electronic devices.
5. Fabricate single and double heterostructures of ZnO/ $\text{Mg}_x\text{Zn}_{1-x}\text{O}$ films and multi-quantum wells (MQW) on r-sapphire substrates and investigate the structural quality using HRXRD and nature of the interface using HRTEM.
6. Study the optical properties of ZnO/ $\text{Mg}_x\text{Zn}_{1-x}\text{O}$ heterostructures and MQWs on r-sapphire substrates using room temperature and low temperature photoluminescence (PL) techniques and correlate it with microstructural data.
7. Correlation of strain with the optical properties, piezoelectric and spontaneous polarization fields in non-polar thin film heterostructures and quantum wells.

REFERENCES

1. M. Wraback H. Shen, S. Liang, C. R. Gorla, Y. Lu, “*A High Contrast, Ultrafast Optically Addressed Ultraviolet Light Modulator Based upon Optical Anisotropy in ZnO Films Grown on r-plane Sapphire*”, Appl. Phys. Lett., 74 (4), p. 507 (1999)
2. Y. Wu, H. Yan, M. Huang, B. Messer, J. H. Song, and P. Yang, “*Inorganic Semiconductor Nanowires: Rational Growth, Assembly, and Novel Properties*”, European Journal of Chemistry, 8(6), p. 1260 (2002)
3. T. Komaru, S. Shimizu, M. Kanbe, Y. Maeda, T. Kamiya, C. M. Fortmann, I. Shimizu, “*Optimization of Transparent Conductive Oxide for Improved Resistance to Reactive and/or High Temperature Optoelectronic Device Processing*”, Jpn. J. Appl. Phys., Part 1, 38, 5796 (1999)
4. D. M. Bagnall Y. F. Chen, Z. Zhu, T. Yao, M. Y. Shen, and T. Goto,” *High temperature excitonic stimulated emission from ZnO epitaxial layers*”, Appl. Phys. Lett., 73 (8) p. 1038 (1998)
5. Z. K. Tang G. K. L Wong, P. Yu, M. Kawasaki, A. Ohtomo, H. Koinuma, and Y. Segawa, “*Room-temperature ultraviolet laser emission from self-assembled ZnO microcrystallite thin films*”, Appl. Phys. Lett., 72 (25) p. 3270 (1998)
6. F. Hamdani, M. Yeadon, D. J. Smith, H. Tang, W. Kim, A. Salvador, A. E. Botchkarev, J. M. Gibson, A. Y. Polyakov, M. Skowronski, and H. Morkoc, “*Microstructure and optical properties of epitaxial GaN on ZnO (0001) grown by reactive molecular beam epitaxy*”, Journal of Applied Physics, 83(2) p. 983 (1998)
7. D. C. Look, “*Recent advances in ZnO materials and devices*”, Material Sci. and Eng. B, 80 (1-3), p. 383 (2001)
8. Y. Oumi, H. Takaba, S. S. C. Ammal, M. Kubo, K. Teraishi, A. Miyamoto, M. Kawasaki, M. Yoshimoto, and H. Koinuma, “*Periodic boundary quantum chemical study of ZnO ultra-violet laser emitting materials*”, Japanese Journal of Applied Physics, Part 1, 38(4B), p. 2603, 1999
9. A. Ohtomo, M. Kawasaki, T. Koida, K. Masubuchi, Y. Sakurai, Y. Yoshida, T. Yasuda, Y. Segawa, and H. Koinuma, “*Mg_xZn_{1-x}O as a II-VI widegap semiconductor alloy*”, Appl. Phys. Lett., 72(19), p. 2466 (1998)
10. S. Muthukumar, J. Zhong, Y. Chen, T. Siegrist and Y. Lu, “*Growth and structural analysis of metalorganic chemical vapor deposited (11 $\bar{2}$ 0) Mg_xZn_{1-x}O (0<x<0.33) films on (01 $\bar{1}$ 2) R-plane Al₂O₃ substrates*”, Appl. Phys. Lett., 82 (5), pp. 742, (2003)
11. S. Muthukumar, Y. Chen, J. Zhong, F. Cosandey, Y. Lu, and T. Siegrist, “*Metalorganic chemical vapor deposition and characterizations of epitaxial*

- $Mg_xZn_{1-x}O$ ($0 \leq x \leq 0.33$) films on *r*-sapphire substrates”, Journal of Crystal Growth, 261 (2-3), pp. 316 (2004)
12. C. J. Kao, Yong Wook Kwon, Y. W. Heo, D. P. Norton, F. Ren, G. C. Chi and S. J. Pearton, “*Comparison of ZnO metal–oxide–semiconductor field effect transistor and metal–semiconductor field effect transistor structures grown on sapphire by pulsed laser deposition*”, Journal of Vacuum Science & Technology B, 23 (3), pp. 1024-1028 (2005)
 13. K. Koike, I. Nakashima, K. Hashimoto, S. Sasa, M. Inoue, and M. Yano “*Characteristics of a $Zn_{0.7}Mg_{0.3}O/ZnO$ heterostructure field-effect transistor grown on sapphire substrate by molecular-beam epitaxy*”, Appl. Phys. Lett. 87, 112106 (2005)
 14. Chennupati Jagadish and S. J. Pearton, “*Zinc oxide thin films*”, ISBN 0080447228, Elsevier 2006
 15. V. G. Litovchenko, V. N. Babentsov, D. V. Korbutyak, and M. T. Ivanchuki, “*Multiparticle exciton complexes in semiconductors with a large exciton binding energy in (ZnO)*”, JETP Letters, 30(9), p. 544 (1979)
 16. J. F. Muth, A. K. Sharma, S. Oktyabrsky, J. Narayan, and R. M. Kolbas, “*Excitonic structure and absorption coefficient measurements of ZnO single crystal epitaxial films deposited by pulsed laser deposition*”, Journal of Applied Physics, 85(11), p. 7884 (1999)
 17. A. Ohtomo, M. Kawasaki, I. Ohkubo, H. Koinuma, T. Yasuda, and Y. Segawa, “*Structure and optical properties of $ZnO/Mg_{0.2}Zn_{0.8}O$ superlattices*”, Appl. Phys. Letts, 75(7), p. 980 (1999)
 18. A. Ohtomo, K. Tamura, M. Kawasaki, T. Makino, Y. Segawa, Z. K. Tang, G. K. L. Wong, Y. Matsumoto, and H. Koinuma, “*Room-temperature stimulated emission of excitons in $ZnO/(Mg, Zn)O$ superlattices*”, Appl. Phys. Letts, 77(14), p. 2204 (2000)
 19. C. H. Chia, T. Makino, and Y. Segawa, M. Kawasaki, A. Ohtomo, K. Tamura, and H. Koinuma, “*Well-width dependence of radiative and nonradiative recombination times in $ZnO/Mg_{0.12}Zn_{0.88}O$ multiple quantum wells*”, Journal of Applied Physics, 90 (7), p. 3650 (2001)
 20. S-H. Park and S-L. Chuang “*Spontaneous polarization effects in wurtzite $GaN/AlGaN$ quantum wells and comparison with experiment*”, Appl. Phys. Lett. 76, 1981 (2000)
 21. P. Misra, , Y. J. Sun, O. Brandt, and H. T. Grahn, “*Polarization filtering by nonpolar M -plane GaN films on $LiAlO_2$* ”, Journal of Applied Physics, 96, 7029–7035 (2004)

22. C. R. Gorla, W. E. Mayo, S. Liang and Y. Lu, “*Structural, optical, and surface acoustic wave properties of epitaxial ZnO films grown on (01 $\bar{1}$ 2) sapphire by metalorganic chemical vapor deposition*”, Journal of Applied Physics, 87 (8), pp. 3736 (2000)
23. G. Saraf, J. Zhong, O. Dulub, U. Diebold, T. Siegrist and Y. Lu, “*Surface and Interface Properties of MOCVD Grown a-plane Mg_xZn_{1-x}O (0 ≤ x ≤ 0.3) Films*”, Journal of Electronic Materials, 36 (4), pp. 446-451 (2007)
24. W-J. Li, E-W. Shi, W-Z. Zhong, Z-W. Yin, “*Growth mechanism and growth habit of oxide crystals*”, Journal of Crystal Growth, 203 (1-2), pp. 186-196 (1999)
25. W. B. Pearson, “*A Handbook of Lattice Spacings and Structures of Metals and Alloys*” Vol. 2 (1967), New York: Pergamon Press
26. P. Mishra, Y. J. Sun, O. Brandt, H. T. Grahn, “*Angular dependence of the in-plane polarization anisotropy in the absorption coefficient of strained M-plane GaN films on γ -LiAlO₂*”, Physica Status Solidi (b), 240 (2), pp. 293–296 (2003)
27. A. Ohtomo, R. Shiroki, I. Ohkubo, H. Koinuma, and M. Kawasaki, “*Thermal stability of supersaturated Mg_xZn_{1-x}O alloy films and Mg_xZn_{1-x}O/ZnO heterointerfaces*”, Appl. Phys. Letts, 75(26): p. 4088 (1999)
28. Olga Dulub, Lynn A. Boatner, Ulrike Diebold, “*STM study of the geometric and electronic structure of ZnO (0001)-Zn, (000-1)-O, (10-10), and (11-20) surfaces*”, Surface Science, 519, pp. 201–217 (2002)
29. A. Mills, *Metal-organic processing leads the pack*. III-Vs Review, 15 (8), pp. 46-48 (2002)
30. R. L. Moon, *MOVPE: Is there any other technology for optoelectronics?* Journal of Crystal Growth, 170 (1-4), pp. 1-10 (1997)
31. A. G. Thompson, *MOCVD technology for semiconductors*. Materials Letters, 30 (4), pp. 255-263 (1997)
32. M. L. Timmons, P. K. Chiang, and S. V. Hattangady, *An alternative Mg precursor for p-type doping of MOVPE grown material*. Journal of Crystal Growth, 77(1-3), pp. 37-41 (1986)
33. S. Muthukumar, “*MOCVD growth and characterizations of Mg_xZn_{1-x}O films on r-sapphire*”, Ph.D. thesis, Rutgers University (2003)
34. C. R. Gorla, “*Properties of ZnO thin films grown on r-sapphire by MOCVD*”, Ph.D. Thesis, Rutgers University (1999)

35. J. Z. Pérez and V. M. Sanjosé, M. Lorenz, G. Benndorf, S. Heitsch, D. Spemann, and M. Grundmann, “*Structural characterization of a-plane $\text{Zn}_{1-x}\text{Cd}_x\text{O}$ ($0 \leq x \leq 0.085$) thin films grown by metal-organic vapor phase epitaxy*”, Journal of Applied Physics, 99, 023514 (2006)
36. Olga Dulub, Ulrike Diebold, and G. Kresse, “*Novel Stabilization Mechanism on Polar Surfaces: $\text{ZnO}(0001)\text{-Zn}$* ”, Physical Review Letters, 90, 016102 (2003)
37. U. Diebold, L. Vogel Koplitz, O. Dulub, “*Atomic-Scale Properties of Low-Index ZnO Surfaces*”, Applied Surface Science 237 (1-4), pp. 336-342 (2004)
38. X. Q. Gong, A. Selloni, M. Batzill, and U. Diebold, “*Steps on TiO_2 Anatase (101)*” Nature Materials 5 (8), pp. 665-70 (2006)
39. R. L. Headrick, J.-M. Baribeau and Y. E. Strausser, “*Anisotropic roughness in Ge/Si superlattices*”, Appl. Phys. Lett., 66 (1), pp. 96-98 (1995)
40. S. B. Samavedam and E. A. Fitzgerald, “*Novel dislocation structure and surface morphology effects in relaxed $\text{Ge/Si-Ge}(\text{graded})/\text{Si}$ structures*”, Journal of Applied Physics, 81 (7), pp. 3108-3116 (1997)
41. Y. H. Phang, C. Teichert, L. J. Peticolos, J. C. Bean, E. Kasper and M. G. Lagally, “*Correlated-interfacial-roughness anisotropy in $\text{Si}_{1-x}\text{Ge}_x/\text{Si}$ superlattices*”, Physical Reviews B, 50 (19), (1994)
42. T. Someya, K. Hoshino and Y. Arakawa, “*Misorientation-angle dependence of GaN layers grown on a-plane sapphire substrates by metalorganic chemical vapor deposition*”, Appl. Phys. Lett., 79 (13), pp.1992-1994 (2001)
43. J. Pernot, M. Rudziński, P. R. Hageman, P. K. Larsen and E. Bustarret, “*Strain relaxation in GaN grown on vicinal 4H-SiC (0001) substrates*”, Journal of Applied Physics, 101, 033536 (2007)
44. X. Ni, Ü. Özgür, Z. Liliental-Weber, H. O. Everitt and H. Morkoc, “*Epitaxial lateral overgrowth of a-plane GaN by metalorganic chemical vapor deposition*”, Journal of Applied Physics, 102, 053506 (2007)
45. T. Kawashima, T. Nagai, D. Iida, A. Miura, Y. Okadome, Y. Tsuchiya, M. Iwaya, S. Kamiyama, H. Amano and I. Akasaki, “*Characterization of low-defect-density a-plane and m-plane GaN and fabrication of a-plane and m-plane LEDs*”, Proc. of SPIE Vol. 6468, 64680S, (2007)
46. F. Vigue, P. Vennegues, S. Vezian, M. Laugt, and J. P. Faurie, “*Defect characterization in ZnO layers grown by plasma-enhanced molecular beam epitaxy on (0001) sapphire substrates*”, Appl. Phys. Letts, 79 (2), pp. 194 (2001)

47. D. Gerthsen and D. Litvinov, Th. Gruber, C. Kirchner, and A. Waag, “*Origin and consequences of a high stacking fault density in epitaxial ZnO layers*”, Appl. Phys. Letts, 81 (3972), 2002
48. J. Narayan, K. Dovidenko, A. K. Sharma, and S. Oktyabrsky, “Defects and interfaces in epitaxial ZnO/ α -Al₂O₃ and AlN/ZnO/ α -Al₂O₃ heterostructures”, Journal of Applied Physics, 84 (5), pp. 2597-2601 (1998)
49. P. Bhattacharya, “*Semiconductor Optoelectronic Devices*”, 2 ed., New Jersey: Prentice-Hall, Inc., 114 (120), pp. 143 – 147 (1997)
50. D. K. Kolb and H. J. Schulz, “*Current Topics in Material Science*”, ed. E. Kaldis. Vol. 7., Amsterdam: North-Holland (1981)
51. E. Tomzig and R. Helbig, “*Band-edge emission in ZnO*”, *Journal of Luminescence*”, 14 (5-6), pp. 403 – 415 (1976)
52. S. M. Sze, “*Semiconductor Devices-Physics and Technology*”, 2 ed., New York: John Wiley & Sons, Inc. (2001)
53. W. R. L. Lambrecht, Anna V. Rodina, Sukit Limpijumnong, B. Segall, and Bruno K. Meyer, “*Valence-band ordering and magneto-optic exciton fine structure in ZnO*”, Physical Reviews B, 65, 075207 (2002)
54. S. Limpijumnong and W. R. L. Lambrecht, “*Theoretical study of the relative stability of wurtzite and rocksalt phases in MgO and GaN*”, Physical Review B, 63, 104103 (2001)
55. G. Coli and K. K. Bajaj, “*Excitonic transitions in ZnO/MgZnO quantum well. Heterostructures*”, Appl. Phys. Letts., 78 (19), pp. 2861-2863 (2001)
56. S. Masuda, K. Kitamura, Y. Okumura, S. Miyatake, H. Tabata, and T. Kawai, “*Transparent thin film transistors using ZnO as an active channel layer and their electrical properties*”, Journal of Applied Physics, 93 (3), pp. 1624 (2003)
57. F. M. Hossain, J. Nishii, S. Takagi, A. Ohtomo, and T. Fukumura, H. Fujioka, H. Ohno, H. Koinuma, M. Kawasaki, “*Modeling and simulation of polycrystalline ZnO thin-film transistors*”, Journal of Applied Physics, 94 (12), pp. 7768 (2003)
58. E. M. C. Fortunato, P. M. C. Barquinha, A. C. M. B. G. Pimentel, A. M. F. Gonçalves, A. J. S. Marques, L. M. N. Pereira, R. F. P. Martins, “*Fully Transparent ZnO Thin-Film Transistor Produced at Room Temperature*”, Advanced Materials., 17 (5), pp. 590 (2005)

59. H. Yano, T. Hirao, T. Kimoto, H. Matsunami, K. Asano, and Y. Sugawara, “*High channel mobility in inversion layers of 4H-SiC MOSFETs by utilizing (11-20) face*”, IEEE Elect. Dev. Lett., 20 (12), pp. 611-613 (1999)
60. J. N. Shenoy, J.A. Cooper, and M.R. Melloch, “*High-Voltage Double-Implanted Power MOSFETs in 6H-SiC*”, IEEE Elect. Dev. Lett., 18 (3), pp. 93-95 (1997)
61. J. E. Chung, J. Chen, M. Levi, P-K. Ko, and C. Hu, “The effects of off-axis substrate orientation on MOSFET characteristics”, International Elect. Dev. Meeting, pp. 633 (1989)
62. H. Irie, K. Kita, K. Kyuno and A. Toriwani, “*In-Plane Mobility Anisotropy and Universality Under Uni-axial Strains in n- and p-MOS Inversion Layers on (100), (110), and (111) Si*”, International Elect. Dev. Meeting, pp. 225 (2004)
63. R. W. Keyes, “*High-Mobility FET in Strained Silicon*”, IEEE Trans. on Elect. Dev., 33 (6), pp. 863 (1986)
64. J. Y. Lee, S. Roth, and Y. W. Park, “*Anisotropic field effect mobility in single crystal pentacene*”, Appl. Phys. Lett., 88, 252106 (2006)
65. L. Kinder, J. Kanicki, P. Petroff, “*Structural ordering and enhanced carrier mobility in organic polymer thin film transistors*”, Synthetic Metals, 146, pp. 181–185 (2004)
66. D. Reuter, M. Versen, M. D. Schneider and A. D. Wieck, “*Increased mobility anisotropy in selectively doped $Al_xGa_{1-x}As/GaAs$ heterostructures with high electron densities*”, Journal of Applied Physics, 88 (1), pp. 321-325 (2000)
67. L. Chernyak, A. Osinsky, V. N. Fuflyigin, J. W. Graff, and E. F. Schubert, “*Minority Electron Transport Anisotropy in P-Type $Al_xGa_{1-x}N/GaN$ Superlattices*”, IEEE Trans. on Elect. Dev., 48 (3), pp. 433 (2001)
68. E. R. Segnit and A. E. Holland, “*The System $MgO-ZnO-SiO_2$* ”, Journal of American Ceramic Society, 48 (8), pp. 412 (1965)
69. S. Schmitt-Rink, D. S. Chemla, and D. A. B. Miller, “*Linear and nonlinear optical properties of semiconductor quantum wells*”, Advances in Physics, 38 (2), pp. 89-188 (1989)
70. P. Prete R. Cingolani, D. Greco, P. V. Giugno, M. Lomascolo, R. Rinaldi, and L. Calcagnile L. Vanzetti, L. Sorba, and A. Franciosi, “*Exciton spectroscopy in $Zn_{1-x}Cd_xSe/ZnSe$ quantum wells*”, Physical Review B, 51 (8-15), pp. 5176-5183 (1995)
71. N. T. Pelekanos, J. Ding, M. Hagerott, A. V. Nurmikko, H. Luo, N. Samarth, and J. K. Furdyna, “*Quasi-two-dimensional excitons in $(Zn,Cd)Se/ZnSe$ quantum wells: Reduced exciton-LO-phonon coupling due to confinement effects*”, Physical Review B, 45 (11-15), pp. 6037-6042 (1992)

72. H. D. Sun, T. Makino, Y. Segawa, M. Kawasaki, A. Ohtomo, K. Tamura, and H. Koinuma, “*Enhancement of exciton binding energies in ZnO/ZnMgO multiquantum wells*”, Journal of Applied Physics, 91 (4), pp. 1993-1997 (2002)
73. T. Makino, K. Tamura, C. H. Chia, Y. Segawa, M. Kawasaki, A. Ohtomo, and H. Koinuma, “*Size dependence of exciton–longitudinal-optical-phonon coupling in ZnO/Mg_{0.27}Zn_{0.73}O quantum wells*”, Physical Review B, 66, pp. 233305-233307 (2002)
74. H. D. Sun, T. Makino, Y. Segawa, M. Kawasaki, A. Ohtomo, K. Tamura, and H. Koinuma, “*Biexciton emission from ZnO/Zn_{0.74}Mg_{0.26}O multiquantum wells*”, Applied Physics Letters, 78 (22), pp. 3385-3387 (2001)
75. T. Makino, K. Tamura, C. H. Chia, Y. Segawa, M. Kawasaki, A. Ohtomo, and H. Koinuma, “*Radiative recombination of electron–hole pairs spatially separated due to quantum-confined Stark and Franz–Keldish effects in ZnO/Mg_{0.27}Zn_{0.73}O quantum wells*”, Applied Physics Letters, 81 (13), pp. 2355-2357 (2002)
76. H. D. Sun, Y. Segawa, M. Kawasaki, A. Ohtomo, K. Tamura, and H. Koinuma, “*Phonon replicas in ZnO/ZnMgO multiquantum wells*”, Journal of Applied Physics, 91 (10), pp. 6457-6460 (2002)
77. C. H. Chia, T. Makino, Y. Segawa, M. Kawasaki, A. Ohtomo, K. Tamura, and H. Koinuma, “*Well-width dependence of radiative and nonradiative recombination times in ZnO/Mg_{0.12}Zn_{0.88}O multiple quantum wells*”, Journal of Applied Physics, 90 (7), pp. 3650-3652 (2001)
78. T. Makino, C. H. Chia, N. T. Tuan, Y. Segawa, M. Kawasaki, A. Ohtomo, K. Tamura, and H. Koinuma, “*Radiative and nonradiative recombination processes in lattice-matched (Cd,Zn)O/(Mg,Zn)O multiquantum wells*”, Applied Physics Letters, 77 (11), pp. 1632-1634 (2000)
79. H. D. Sun, T. Makino, N. T. Tuan, Y. Segawa, M. Kawasaki, A. Ohtomo, K. Tamura, and H. Koinuma, “*Temperature dependence of excitonic absorption spectra in ZnO/Zn_{0.88}Mg_{0.12}O multiquantum wells grown on lattice-matched substrates*”, Applied Physics Letters, 78 (17), pp. 2464-2466 (2001)
80. T. Makino, Y. Segawa, M. Kawasaki, A. Ohtomo, R. Shiroki, K. Tamura, T. Yasuda, and H. Koinuma, “*Band gap engineering based on Mg_xZn_{1-x}O and Cd_yZn_{1-y}O ternary alloy films*”, Applied Physics Letters, 78 (9), pp. 1237-1239 (2001)
81. T. Makino, K. Tamura, C. H. Chia, Y. Segawa, M. Kawasaki, A. Ohtomo, and H. Koinuma, “*Effect of MgZnO-layer capping on optical properties of ZnO epitaxial layers*”, Applied Physics Letters, 81 (12), pp. 2172-2174 (2002)

82. T. H. Yu and K. F. Brennan, "*Theoretical Study of a GaN-AlGaN High Electron Mobility Transistor Including a Nonlinear Polarization Model*", IEEE Trans. on Elect. Dev, 50 (2), pp. 315-232 (2003)
83. Nicola A. Hill and Umesh Waghmare, "*First-principles study of strain-electronic interplay in ZnO: Stress and temperature dependence of the piezoelectric constants*", Phys. Rev. B 62 (13), pp. 8802-8810 (2000)
84. Y. Kanke, H. Shigematsu, K. Kato and K-I. Ohsima, "*Space-Group Determination of the Orthorhombic Form of NaV₆O₁₁*", J. Appl. Cryst., 28, pp. 599-603 (1995)
85. T. Nakamura, H. Matsushashi and Y. Nagatomo, "*Silicon on Sapphire (SOS) Device Technology*", Oki Technical Review, 71 (4), Issue 200 (2004)
86. W. R. L. Lambrecht, S. Limpijumnong, and B. Segall, "*Theoretical study of ZnO and related Mg_xZn_{1-x}O alloy band structures*", MRS Internet Journal of Nitride Semiconductor Research, 4S1, G6.8 (1999)
87. L. B. Freund and S. Suresh, "*Thin Film Materials: Stress, Defect Formation, and Surface Evolution*", Cambridge University Press, ISBN 0521822815 (2003)
88. C. Julian Chen, "*Introduction to Scanning Tunneling Microscopy*", Oxford University Press New York (1993)
89. David Vanderbilt and L. K. Wickham, "*Elastic Relaxation Energies of Coherent Germanium Islands on Silicon*", *Evolution of Thin-Film and Surface Microstructure* (MRS Proceedings Volume 202)
90. Robert D. Meade and David Vanderbilt, "*Adatoms on Si (111) and Ge (111) Surfaces*", Phys. Rev. B 40, 3905 (1989)
91. David Vanderbilt, "*Model for the Energetics of Si and Ge (111) Surfaces*", Phys. Rev. B 36 (Rapid Communications), 6209 (1987)
92. M. A. Van Hove, W. H. Weinberg and C. M. Chan, "*Low-Energy Electron Diffraction*", Springer Verlag, 1986
93. A. D. L. Humphris, M. J. Miles, J. K. Hobbs, "*A mechanical microscope: High-speed atomic force microscopy*", Applied Physics Letters, 86, 034106 (2005)
94. T. B. Hur, Y. H. Hwang, I. J. Lee and H. K. Kim, "*Strain effects in ZnO thin films and nanoparticles*", Journal of Applied Physics, 99, 064308 (2006)
95. L. D. Doucette, M. Pereira da Cunha and R. J. Lad, "*Precise orientation of single crystals by a simple x-ray diffraction rocking curve method*", Review of Scientific Instruments, 76, 036106 (2005)

96. R. E. Cavicchi, M. D. Antonik, R. J. Lad and S. Semancik, “*Layer-by-layer growth of epitaxial SnO₂ on sapphire by reactive sputter deposition*”, Appl. Phys. Letts., 61 (16), pp. 1921 - 1923 (1992)
97. F. Siah, Z. Yang, Z. K. Tang, M. Kawasaki, A. Ohtomo, H. Koinuma, Y. Segawa and G. K. L. Wong, “*In-plane anisotropic strain of ZnO closely packed microcrystallites grown on tilted (0001) sapphire*”, Journal of Applied Physics, 88 (5), pp. 2480 – 2483 (2000)
98. Z. Xu, A. Daga, and H. Chen, “*Microstructure and optical properties of scandium oxide thin films prepared by metalorganic chemical-vapor deposition*”, Appl. Phys. Letts., 79 (23), pp. 3782 – 3784 (2001)
99. Y. C. Chao, C. W. Lin, D. J. Ke, Y. H. Wu, H. G. Chen, L. Chang, Y. T. Ho, M. H. Liang, “*Growth of epitaxial ZnO thin film on yttria-stabilized zirconia single-crystal substrate*”, Journal of Crystal Growth 298, pp. 461–463 (2007)
100. R. Binder, “*Interaction-Induced Polarization Rotation in Anisotropic Semiconductor Quantum Wells*”, Physical Review Letters, 78 (23), pp. 4466-4469 (1997)
101. R. H. Henderson and E. Towe, “*Effective mass theory for III-V semiconductors on arbitrary (hkl) surfaces*”, Journal of Applied Physics, 79 (4), pp. 2029-2037 (1996)
102. W. Y. Liang and A. D. Yoffe, “*Transmission Spectra of ZnO Single Crystals*”, Physical Review Letters, 20 (2-8), pp. 59-62 (1968)
103. H. Matsui and H. Tabata, “*Correlation of self-organized surface nanostructures and anisotropic electron transport in nonpolar ZnO (10-10) homoepitaxy*”, Journal of Appl. Phys. 99, 124307 (2006)
104. T. F. Chung, J. A. Zapien, and S-T. Lee, “*Luminescent Properties of ZnO Nanorod Arrays Grown on Al:ZnO Buffer Layer*”, J. Phys. Chem. C, 112 (3), pp. 820 -824 (2008)
105. C. R. Gorla, W. E. Mayo, S. Liang and Y. Lu, “*Structure and interface-controlled growth kinetics of ZnAl₂O₄ formed at the (11 $\bar{2}$ 0) ZnO/(01 $\bar{1}$ 2) Al₂O₃ interface*”, J. Appl. Phys. 87 (8), pp. 3736 (2000)

CURRICULUM VITAE OF GAURAV SARAF

EDUCATION

- January 2008 **Doctor of Philosophy** in Electrical & Computer Engineering
Rutgers University, New Brunswick, New Jersey 08901
- October 2003 **Masters of Science** in Ceramics & Materials Engineering
Rutgers University, New Brunswick, New Jersey 08901
- July 2001 **Bachelor of Technology** in Metallurgical & Materials Engineering
Indian Institute of Technology, Kharagpur, India

PATENT APPLICATION

G. Saraf, Y. Chen, J. Zhu, and Y. Lu, “*MOCVD - Sputtering Hybrid Technology to Deposit Multilayer and Multifunctional Epitaxial Films*”, (Rutgers Docket Number 07-014), US patent filed in 2006

JOURNAL PUBLICATIONS

1. G. Saraf, T. Siegrist and Y. Lu, “*Anisotropic Strain in a-plane ZnO films grown on r-sapphire substrates*”, to be published in Applied Physics Letters
2. H. Chen, G. Saraf, J. Zhong, A. D. Pasquier and Y. Lu, “*ZnO nanotips/ZnO TCO hybrid structure for dye sensitized solar cells*”, to be published in Journal of Applied Physics
3. J. Zhu, H. Chen, G. Saraf, Z. Duan, S. T. Hsu and Y. Lu, “*ZnO TFT devices built on glass substrates*”, accepted to be published in Journal of Electronic Materials, 2008
4. Y. Chen, G. Saraf, T. Siegrist, and Y. Lu, “*a-plane $Mg_xZn_{1-x}O$ films deposited on r-sapphire and its surface acoustic wave characteristics*”, Journal of Vacuum Science & Technology A, Vol. 25, pp. 857-861, 2007
5. G. Saraf, J. Zhong, O. Dulub, U. Diebold, T. Siegrist and Y. Lu, “*Surface and Interface properties of MOCVD grown a-plane $Mg_xZn_{1-x}O$ ($0 \leq x \leq 0.3$) films*”, Journal of Electronic Materials, Vol 36 (4), April '2007
6. P. Wu, G. Saraf, D. H. Hill, D. A. Arena, R. A. Bartynski, F. Cosandey, J. F. Al-Sharab, L. Wielunski, R. Gateau, J. Dvorak, A. Moodenbaugh, J. A. Raley, Y. K. Yeo, and Y. Lu, “*Magnetic Properties of Fe Implanted ZnO Nanotips*”, Journal of Electronic Materials, Vol. 36 (4) April, 2007
7. Z. Zhang, H. Chen, J. Zhong, G. Saraf and Y. Lu, “*Fast and Reversible Wettability Transitions on ZnO Nanostructures*”, Journal of Electronic Materials, Volume 36 (8), 2007
8. J. Zhong, H. Chen, G. Saraf, C. K. Choi, J. J. Song, D. M. Mackie, H. Shen and Y. Lu, “*Integrated ZnO nanotips on GaN light emitting diodes for enhanced emission efficiency*”, Appl. Phys. Lett. Vol. 90 (203515), 2007

9. J. Zhong, G. Saraf, H. Chen, Y. Lu, Hock M. Ng, T. Siegrist, A. Parekh, E. A. Armour, “*Structural and Optical Properties of ZnO Nanotips Grown on GaN Using Metalorganic Chemical Vapor Deposition*”, Journal of Electronic Materials, Vol. 36 (6), June, 2007
10. G. Saraf, Y. Chen, T. Siegrist, L. S. Wielunski and Y. Lu, “*Hybrid deposition of a-plane piezoelectric $Mg_xZn_{1-x}O$ films on R-sapphire substrates using RF sputtering and MOCVD*”, Journal of Electronic Materials, Vol. 35 (6), 2006
11. P. Wu, G. Saraf, D. H. Hill, R. A. Bartynski, T. Siegrist, M. Y. Ryu, J. A. Raley, Y. K. Yeo and Y. Lu, “*Ferromagnetism in Fe-implanted a-plane ZnO Films*”, Appl. Phys. Lett., Vol. 89, (012508), 2006
12. D. H. Hill, D. A. Arena, R. A. Bartynski, P. Wu, G. Saraf, Y. Lu, L. Wielunski, R. Gateau, J. Dvorak, A. Moodenbaugh, and Yung Kee Yeo, “*Room temperature ferromagnetism in Mn Ion implanted epitaxial ZnO films*”, Phys. Stat. Sol. (a), Vol. 1–8, 2006
13. J. Zhu, G. Saraf, J. Zhong, H. F. Sheng, B. V. Yakshinskiy and Y. Lu, “ *$SiCl_4$ -based Reactive Ion Etching of $Mg_xZn_{1-x}O$ and ZnO*”, Journal of Electronic Materials, Vol. 35 (6), 2006
14. H. Chen, J. Zhong, G. Saraf, S. T. Hsu, Y. Ono and Y. Lu, “*Interface Properties of ZnO Nanotips Grown on Si Substrates*”, Journal of Electronic Materials, Vol. 35 (6), 2006
15. J. Zhu, Y. Chen, G. Saraf, N. W. Emanetoglu, and Y. Lu, “*Voltage tunable SAW phase shifter using semiconducting/piezoelectric ZnO dual-layers grown on r- Al_2O_3* ”, Appl. Phys. Lett., Vol. 89, (103513), 2006
16. Z. Zhang, N. Emanetoglu, G. Saraf, Y. Chen, P. Wu, J. Zhong, Y. Lu, J. Chen, O. Mirochnitchenko, and M. Inouye, “*DNA Immobilization and SAW Response in ZnO Nanotips Grown on $LiNbO_3$ Substrates*”, IEEE Trans. Ultrasonics, Ferroelectrics and Freq. Cont, Vol. 53 (4), 2006
17. E. Galoppini, J. Rochford, H. Chen, G. Saraf, Y. Lu, A. Hagfeldt and G. Boschloo, “*Fast Electron Transport in Metal Organic Vapor Deposition Grown Dye-sensitized ZnO Nanorod Solar Cells*”, J. Phys. Chem. B, 110 (33), 2006
18. O. Taratula, E. Galoppini, D. Wang, D. Chu, Z. Zhang, H. Chen, G. Saraf, and Y. Lu, “*Binding Studies of Molecular Linkers to ZnO and $Mg_xZn_{1-x}O$ Nanotip Films*”, J. Phys. Chem. B, Vol. 110 (13), 2006
19. H. Sheng, G. Saraf, N. W. Emanetoglu, D. Hill, Y. Lu, “*Al Ohmic Contacts to HCl Treated $Mg_xZn_{1-x}O$* ”, Journal of Electronic Materials, Vol. 34 (6), pp. 754 – 757, 2005
20. Y. Chen, N. W. Emanetoglu, G. Saraf, P. Wu, and Y. Lu, “*Analysis of SAW properties in $ZnO/Al_xGa_{1-x}N/c-Al_2O_3$ Structures*”, IEEE Trans. Ultrasonics, Ferroelectrics and Freq. Cont., Vol. 52 (7), pp. 1161 - 1169, 2005
21. H. Chen, J. Zhong, G. Saraf, Z. Zhang, L. A. Fetter, C. S. Pai and Yicheng Lu, “*Properties of ZnO nanotips selectively grown by MOCVD*”, Proc. SPIE, Vol. 5592 (164), 2005
22. Y. Song, M. Chan, C. Burman, H. Chen, G. Saraf, J. Zhong, and Y. Lu, “*Novel ZnO Nanotips: Potential Nanomaterials for New Generation of Radiation Detectors*”, Med. Phys. Vol. 32 (2006), 2005

23. P. Wu, G. Saraf, H. Chen, Y. Chen, Y. Lu, R. Bartynski, M. Ryu, Y. K. Yeo, “*Ion-beam induced sharpening of ZnO nanotips*”, Appl. Phys. Lett., Vol. 85 (7), 2004
24. J. Zhong, S. Muthukumar, G. Saraf, Y. Chen, Y. Lu, “*ZnO nanotips Grown on Silicon Substrates by Metal-Organic Chemical-Vapor Deposition*”, TMS & IEEE Journal of Electronic Materials, Vol. 33 (6), 2004
25. H. Wu, N. W. Emanetoglu, Y. Chen, G. Saraf, P. Wu, and Y. Lu, “*SAW analysis on the $Mg_xZn_{1-x}O/SiO_2/Si$* ”, IEEE Trans. Ultrasonics, Ferroelectrics and Freq. Cont., Vol. 2, 2004